Three-dimensional boundary element analysis of fractured rock

A DISSERTATION

SUBMITTED TO THE FACULTY OF THE GRADUATE SCHOOL

OF THE UNIVERSITY OF MINNESOTA

BY

Dmitry Nikolskiy

IN PARTIAL FULFILLMENT OF THE REQUIREMENTS

FOR THE DEGREE OF

Doctor of Philosophy

Joseph F. Labuz, Sofia G. Mogilevskaya, Advisers

March, 2016

Acknowledgements

I would like to express my deep gratitude to my advisers, Professors Joseph F. Labuz and Sofia G. Mogilevskaya, for their valuable guidance, for continuous encouragement, for the deserved criticism, and for major support in my research and education during the Ph.D. program.

The effort of all committee members, namely Professors Henryk K. Stolarski, Joseph F. Labuz, Sofia G. Mogilevskaya, Bernardo Cockburn, and Fernando Reitich, is highly appreciated.

I am very grateful to Professors Henryk K. Stolarski, Emmanuel M. Detournay, Roger Fosdick, Sofia G. Mogilevskaya, and Ellad Tadmor for their coursework that proved very helpful for my current research.

I also greatly appreciate the help from Professors Joseph F. Labuz, Emmanuel M. Detournay, Steven L. Crouch, Lev Khazanovich, and Charles Fairhurst in providing continuous financial support during my studies in the University of Minnesota.

I give special thanks to my fellow students, Kairat Tuleubekov, Igor Ostanin, Julien Marck, Ali Tarokh, Roman Tokmashev, Ganesh Ramakrishnan, Jeoffrey Druce, Paolo Celli, Fatemeh Pourahmadian, for helping me with accomodation to Minnesota life and climate, and for all the time we spent together that I will never forget.

I would like to specially acknowledge some faculty members of the Moscow Institute of Physics and Technology: the former dean, Sergey Gordunin (R.I.P.), and the Physics

instructor, Dmitry Alexandrov for the priceless gift of inspiration that in some sense determined the path of my life.

And, finally, I express many thanks to my loving family who, besides giving the unvaluable support through all my life, made possible my acquaintance with the University of Minnesota, helped me with my travel, and provided me housing for the recent five years.

Contents

List of Tables

List of Figures

Chapter 1

Introduction

1.1 Preamble

Understanding the mechanisms of rock fracture is of key importance to the mining and petroleum industries. Rock masses feature complicated geometry and structure including joints, heterogeneities of different scales (e.g. grains, pores, macroscopic inhomogeneities, etc.) and may be subject to various effects of injected fluid pressure, temperature gradient, etc. Therefore, comprehensive three-dimensional computational models that would allow to adequately treat complex behavior of a rock mass are required.

One of the possible industrial applications of such models is related to quantification of safety of underground workings, which may feature complicated geometry and geological conditions, including presence of natural fractures or faults. Another application is associated with simulation of hydraulic fracturing, which is characterized by strong coupling between the following physical processes:

- the fluid flow from the wellbore through the fracture described by an appropriate flow equation;

- the mechanical deformation induced by the fluid pressure on the fracture surfaces described by the elasticity equation;
- the propagation of the fracture described by an appropriate criterion.

This dissertation is concerned with the development of an efficient three-dimensional solver for the elasticity equation. This solver should be capable of accurately evaluating the stress state around the borehole-fracture systems subjected to complex loading conditions.

1.2 Background and Motivation

Three-dimensional problems of fractures in elastic media have been first studied analytically. The analytical solutions of Sack [74], Sneddon [82], Green [22], Segedin [79], and Fabrikant [15] were suggested for the problem of a planar penny-shaped crack in an infinite domain under different loading modes at infinity. Later on, semi-analytical solutions for multiple penny-shaped cracks were proposed by several authors (see [34], [35]). The problems of fracture of more complex geometry, especially for multiple cracks, could only be solved numerically.

A number of Finite Element Method (FEM)-based codes are available that allow for handling heterogeneity or non-linear response of geo-materials. However, the method has a few significant issues that impede its capabilities in modeling fracturing processes: the necessity of a volume mesh with large numbers of degrees of freedom, the restrictions on possible fracture propagation paths to the elements' interfaces, and the restriction of stress gradients due to the nature of used approximating (shape) functions, which leads to further refinement of the mesh and its rearrangement on every fracture propagation step. While recent developments in the Finite Element Method, e.g. XFEM [19, 20, 24, 39], were introduced to address the latter two issues, these methods still require a

volume mesh, thus keeping it necessary to handle large numbers of degrees of freedom most of which are not directly related to the fractures. Also, it requires the knowledge of the enrichment functions that serve to address the discontinuities and singularities of certain orders. However, in applications like hydraulic fracturing, the order of crack tip singularity is often uncertain. In general, this method, although very promising, is still under development and has not yet reached its maturity.

Among other numerical methods used for geomechanical applications, the Boundary Element Method (BEM) deserves special attention due to its capability of efficient treatment of problems that involve large domains containing inhomogeneities including fractures of arbitrary shapes. In the BEM, unlike in the FEM, the fields inside the computational domain are already exactly self-equilibrated, perhaps except for the boundaries (see [12]). This feature allows for extreme stress gradients and singularities inherent to the the fracture fronts (crack tips) that are difficult to handle with FEM, which facilitates accurate prediction of the fracture propagation paths. Another significant feature of BEM is the absence of the volume mesh, which makes it possible to solve large (virtually infinite) domain problems. Since the geometry (shape and opening) of the fractures is predicted explicitly, it facilitates the coupling of the elastic model with the hydraulic one without the necessity to handle extra degrees of freedom.

These features of BEM make it a powerful and versatile tool for various applications and a perfect basis for the development of the elastic solver for geomechanical applications. While two-dimensional Boundary Element computational models are widely available, comprehensive three-dimensional BEM models are still lacking.

1.3 Objectives and Signifucance of Research

The objective of this research is to develop the analytical basis for a three-dimensional Boundary Element-based elastic solver to be used in the future as a component of a

fully coupled three-dimensional simulator of fluid flow and evolution of the borehole-hydraulic fractures system that would include the flow (lubrication) models (see e.g. those described in [1, 14, 40]) and the appropriate fracture propagation criteria capable of capturing complex mixed-mode loading effects (see e.g [37] and the references therein, [38, 49]).

This solver should be capable of modeling real-scaled borehole-fracture systems featuring multiple fractures of arbitrary shapes interacting or originating from the borehole subjected to complex loading conditions including fluid pressure. It should allow for accurate treatment of the heterogeneity of the rock mass (natural faults, cavities). Also, the solver should be executable on a standard personal computer handling the mentioned problems within reasonable time.

Various factors such as inclination of the wellbore with respect to in-situ stresses and perforation patterns are known to affect propagation of hydraulic fractures. They lead to complex, non-planar trajectories of the fractures that are responsible for significant pressure losses at the fracture inlet.

Although this issue is well known in the industry, there are currently no computational tools available to model the complex fracture trajectory in the vicinity of the wellbore and to quantify the pressure losses associated with the fracture tortuosity. The availability of such a tool capable of accurately predicting the trajectories of non-planar hydraulic fractures would make it possible not only to optimize the perforation patterns, but also to better interpret the downhole pressure during well stimulation treatments and provide appropriate boundary conditions for large-scale quasi-three-dimensional hydraulic fracturing models where the borehole is reduced to an injection point.

As was mentioned, the elastic solver may also prove useful in non-hydraulic applications such as assessment of risks of underground mining or slope stability analysis.

1.4 Present State of Knowledge

The detailed description of the BEM formulations as well as the applications of the method can be found in various books, e.g. [2], [12], [18], [88]. The BEM formulations for crack problems, both two- and three-dimensional, can be classified as follows [2]:

- Multi-region method (see [36]), which consists in subdividing the domain along the crack surface to create two artificial subdomains for each crack. In this procedure, the conditions of displacement continuity and equilibrium of tractions are enforced at the artificial boundaries of the subdomains, as opposed to real crack boundaries. The need to create additional boundaries leads to an increase in computational costs and makes the method less efficient for multiple cracks.

- Dual BEM (see [9], [26], [50]), which consists in a separate treatment of each side of the crack; the displacement integral equation is applied on one side of the crack and the traction integral equation is applied on the other side. This also leads to an increase in computational costs related to extra unknowns, since the displacements on each side of the crack are used instead of displacement discontinuities.

- Displacement discontinuity (DD)-based method [27] – [29], [44]. In this method, the integral equation for the crack is written in terms of the displacement discontinuities, rather than displacements, and tractions, and may involve hypersingular integrals. The boundary integral equation in this method could be obtained via either the direct or indirect formulation of BEM [45], [43]. In the case of piecewise constant approximations of the unknown DDs the method is equivalent to the well-known Displacement Discontinuity Method [10], [11]. The latter method does not explicitly formulate integral representations neither of the boundary fields nor of the internal fields. Instead, it utilizes the superposition of analytical solutions that provide certain displacement jumps across the elements of regular shapes.

The DD-based approach (in its broader sense that includes an integral formulation) is the most relevant in the context of this work. Therefore, the literature review from this point on will be concentrated mostly on publications describing the DD-based methods.

The relevant publications could be further classified based on several criteria:

- types of limit to the boundary processes (before or after the approximation);
- types of boundary integral equations (hypersingular or regularized);
- types of boundary elements (triangular, quadrilateral, etc.) and approximations for the unknowns;
- techniques of integration (analytical, numerical, or mixed);
- setup of the linear algebraic systems (collocation, Galerkin, symmetric Galerkin).

The classification along some of these lines could be found in the review article by Tanaka et al. [84], which contains an extensive list of references on the topic. However, the review covers only integral equation-based approaches. A significant number of papers were published since then and it is difficult to review all of them here. Thus, we mention just a few recent publications and, in addition, review some relevant papers that are based on the classical DDM.

The "limit after integration" process is, in some sense, evoked in DDM-based papers [32], [33], [41]. In these papers, the triangular elements with constant approximations for the unknowns are employed. The system of equations is set up via collocation. In [41], the crack-tip elements with square root approximation are introduced. Although the integral equation is not written, the coefficients in the matrix of the linear system represent the integrals over the triangular elements (with constant approximation of DDs for ordinary elements and square root approximations for the tip elements). The expressions for the coefficients related to ordinary elements are given in closed form.

However, the list of those expressions in rather long (five pages of Appendix A in [32]). The treatment of the tip elements combines analytical and numerical integration, where the former employs symbolical manipulations in Mathematica 3.0. The extension of this approach to include higher order approximations for the unknowns (without explicit consideration of the boundary integral equation) seems to require significant effort and lead to more lengthy expressions.

Another group of papers, not reviewed in [84], starts with explicit formulations of the BIEs. Thus, Qin et al. [71], [72] considered the problems of a planar crack and wrote a hypersingular integral equation for the stresses on its boundary. Such approach leads to the increase in the number of equations as compared with the more efficient approach in which the BIE is written for the tractions. The authors present the integral expressions for the fields over each element (including tip elements). However, they do not provide specific details on the integration techniques.

Lo et al. [48] presented traction hypersingular BIE for the problems of multiple cracks. The equation is then regularized and reduced to a weakly singular one. Quadratic 8-point discontinuous elements enriched by crack tip asymptotics are used for the approximations. Integrals are evaluated numerically and collocation method is used to set up the system of linear algebraic equations.

A number of publications adopt the symmetric Galerkin BEM for three-dimensional crack problems (see e.g. [16], [17] and references therein). In such formulation both displacement and traction BIEs (the latter is sometimes regularized, as in [16]) are employed, which leads to a symmetric matrix of the linear algebraic system. In addition, this formulation is a weak one, which relaxes the conditions on approximating functions. The drawback of the method is the use of double integration, which could be computationally expensive. Various numerical schemes are used to evaluate these integrals on quadrilateral and triangular isoparametric elements.

It should be noted that apart from the classical DDM-based works, practically all publications that employ triangular elements utilize either numerical or mixed (numerical and analytical) integration schemes. However, the analytical treatment of some integrals, including hypersingular ones, involved in BIEs for crack problems have been reported in several publications that deal with standard elastostatic problems [61], [75]. The procedure to analytically evaluate integrals over triangular and rectangular elements is outlined in [46] for a special form of the traction hypersingular equation in local coordinate systems. However, closed-form expressions for all integrals involved have not been recorded suggesting that most of the integrals could be obtained by differentiation of a few closed-form expressions.

1.5 Organization of the Dissertation

The rest of the dissertation is organized as follows.

In Chapter 2, the basic mathematical concepts and those of Elasticity theory used in the dissertation are briefly summarized. Chapter 3 provides an overview of Boundary Integral formulations equivalent to Boundary Value Problems of Elasticity and considerations on incorporation of fractures into these formulations. In Chapter 4, an overview of the Boundary Element Method (BEM) and the detailed description of the computational scheme developed in the present research including the analytical integration strategy are provided. Chapter 5 presents numerical examples serving to validate the proposed computational approach. In Chapter 6, the outcome of the present research is summarized and its implications are discussed.

In Appendix A, some comments on treatment of body (volume) integrals involved in Boundary Integral Equations are provided. In Appendix B, an algorithm of calculation of coefficients of the approximating functions is described. In Appendix C, details on extension of the boundary elements' geometry (treatment of circular arcs as parts of

the element's contour) are provided. In Appendix D, a closed-form analytical solution for the stress field around a penny-shaped crack (used for validation of the described technique) is reproduced.

Chapter 2

Preliminaries

2.1 Basic Mathematical Concepts

2.1.1 Complex Variables and Functions

A complex number or a complex variable is defined as the following combination of real numbers x_1 and x_2:

$$z = x_1 + ix_2$$

where i is called the imaginary unit; $i^2 = -1$. Such combination can be related to a point on a plane with Cartesian coordinates (x_1, x_2) called the complex plane.

The complex conjugate of z is defined as

$$\overline{z} = x_1 - ix_2$$

A complex-valied function can be defined as a combination of two real-valued functions of two real variables:

$$f(z) = f_1(x_1, x_2) + if_2(x_1, x_2)$$

Holomorphic Functions, Cauchy-Riemann Conditions

For a function $f(z)$ defined in some open set (region) Ω, its complex derivative at some point z_0 can be defined as the limit:

$$f'(z_0) = \lim_{z \to z_0} \frac{f(z) - f(z_0)}{z - z_0} \tag{2.1}$$

The limit in (2.1) must not depend on the direction from which z approaches z_0. To assure this, the function $f(z) = f_1(x_1, x_2) + if_2(x_1, x_2)$ must satisfy the following Cauchy-Riemann conditions at $z = x_1 + ix_2$:

$$\frac{\partial f_1}{\partial x_1} = \frac{\partial f_2}{\partial x_2}, \quad \frac{\partial f_1}{\partial x_2} = -\frac{\partial f_2}{\partial x_1} \tag{2.2}$$

The function $f(z)$ is called holomorphic in the open set Ω if it is complex differentiable at every $z \in \Omega$. Therefore, the function $f(z)$ is holomorphic if and only if the Cauchy-Riemann conditions (2.2) are satisfied everywhere in Ω. It is worth mentioning that in this case the function is also infinitely differentiable in Ω.

Complex Integrals

Consider a continuous complex-valued function $f(z)$ and a smooth curve Γ in the complex plane parametrized by a real number t varying from a to b:

$$z(t) = x(t) + iy(t)$$

The complex line integral of f over Γ is defined as the following line integral:

$$\int_\Gamma f(z)dz = \int_a^b f(z(t))z'(t)dt; \ z \in \Gamma \tag{2.3}$$

Integrals of the following kind

$$F(\tau) = \int_\Gamma \frac{f(z)}{z - \tau} dz$$

are called Cauchy type integrals.

If Γ is a closed curve (contour), the following notation is used:

$$\oint_{\Gamma} f(z)dz$$

where the default direction of integration over Γ is counterclockwise, so the interior of Γ is located on the left of the integration path.

Cauchy Integral Theorems

If $f(z)$ is holomorphic in a simply connected complex region Ω and Γ is a sufficiently smooth closed non-self-intersecting curve (contour) totally located inside Ω then

$$\oint_{\Gamma} f(z)dz = 0 \tag{2.4}$$

Also, for every point z_0 of the interior of Γ

$$f(z_0) = \frac{1}{2\pi i} \oint_{\Gamma} \frac{f(z)}{z - z_0} dz \tag{2.5}$$

For every point $z_0 \in \Omega$ located in the exterior of Γ

$$\frac{1}{2\pi i} \oint_{\Gamma} \frac{f(z)}{z - z_0} dz = 0$$

Sokhotski-Plemelj Formulae

Consider a Cauchy type integral over a sufficiently smooth open or closed curve Γ:

$$F(z_0) = \frac{1}{2\pi i} \int_{\Gamma} \frac{f(z)}{z - z_0} dz$$

Let z_0 approach τ belonging to the smooth part of Γ from its left or right side (τ does not coinside with the ends of Γ in case of an open curve). If the function $f(z)$ is holomorphic in the neighborhood of τ then the limits $F^+(\tau)$ and $F^-(\tau)$ are given by

Sokhotski-Plemelj formulae (see [55, 80]):

$$F^+(\tau) = \frac{1}{2\pi i}\oint_\Gamma \frac{f(z)}{z-\tau}dz + \frac{1}{2}f(\tau)$$
$$F^-(\tau) = \frac{1}{2\pi i}\oint_\Gamma \frac{f(z)}{z-\tau}dz - \frac{1}{2}f(\tau) \tag{2.6}$$

where the sign"+" ("–") identifies the left (right) side of Γ defined by the direction of the integration path and the integral over Γ is understood as Cauchy principal value integral (see Subsection 2.1.2).

These formulae can be generalized to include piecewise-smooth curves (see [55]):

$$F^+(\tau) = \frac{1}{2\pi i}\oint_\Gamma \frac{f(z)}{z-\tau}dz + \frac{\gamma}{2\pi}f(\tau)$$
$$F^-(\tau) = \frac{1}{2\pi i}\oint_\Gamma \frac{f(z)}{z-\tau}dz - \frac{\gamma}{2\pi}f(\tau) \tag{2.7}$$

where γ is the angle of Γ at the point z_0 taken from the "+" side of the curve. For regular (smooth) points, $\gamma = \pi$.

Wirtinger Calculus

The so-called Wirtinger derivatives are employed in the following analysis:

$$\frac{\partial}{\partial z} = \frac{1}{2}\left(\frac{\partial}{\partial x_1} - i\frac{\partial}{\partial x_2}\right), \quad \frac{\partial}{\partial \overline{z}} = \frac{1}{2}\left(\frac{\partial}{\partial x_1} + i\frac{\partial}{\partial x_2}\right) \tag{2.8}$$

in which z and $\overline{z}$ are treated as independent variables.

One of attractive features of Wirtinger derivatives is that they allow for a concise way to formulate the Cauchy-Riemann conditions. Specifically, the Wirtinger derivative of a holomorphic function f with respect to $\overline{z}$ is zero,

$$\frac{\partial f}{\partial \overline{z}} = 0$$

i.e. f is independent of $\overline{z}$ (see [85]).

Cauchy-Pompeiu (Borel-Pompeiu) Formulae

Cauchy integral theorems are valid for holomorphic functions. However, they can be generalized to include sufficiently smooth functions that are not necessarily holomorphic. For such function f and a region Ω on the complex plane bounded by a simple (non-self-intersecting) curve Γ the following integral representations apply (see [70, 85]):

$$\frac{1}{2\pi i}\oint_{\Gamma}\frac{f(\tau,\overline{\tau})\,d\tau}{\tau-z}-\frac{1}{\pi}\int_{\Omega}\frac{\partial f(\tau,\overline{\tau})}{\partial\overline{\tau}}\frac{dS}{\tau-z}=\begin{cases} f(z,\overline{z}), & z\in\Omega,\\ 0, & z\notin\Omega\cup\Gamma,\end{cases} \tag{2.9}$$

$$-\frac{1}{2\pi i}\oint_{\Gamma}\frac{f(\tau,\overline{\tau})\,d\overline{\tau}}{\overline{\tau}-\overline{z}}-\frac{1}{\pi}\int_{\Omega}\frac{\partial f(\tau,\overline{\tau})}{\partial\tau}\frac{dS}{\overline{\tau}-\overline{z}}=\begin{cases} f(z,\overline{z}), & z\in\Omega,\\ 0, & z\notin\Omega\cup\Gamma.\end{cases} \tag{2.10}$$

Notations like $f(z,\overline{z})$ are used for the functions that are not necessarily holomorphic.

The limit values of Cauchy type integrals involved in (2.9) and (2.10) as the point $z\in\Omega$ approaches the boundary, $z\to z_0\in\Gamma$, can be evaluated using Sokhotsli-Plemelj formulae (see [55, 80]) as follows:

$$\lim_{\mathbf{z}\to\mathbf{z_0}}\frac{1}{2\pi i}\oint_{\Gamma}\frac{f(\tau,\overline{\tau})\,d\tau}{\tau-z}=\frac{\gamma}{2\pi}f(z_0,\overline{z_0})+\frac{1}{2\pi i}\fint_{\Gamma}\frac{f(\tau,\overline{\tau})\,d\tau}{\tau-z_0} \tag{2.11}$$

in which $\fint_{\Gamma}$ is understood as a Cauchy principal value integral, and γ is an internal angle of the curve Γ at the point z_0. Thus,

$$\gamma=\begin{cases}\pi & \text{for regular points,}\\ \gamma_k & \text{for } k\text{-th corner point,}\end{cases} \tag{2.12}$$

where γ_k, $0<\gamma_k\le 2\pi$, $(k=1,\ldots,M)$ is the internal angle at the k-th corner point of the piecewise smooth curve Γ; $M=0$ for smooth curves.

2.1.2 Singular Integrals

Consider a sufficiently smooth function $f(z)$ defined on a the interval $[a,b]$ containing the point z_0 and an integral of the following type:

$$\int_a^b\frac{f(z)}{(z-z_0)^{\alpha}}dz \tag{2.13}$$

If $0 < \alpha < 1$ and the function f is continuous, such integral is called weakly singular and can be defined via the limits of regular Riemann integrals:

$$\int_a^b \frac{f(z)}{(z-z_0)^\alpha} dz = \lim_{\epsilon \to 0^+} \int_a^{z_0-\epsilon} \frac{f(z)}{(z-z_0)^\alpha} dz + \lim_{\delta \to 0^+} \int_{z_0+\delta}^b \frac{f(z)}{(z-z_0)^\alpha} dz \tag{2.14}$$

If $\alpha = 1$ and f is Hölder continuous ($f \in C^{0,\alpha}$), the integral is singular and defined as the following Cauchy principal value integral:

$$⨍_a^b \frac{f(z)}{z-z_0} dz = \lim_{\epsilon \to 0^+} \left[\int_a^{z_0-\epsilon} \frac{f(z)}{z-z_0} dz + \int_{z_0+\epsilon}^b \frac{f(z)}{z-z_0} dz \right] \tag{2.15}$$

If $\alpha = 2$ and $f' \in C^{1,\alpha}$, the integral is hypersingular and can be defined as Hadamard finite part [25]:

$$⨎_a^b \frac{f(z)}{(z-z_0)^2} dz = \lim_{\epsilon \to 0^+} \left[\int_a^{z_0-\epsilon} \frac{f(z)}{(z-z_0)^2} dz + \int_{z_0+\epsilon}^b \frac{f(z)}{(z-z_0)^2} dz - 2\frac{f(z_0)}{\epsilon} \right] \tag{2.16}$$

More details onf the theory of complex singular integrals are provided in literature (see e.g. [42, 44, 45]).

2.1.3 Lagrange Polynomials

Consider a discrete set of points $\mathbf{x}_1..\mathbf{x}_K$. The polynomials defined as

$$L^{(N)}(\mathbf{x}) = \prod_{\substack{M=1 \\ M \neq N}}^{K} \frac{\mathbf{x} - \mathbf{x}_M}{\mathbf{x}_N - \mathbf{x}_M} \tag{2.17}$$

are called Lagrange basis polynomials. It is easy to show that for every $1 \leq N \leq K$

$$L^{(N)}(\mathbf{x}_M) = \begin{cases} 1 \; if \; M = N \\ 0 \; if \; M \neq N \end{cases} \tag{2.18}$$

Given the corresponding set of data points $y_1..y_K$, the interpolating polynomial can be presented as a combination of the basis functions 2.17:

$$y(\mathbf{x}) = \sum_{M=1}^{K} y_M L^{(M)}(\mathbf{x}) \tag{2.19}$$

2.2 Basic Concepts of Elasticity

The numerical model developed in the present work is based on main concepts of Continuum Mechanics, which are described in various textbooks (see e.g. [4, 23]). In the following, a short review of these concepts is provided.

Traction, Stress, and Equilibrium

The vector $\mathbf{t}(\mathbf{x})$ that expresses force per unit area acting at a given point on a specified surface that contains this point is called traction. At a point located inside the material, one can pass an imaginary surface (e.g.plane) oriented arbitrarily. The traction acting on such surface depends on its orientation. Stress is a second order tensor, which can be defined in Cartesian coordinates via a 3x3 matrix. The physical meaning of the component σ_{kl}, $k, l = 1, 2, 3$ of the stress tensor is k-th component of traction (force per unit area) acting on the plane perpendicular to the j-th coordinate axis. Thus, given the orientation of the surface at the point $\mathbf{x}$, the traction vector at this point can be expressed via its components as $t_k(\mathbf{x}) = \sigma_{kl}(\mathbf{x})n_l(\mathbf{x})$, where $n_l(\mathbf{x})$ are the components of the unit vector $\mathbf{n}(\mathbf{x})$ normal to the surface at the point $\mathbf{x}$.

To satisfy the equilibrium of moments, the stress tensor σ must be symmetric [4]:

$$\sigma_{mn}(\mathbf{x}) = \sigma_{nm}(\mathbf{x}) \tag{2.20}$$

Equilibrium of forces leads to the following equation [4]:

$$\sigma_{mn,n}(\mathbf{x}) = b_m(\mathbf{x}) \tag{2.21}$$

where $b_m(\mathbf{x}), m = 1, 2, 3$ are the Cartesian components of the external body force vector $\mathbf{b}(\mathbf{x})$ (force per unit volume) applied at the point $\mathbf{x}$. Here and in the following, standard indicial notation is used, i.e. repeated indices imply summation and $f_{,m} = \partial f/\partial x_m$ is the partial derivative of $f(\mathbf{x})$ with respect to the m-th Cartesian coordinate of $\mathbf{x}$. Also in the following, tensile stresses are considered positive.

Displacements, Strains, and Compatibility

A deformed state of a body can be defined by displacement of every material point of the body with respect to the reference (unloaded) state (thus, the Lagrangian description of motion of continua is used). The displacement of the point $\mathbf{x}$ is denoted by the vector $\mathbf{u}(\mathbf{x})$ with components $u_k(\mathbf{x})$, $k = 1, 2, 3$.

To exclude rigid body motion, which does not produce deformation, the local deformation of the material should rather be described via relative displacements or strains. Strains can be defined in several ways and, generally, are not linearly expressed in terms of displacements (see [23]). In the so-called small (infinitesimal) strain approximation, which is employed in the following analysis, strains are linear with respect to displacements and are defined by Cartesian components as

$$\epsilon_{mn} = \frac{1}{2}(u_{m,n} + u_{n,m}) \tag{2.22}$$

Distribution of strains over a deformed body must provide the uniqueness of displacements of every material point, i.e. the material should not become discontinuous or overlap itself anywhere. To provide this, the strains must satisfy the following compatibility conditions:

$$\varepsilon_{klm}\varepsilon_{npq}\epsilon_{lp,kr} = 0 \tag{2.23}$$

where $f_{,km}$ denotes the second partial derivative $\frac{\partial^2 f}{\partial x_k \partial x_m}$ and ε_{klm} is the permutation symbol ($\varepsilon_{klm} = 1$ if k, l, m is a cyclic permutation of $1, 2, 3$; $\varepsilon_{lkm} = -\varepsilon_{klm}$; $\varepsilon_{kkm} = 0$).

It can be shown that, if strains are defined via displacements as (2.22), these conditions are automatically satisfied.

Hooke's law

The theory of linear elasticity is used in the present work, which proposes that, for an equilibrium state of the material, stresses and strains at each material point are

proportional to each other.

$$\sigma_{kl} = c_{klmn}\epsilon_{mn} \tag{2.24}$$

where c_{klmn} are the components of the 4-th order symmetric stiffness tensor $\mathbf{c}$.

In the following, the analysis is restricted to isotropic materials, for which the tensor $\mathbf{c}$ is invariant with respect to any rotation of the coordinate system. Consequently, all components of $\mathbf{c}$ can be expressed via 2 independent scalars. So, Eq.(2.24) can be written as follows:

$$\sigma_{kl} = \lambda\delta_{kl}\epsilon_{mm} + 2\mu\epsilon_{kl} \tag{2.25}$$

where δ_{kl} is Kronecker delta,

$$\delta_{kl} = \begin{cases} 1 \ if \ k = l \\ 0 \ if \ k \neq l \end{cases}$$

μ is the shear modulus, λ is the Lamé constant of the medium that can expressed via Poisson's ratio as follows:

$$\lambda = \frac{2\mu\nu}{1-2\nu}$$

Combining Eqs.(2.21), (2.22), and (2.25), one can obtain the so called Navier-Cauchy (Lamé) equilibrium equation, which expresses the equilibrium of the material in terms of displacements:

$$\lambda u_{k,km} + \mu\left(u_{m,jj} + u_{j,mj}\right) + b_m = 0 \tag{2.26}$$

2.3 Boundary Value Problems of Elasticity

Generally, deformation of an elastic body is determined not only by the applied body forces, but also by the loads (tractions) and/or displacements on its boundary. The unknown elastic fields - displacements, strains, and stresses inside the body (domain), as well as displacements on the parts of the boundary with prescribed loads, tractions

on the parts of the boundary with prescribed displacements - are to be found by solving the corresponding boundary value problem.

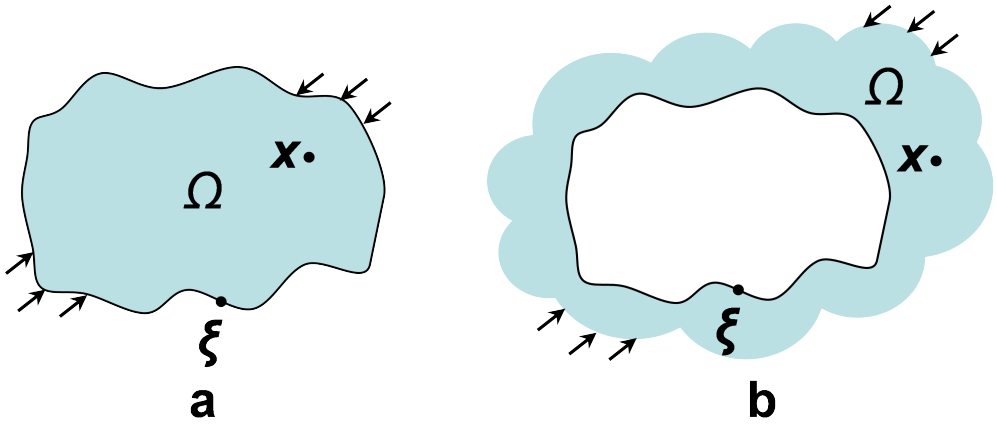

Figure 2.1: Boundary Value Problem formulation. Finite and infinite computational domain.

Two types of boundary value problems are considered in the following analysis: that of a bounded finite domain Ω with loads (tractions) applied on part of its boundary $\partial\Omega$ and that of an infinite domain containing voids, cracks, etc. with loads applied at infinity as well as on part of the internal boundaries.

In general, boundary value problems of elasticity can be only solved by means of numerical methods. However, in some specific cases, Eq.(2.26) can be solved analytically. One of such solutions plays an important role in the further analysis.

2.4 Kelvin Fundamental Solution

Consider the problem of an infinite elastic medium subjected to the unit point force applied at the point $\boldsymbol{\xi}$ in the direction of j-th Cartesian coordinate axis ($j = 1, 2, 3$).

The solution of this problem is attributed to Lord Kelvin (William Thomson) and is called the Kelvin Fundamental Solution [4]. The displacement at any point except $\boldsymbol{\xi}$

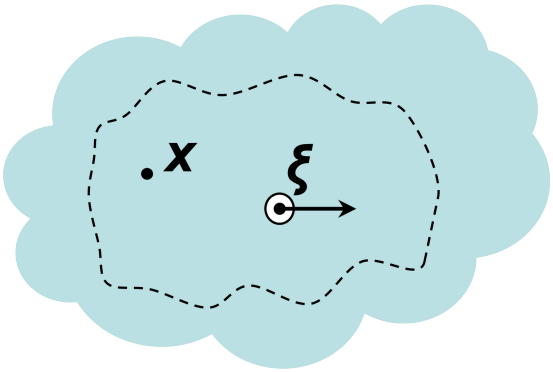

Figure 2.2: Infinite domain subjected to point force.

can be expressed by the second order tensor with the following components:

$$U_{mj}(\mathbf{x},\boldsymbol{\xi}) = \frac{1}{16\pi\mu(1-\nu)r}\left[(3-4\nu)\delta_{mj} + r_{,m}r_{,j}\right] \tag{2.27}$$

in which U_{mj} is the m-th component of displacement at point $\mathbf{x}$ due to the unit point force in j-th direction applied at the point $\boldsymbol{\xi}$; $m = 1, 2, 3$; $r_m = x_m - \xi_m$; x_m and ξ_m are the m-th coordinates of $\mathbf{x}$ and $\boldsymbol{\xi}$, respectively; $r = |\mathbf{r}|$ is the distance between the points $\mathbf{x}$ and $\boldsymbol{\xi}$; δ_{mj} is Kronecker's symbol.

This solution satisfies Eq.(2.26) at every point except $\boldsymbol{\xi}$. At that point it is singular; the displacement tends to infinity as $\frac{1}{r}$ as the point $\mathbf{x}$ tends to $\boldsymbol{\xi}$ [31]. The tensor $\mathbf{U}$ also posesses the following symmetry property:

$$U_{mj}(\mathbf{x},\boldsymbol{\xi}) = U_{jm}(\boldsymbol{\xi},\mathbf{x})$$

Using the relationships between the displacements and strains (2.22), as well as Hooke's law (2.25), the traction vector at the point $\mathbf{x}$ on the surface characterized by the unit normal vector $\mathbf{n}(\mathbf{x})$ can be represented as follows:

$$\begin{aligned} T_{mj}(\mathbf{x},\boldsymbol{\xi}) = &\frac{1}{8\pi(1-\nu)r^2}\Big\{(1-2\nu)[n_m(\mathbf{x})r_{,j} - r_{,m}\, n_j(\mathbf{x})] \\ &- \frac{\partial r}{\partial \mathbf{n}(\mathbf{x})}[3r_{,m}\, r_{,j} + (1-2\nu)\delta_{mj}]\Big\} \end{aligned} \tag{2.28}$$

where $n_k(\mathbf{x})$ is the k-th the component of $\mathbf{n}(\mathbf{x})$ and

$$\frac{\partial r}{\partial \mathbf{n}(\mathbf{x})} = \frac{\partial r}{\partial x_m} n_m(\mathbf{x}) = \frac{r_m n_m(\mathbf{x})}{r}$$

Note that the order of singularity of $T_{mj}(\mathbf{x}, \boldsymbol{\xi})$ as $\mathbf{x}$ tends to $\boldsymbol{\xi}$ is higher ($\frac{1}{r^2}$) [31].

2.5 Surface Potentials

Using superposition, solutions of more general kind can be found. Consider a sufficiently smooth surface S, vector functions (densities) $\boldsymbol{\phi}(\boldsymbol{\xi})$ and $\boldsymbol{\psi}(\boldsymbol{\xi})$ defined on this surface, and the following integrals called surface potentials (see [31, 65, 53]):

- a single layer potential

$$\int_S \boldsymbol{\phi}(\boldsymbol{\xi}) \mathbf{U}(\mathbf{x}, \boldsymbol{\xi}) dS_\xi \tag{2.29}$$

- a double layer potential

$$\int_S \boldsymbol{\psi}(\boldsymbol{\xi}) \mathbf{T}^T(\boldsymbol{\xi}, \mathbf{x}) dS_\xi \tag{2.30}$$

- an adjoint double layer potential

$$\int_S \boldsymbol{\phi}(\boldsymbol{\xi}) \mathbf{T}(\mathbf{x}, \boldsymbol{\xi}) dS_\xi \tag{2.31}$$

- a hypersingular potential

$$\int_S \boldsymbol{\psi}(\boldsymbol{\xi}) \mathbf{H}(\boldsymbol{\xi}, \mathbf{x}) dS_\xi \tag{2.32}$$

where the superscript T identifies transposition of the corresponding tensor, the kernels involved in (2.29 – 2.31) are given by tensor components (2.27 – 2.28), and the kernel

of (2.32) is given by the following components:

$$
\begin{aligned}
H_{mj}(\mathbf{x},\boldsymbol{\xi}) = \\
&\frac{\mu}{4\pi(1-\nu)r^3}\Bigg\{(1-2\nu)[\delta_{mj}n_k(\mathbf{x})n_k(\boldsymbol{\xi})+n_m(\boldsymbol{\xi})n_j(\mathbf{x})]-(1-4\nu)n_m(\mathbf{x})n_j(\boldsymbol{\xi}) \\
&+3\nu\left[n_k(\mathbf{x})n_k(\boldsymbol{\xi})r_{,m}\,r_{,j}+\frac{\partial r}{\partial \mathbf{n}(\boldsymbol{\xi})}r_{,m}\,n_j(\mathbf{x})+\frac{\partial r}{\partial \mathbf{n}(\mathbf{x})}r_{,j}\,n_m(\boldsymbol{\xi})+\delta_{mj}\frac{\partial r}{\partial \mathbf{n}(\boldsymbol{\xi})}\frac{\partial r}{\partial \mathbf{n}(\mathbf{x})}\right] \\
&+\frac{3(1-2\nu)}{r}\left[\frac{\partial r}{\partial \mathbf{n}(\boldsymbol{\xi})}r_{,j}\,n_m(\mathbf{x})+\frac{\partial r}{\partial \mathbf{n}(\mathbf{x})}r_{,m}\,n_j(\boldsymbol{\xi})\right]-15\frac{\partial r}{\partial \mathbf{n}(\mathbf{x})}\frac{\partial r}{\partial \mathbf{n}(\boldsymbol{\xi})}r_{,m}\,r_{,j}\Bigg\}
\end{aligned}
\tag{2.33}
$$

in which $m,j,k=1,2,3$, $n_k(\boldsymbol{\xi})$ is the k-th component of the unit vector $\mathbf{n}(\boldsymbol{\xi})$ normal to S at the point $\boldsymbol{\xi}\in S$, and

$$\frac{\partial r}{\partial \mathbf{n}(\boldsymbol{\xi})}=\frac{\partial r}{\partial \xi_m}n_m(\boldsymbol{\xi})=-\frac{r_m n_m(\boldsymbol{\xi})}{r}$$

Note that the tensor $\mathbf{H}$ is also symmetric:

$$H_{mj}(\mathbf{x},\boldsymbol{\xi})=H_{jm}(\boldsymbol{\xi},\mathbf{x})$$

and has the order of singularity $\frac{1}{r^3}$ (hypersingular).

Equation (2.26) is automatically satisfied when the vector $\mathbf{u}(\mathbf{x})$ is equal to any of expressions (2.29 – 2.32) or their linear combinations. Eq. (2.29) can be interpreted as the displacement at the point $\mathbf{x}$ due to the concentrated forces distributed on the surface S with the density given by the function $\boldsymbol{\phi}(\boldsymbol{\xi})$. The physical meaning of the double layer potential (2.30) is the displacement at the point $\mathbf{x}$ due to the moments distributed on S with the density given by $\boldsymbol{\psi}(\boldsymbol{\xi})$ (see [65]). Consequenty, Eqs. (2.31 – 2.32) express the tractions corresponding to the displacement field given by (2.29 – 2.30).

If the closed or open surface S is sufficiently smooth and $\boldsymbol{\xi_0}$ is neither a corner nor an end point of S, the potentials of Eqs.(2.29) and (2.32) are continuous when the point $\mathbf{x}$

approaches the point $\boldsymbol{\xi_0}$, while potentials of Eqs. (2.30) and (2.31) undergo the jumps:

$$\begin{aligned}
\lim_{\mathbf{x}\to\boldsymbol{\xi_0}} \int_S \boldsymbol{\phi}(\boldsymbol{\xi})\mathbf{U}(\mathbf{x},\boldsymbol{\xi})dS_\xi &= \int_S \boldsymbol{\phi}(\boldsymbol{\xi})\mathbf{U}(\boldsymbol{\xi_0},\boldsymbol{\xi})dS_\xi \\
\lim_{\mathbf{x}\to\boldsymbol{\xi_0}} \int_S \boldsymbol{\psi}(\boldsymbol{\xi})\mathbf{T}^T(\boldsymbol{\xi},\mathbf{x})dS_\xi &= \pm\frac{1}{2}\boldsymbol{\psi}(\boldsymbol{\xi_0}) + \neq\!\!\!\!\int_S \boldsymbol{\psi}(\boldsymbol{\xi})\mathbf{T}^T(\boldsymbol{\xi},\boldsymbol{\xi_0})dS_\xi \\
\lim_{\mathbf{x}\to\boldsymbol{\xi_0}} \int_S \boldsymbol{\phi}(\boldsymbol{\xi})\mathbf{T}(\mathbf{x},\boldsymbol{\xi})dS_\xi &= \mp\frac{1}{2}\boldsymbol{\phi}(\boldsymbol{\xi_0}) + \neq\!\!\!\!\int_S \boldsymbol{\phi}(\boldsymbol{\xi})\mathbf{T}(\boldsymbol{\xi_0},\boldsymbol{\xi})dS_\xi \\
\lim_{\mathbf{x}\to\boldsymbol{\xi_0}} \int_S \boldsymbol{\psi}(\boldsymbol{\xi})\mathbf{H}(\boldsymbol{\xi},\mathbf{x})dS_\xi &= \neq\!\!\!\!\int_S \boldsymbol{\psi}(\boldsymbol{\xi})\mathbf{H}(\boldsymbol{\xi},\boldsymbol{\xi_0})dS_\xi
\end{aligned} \tag{2.34}$$

where the sign " $+$ " or " $-$ " indicates the fields related to the corresponding side of S (with respect to the direction of the prescribed normal vector). For sufficiently smooth S and density functions, the first integral is weakly singular, the second and third integrals involved in Eq.(2.34) are Cauchy principal value integrals, while the fourth integral is a hypersingular, Hadamard finite part integral [25]. From Eq.(2.34) it follows that the physical meaning of the density functions $\boldsymbol{\psi}(\boldsymbol{\xi})$ and $\boldsymbol{\phi}(\boldsymbol{\xi})$ is the jumps of the corresponding potentials (2.30) and (2.31) over S.

Note that, as mentioned above, the described potentials can be defined for closed and open surfaces. This makes it possible to construct the solutions of boundary value problems including crack problems as combinations of potentials with the density functions to be determined.

2.6 Betti's Reciprocal (Virtual) Work Theorem

Consider two different deformed states of the same elastic body (domain) Ω defined by stresses and strains σ, ϵ and σ^*, ϵ^*, respectively (see Fig. 2.3).

Betti's reciprocal work theorem states (see [4]) that the work of stresses and boundary tractions of the first state done on strains and boundary displacements of the second state is equal to the work of stresses and boundary tractions of the second state on strains

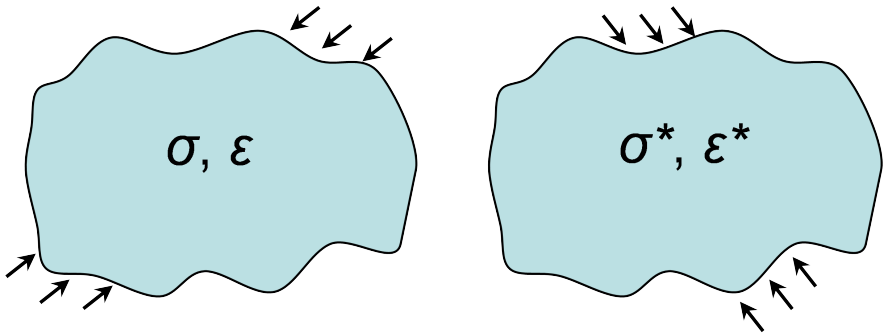

Figure 2.3: Illustration of Reciprocal Work Principle.

and boundary displacements of the first state:

$$\int_{\Omega} \sigma_{kl}\epsilon^*_{kl} d\Omega + \int_{\partial\Omega} t_k u^*_k dS = \int_{\Omega} \sigma^*_{kl}\epsilon_{kl} d\Omega + \int_{\partial\Omega} t^*_k u_k dS \tag{2.35}$$

As one of the states in (2.35), a closed-form analytical solution of Lamé equation, e.g. Kelvin fundamental solution, can be used. The latter solution $\mathbf{U}(\boldsymbol{\xi}, \mathbf{x})$, however, cannot be used directly if the point $\mathbf{x} \in \Omega$ because of its singularity. For $\mathbf{x} \notin \Omega$, after substituting $\mathbf{U}(\boldsymbol{\xi}, \mathbf{x})$ as one of the states in (2.35) and applying divergence (Gauss) theorem to the displacements and tractions on the boundary $\partial\Omega$ one gets the following integral relation:

$$0 = \int\limits_{\partial\Omega} U_{mj}(\mathbf{x}, \boldsymbol{\xi}) t_j(\boldsymbol{\xi}) dS_\xi - \int\limits_{\partial\Omega} T_{jm}(\boldsymbol{\xi}, \mathbf{x}) u_j(\boldsymbol{\xi}) dS_\xi + \int\limits_{\Omega} U_{mj}(\mathbf{x}, \eta) b_j(\eta) dV_\eta \tag{2.36}$$

Here and in the following subsection, Ω is considered finite, bounded, and simply connected.

Obtaining a similar integral identity for points located inside the domain (known as Somigliana's identity) requires some modifications.

2.7 Somigliana Identities

For a point $\mathbf{x} \in \Omega$, instead of Ω one should consider a similar domain with excluded small spherical neighborhood S_ϵ of radius ϵ of the point $\mathbf{x} \in \Omega$. Then, similarly, the Kelvin

solution $\mathbf{U}(\boldsymbol{\xi}, \mathbf{x})$ is substituted as one of the two states in (2.35) and divergence (Gauss) theorem is applied to the displacements and tractions on the boundary $\partial\Omega \cup \partial S_\epsilon$. After making ϵ go to zero, one can obtain the following identity that relates the displacement vector at the point $\mathbf{x} \in \Omega$ with the displacements and the tractions at the boundary $\partial\Omega$ of the domain:

$$u_m(\mathbf{x}) = \int\limits_{\partial\Omega} U_{mj}(\mathbf{x}, \boldsymbol{\xi}) t_j(\boldsymbol{\xi}) dS_\xi - \int\limits_{\partial\Omega} T_{jm}(\boldsymbol{\xi}, \mathbf{x}) u_j(\boldsymbol{\xi}) dS_\xi + \int\limits_{\Omega} U_{mj}(\mathbf{x}, \eta) b_j(\eta) dV_\eta \quad (2.37)$$

where $\boldsymbol{\xi} \in \partial\Omega$ (Σ), $\boldsymbol{\eta} \in \Omega$, the components U_{mj} of the tensor $\mathbf{U}$ that represents the kernel of the single layer potential are given by (2.27) and the components T_{jm} are of the transposed tensor $\mathbf{T}$ (2.28). Thus, the right-hand side of Eq.(2.37) is a combination of a single layer potential with density $\mathbf{t}(\boldsymbol{\xi})$ and a double layer potential with density $\mathbf{u}(\boldsymbol{\xi})$. Note that these density functions have the clear physical meaning of displacements and tractions at the boundary $\partial\Omega$.

The traction at the point $\mathbf{x}$ on the plane characterized by the normal vector $\mathbf{n}(\mathbf{x})$ can be obtained from Eq. (2.37) by using strain-displacements relations (2.22) and Hooke's law (2.25):

$$t_m(\mathbf{x}) = \int\limits_{\partial\Omega} T_{mj}(\mathbf{x}, \boldsymbol{\xi}) t_j(\boldsymbol{\xi}) dS_\xi - \int\limits_{\partial\Omega} H_{mj}(\mathbf{x}, \boldsymbol{\xi}) u_j(\boldsymbol{\xi}) dS_\xi + \int\limits_{\Omega} T_{mj}(\mathbf{x}, \eta) b_j(\eta) dV_\eta \quad (2.38)$$

where the components T_{mj} are that of the tensor $\mathbf{T}$ (2.28) and the components H_{mj} are of the tensor $\mathbf{H}$ (2.33). Thus, the surface integrals in the right-hand sides of Eqs.(2.37) and (2.38) are combinations of potentials described in Section 2.5.

As noted above (see (2.36)), if the point $\mathbf{x} \notin \Omega$ the left-hand sides of Eq.(2.37) is zero. Similarly, the left-hand side of Eq.(2.38) is zero if the point $\mathbf{x} \notin \Omega$.

Chapter 3

Boundary Integral Equations

3.1 Integral Representation of Boundary Fields

In the following sections the volume integral associated with the body force $\mathbf{b}(\boldsymbol{\eta})$ is omitted. The considerations on its treatment can be found in Appendix A.

3.1.1 Formulation via Combination of Potentials (Indirect)

The solution of a specific elasticity boundary value problem can be sought as a surface potential or a combination of potentials (2.29) – (2.32) defined on the boundary of the domain Ω (indirect formulation, see [27] – [29], [44]). The boundary integral equation in terms of unknown density functions that is equivalent to the boundary value problem can be obtained by using the prescribed boundary data. For closed surfaces, the physical meaning of the unknown densities is unclear, which can make it necessary to perform further calculations to find the boundary displacements and tractions. For these cases, it is more advantageous to use formulation based on Somigliana identities (direct formulation, see e.g. [12, 81, 83]).

3.1.2 Formulation via Somigliana Identities (Direct)

An important advantage of this formulation is clear physical meaning of the boundary unknowns, which allows to avoid calculation of the missing boundary data (densities).

As discussed above, integral identities of Eqs.(2.37) and (2.38) involve potentials given by Eqs.(2.29) – (2.32). These identities are valid for the points $\mathbf{x}$ located inside the domain Ω. The case of $\boldsymbol{\xi_0} \in \partial\Omega$ ($\partial\Omega$ is assumed sufficiently smooth at this point), is treated using the limit properties of the potentials, see Eq.(2.34). This procedure results in the following boundary integral equations (see e.g., [2]):

$$\frac{1}{2}u_m(\boldsymbol{\xi_0}) = \int\limits_{\partial\Omega} U_{mj}(\mathbf{x},\boldsymbol{\xi})t_j(\boldsymbol{\xi})dS_\xi - \fint\limits_{\partial\Omega} T_{jm}(\boldsymbol{\xi},\mathbf{x})u_j(\boldsymbol{\xi})dS_\xi \tag{3.1}$$

$$\frac{1}{2}t_m(\boldsymbol{\xi_0}) = \fint\limits_{\partial\Omega} T_{mj}(\boldsymbol{\xi_0},\boldsymbol{\xi})t_j(\boldsymbol{\xi})dS_\xi - \fint\limits_{\partial\Omega} H_{mj}(\boldsymbol{\xi_0},\boldsymbol{\xi})u_j(\boldsymbol{\xi})dS_\xi \tag{3.2}$$

where the second integral in in the right-hand side of Eq.(3.1) and the first integral in in the right-hand side of Eq.(3.2) are singular Cauchy principal value integrals and a the second integral in in the right-hand side of Eq.(3.2) is a hypersingular Hadamard finite part integral.

Note that for the limits of the integrals in Eq.(3.4) to exist, certain smoothness conditions are required for the boundary $\partial\Omega$ and the approximating functions for $\mathbf{u}$ and $\mathbf{t}$: $\mathbf{u}(\boldsymbol{\xi}), \mathbf{t}(\boldsymbol{\xi}) \in C^{1,\alpha}$ (see [2, 44]).

The solutions of these boundary equations would require evaluation of the invovled singular and hypersingular integrals. In case of numerical integration, special quadrature rules (see e.g. [42] – [45]) would be required for those integrals. Provided that presently there are no universally accepted quadratures for evaluation of hypersingular integrals, a different approach may be more advantageous. In addition, evaluation of the fields inside Ω requires extra integration of the regular integrals involved in Eqs.(2.37) and (2.38).

In an alternative "limit after integration" approach (see e.g. [65] – [67]), i.e. the formulation via the direct limit to the boundary (see Fig. 3.1), the integrals are evaluated before the limits are taken, thus these integrals remain regular. This procedure results in the following boundary equations:

$$u_m(\boldsymbol{\xi_0}) = \lim_{\mathbf{x}\to\boldsymbol{\xi_0}} \int_{\partial\Omega} U_{mj}(\mathbf{x},\boldsymbol{\xi}) t_j(\boldsymbol{\xi}) dS_\xi - \lim_{\mathbf{x}\to\boldsymbol{\xi_0}} \int_{\partial\Omega} T_{jm}(\boldsymbol{\xi},\mathbf{x}) u_j(\boldsymbol{\xi}) dS_\xi \tag{3.3}$$

$$t_m(\boldsymbol{\xi_0}) = \lim_{\mathbf{x}\to\boldsymbol{\xi_0}} \int_{\partial\Omega} T_{mj}(\mathbf{x},\boldsymbol{\xi}) t_j(\boldsymbol{\xi}) dS_\xi - \lim_{\mathbf{x}\to\boldsymbol{\xi_0}} \int_{\partial\Omega} H_{mj}(\mathbf{x},\boldsymbol{\xi}) u_j(\boldsymbol{\xi}) dS_\xi \tag{3.4}$$

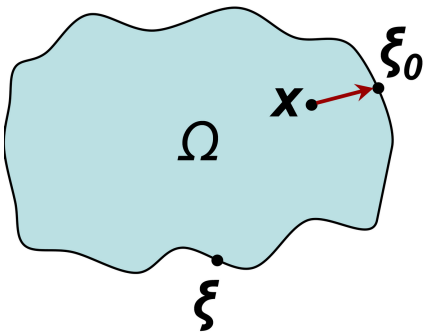

Figure 3.1: An illustration to the "Limit to the boundary" formulation of BIE.

To be able to implement this procedure and evaluate the limits involved in Eqs.(3.3) and (3.4), analytical integration is typically required. However, the benefit of the procedure is that the fields inside the domain are evaluated with the use of the same integration procedures as those for the boundary before the limits are taken. This allows for more compact structure of the computer code. This approach is employed in the present work.

3.2 External (Infinite Domain) Problem

Eqs.(2.37 – 3.4) remain valid for an infinite domain (external problem) under the so-called regularity conditions at infinity (see [2]). For three-dimensional problems, they

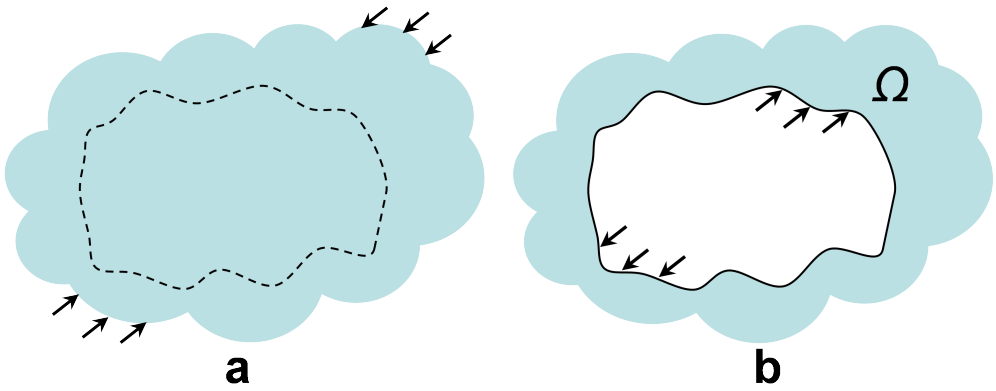

Figure 3.2: a) Infinite space with far-field load, b) Original domain with corrected boundary loads.

require that the fields behave as

$$u_k(\mathbf{x}) = O(\frac{1}{r}); \quad \sigma_{km}(\mathbf{x}) = O(\frac{1}{r^2}) \tag{3.5}$$

as $r = |\mathbf{x}|$ goes to infinity.

In case of applied far-field load, these conditions are not satisfied. In this case, a standard superposition procedure is applied, in which the problem is decomposed into the following two: one of the infinite space under the far-field load and another one of the original infinite domain without far-field load, but with the boundaries additionally loaded by the prescribed corrective tractions ($-\mathbf{t}^{\infty}$) that compensate those induced on the boundaries by the far-field load of the former problem (see Fig. 3.2).

3.3 Treatment of Cracks

The presented formulation can be extended to the case of a domain containing cracks by combining in Eqs.(2.37 – 2.38) the integrals over the external boundary of the domain and the corresponding integrals over the cracks' surface (see [58]).

A crack is treated as the common part of the boundary of two adjacent subdomains (I and II) with the same elastic properties (see Fig. 3.3). The conditions on the artificial

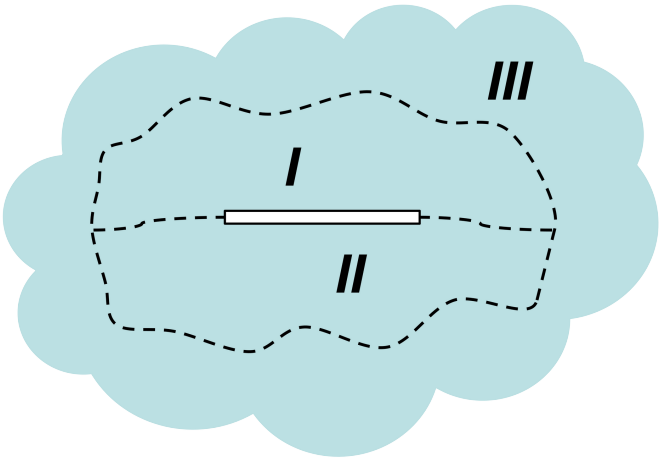

Figure 3.3: The scheme of crack treatment.

boundaries (those complementary to the crack surfaces) are prescribed to provide the continuity of displacement and equilibrium of tractions.

After summation of the traction identities for both subdomains and the surrounding medium (III), the integrals over the complementary boundaries cancel out. The summation results in the identity similar to Eq.(3.2) with $\mathbf{u}$ substituted by the displacement discontinuity $\triangle\mathbf{u} = \mathbf{u}^+ - \mathbf{u}^-$, where "+" and "–" refer to the opposite sides of the crack (see Fig. 3.4).

$$t_m(\boldsymbol{\xi_0}) = -\!\!\!\!\!\!\int\limits_{S_C} H_{mj}(\boldsymbol{\xi_0}, \boldsymbol{\xi}) \triangle u_j(\boldsymbol{\xi}) dS_\xi \tag{3.6}$$

where S_C denotes the crack surface. The traction $\mathbf{t}(\boldsymbol{\xi_0})$ in the left-hand side, as mentioned in the previous Subsection, must include the corrective tractions $(-\mathbf{t}^\infty(\boldsymbol{\xi_0}))$ that compensate those induced by the far-field load on the crack surface.

Alternatively, the right-hand side of Eq.(3.6) can still be understood as the limit of a regular integral:

$$t_m(\boldsymbol{\xi_0}) = -\lim_{\mathbf{x}\to\boldsymbol{\xi_0}} \int\limits_{S_C} H_{mj}(\mathbf{x}, \boldsymbol{\xi}) \triangle u_j(\boldsymbol{\xi}) dS_\xi \tag{3.7}$$

An alternative procedure to obtain the integral equation for a single crack that used

the asymptotic behavior of potentials (2.29) – (2.32) at infinity and symmetry properties of the kernels **U**, **T**, and **H** was used in [83]. It was assumed that Ω is a region whose internal boundary coincides with the crack surfaces S_C^+ and S_C^- and the external one is a sphere of sufficiently large radius.

A similar identity could be obtained using the indirect BEM formulation with the double layer potential. In this case, the unknown density function could be shown to coincide with $\triangle\mathbf{u}$ (see [2]).

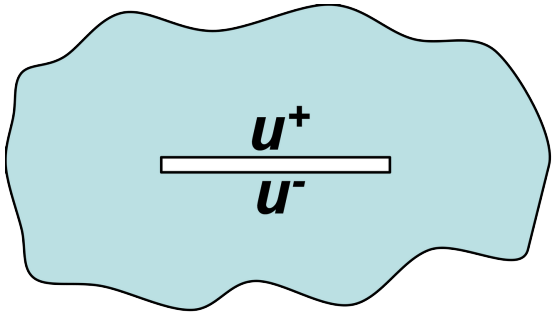

Figure 3.4: Notations for boundary displacements on the crack surface.

The direction of the normal $\mathbf{n}(\boldsymbol{\xi})$ to the crack surface involved in the tensor **H** may be chosen arbitrarily. The convention used in the following analysis is such that this direction indicates the outward normal for the "+" side (and the inward normal for the "–" side) of the crack.

Eqs.(3.6) or (3.7) remain valid for the case when other boundaries are present (e.g. external boundary of a finite body containing cracks or boundaries of the cavities in a finite or infinite domain) provided that $\triangle\mathbf{u}$ is understood as $\triangle\mathbf{u} = \mathbf{u}^+ = \mathbf{u}$, $\mathbf{u}^- = 0$, and the normal $\mathbf{n}(\boldsymbol{\xi})$ is an outward normal, i.e. directed away from the domain of interest.

Similarly, Eq.(3.2) or (3.4) remain valid for the above case if $\partial\Omega$ is understood as the totality of all boundaries including cracks.

In the present work, the "limit after integration" approach is adopted. The governing integral equation is formulated in terms of tractions with the unknown $\triangle\mathbf{u}(\boldsymbol{\xi})$ that

represents displacement discontinuity on the cracks' surfaces and displacement on the remaining boundaries. Thus, for a smooth point $\boldsymbol{\xi_0} \in \partial\Omega$, one has

$$\lim_{\mathbf{x}\to\boldsymbol{\xi_0}} \int_{\partial\Omega} H_{mj}(\mathbf{x},\boldsymbol{\xi}) \triangle u_j(\boldsymbol{\xi}) dS_\xi = \lim_{\mathbf{x}\to\boldsymbol{\xi_0}} \int_{\partial\Omega_B} T_{mj}(\mathbf{x},\boldsymbol{\xi}) t_j(\boldsymbol{\xi}) dS_\xi - t_m(\boldsymbol{\xi_0}) \tag{3.8}$$

where $\partial\Omega_B$ is the totality of non-crack boundaries.

Chapter 4

Boundary Element Method

4.1 Overview

Boundary Element Method is a numerical technique of solving boundary integral equations.

To find the approximate solution of the boundary integral equation, the boundary is discretized, approximating (shape) functions for the unknowns are introduced, the integrals associated with each degree of freedom (and the corresponding shape function) are evaluated. After that, the system of linear algebraic equations is assembled with the use of the "limit after integration" procedure, in which the prescribed boundary data are matched either in weak (Galerkin) sense (see e.g. [16, 17]) or by collocation, i.e. exactly at a discrete set of boundary points.

By solving the system of algebraic equations, the boundary unknowns are found at the nodal points. Substituting them into the corresponding integral identities (reformulated for the discretized boundary), one can evaluate the fields at any point on the boundary or inside the domain. These basic steps are illustrated on Fig. 4.1.

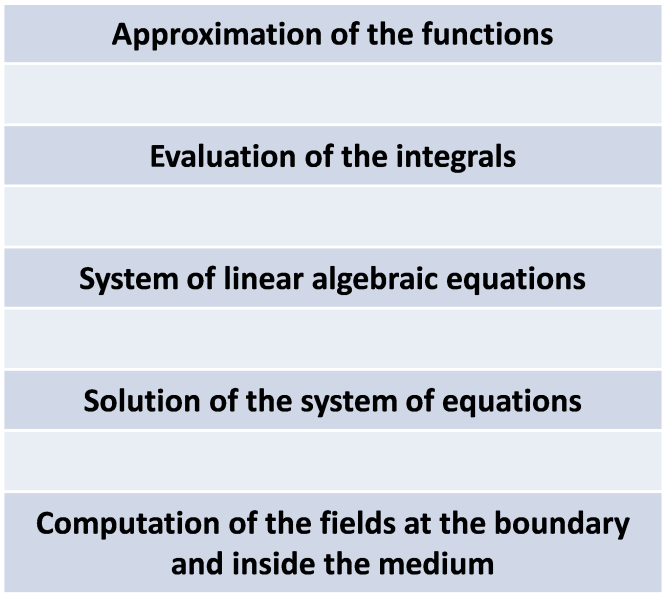

Figure 4.1: Basic steps of Boundary Element Method.

4.2 Implementation Details

In the algorithm presented in this dissertation, the collocation method is implemented together with "limit after integration" approach. Thus, one can consider $\boldsymbol{\xi_0}$ a collocation point and replace $\partial\Omega$ in Eq.(3.8) with the set of discrete boundary elements:

$$\sum_{s=1}^{N_B+N_C} \lim_{\mathbf{x}\to\boldsymbol{\xi_0}} \int_{E_s} H_{jk}(\mathbf{x},\boldsymbol{\xi}) \triangle u_k(\boldsymbol{\xi}) dS_\xi = \sum_{s=1}^{N_B} \lim_{\mathbf{x}\to\boldsymbol{\xi_0}} \int_{E_s} T_{jk}(\mathbf{x},\boldsymbol{\xi}) t_k(\boldsymbol{\xi}) dS_\xi - t_j(\boldsymbol{\xi_0}) \tag{4.1}$$

where E_s is the s-th boundary element, first N_B elements discretize the external boundary of Ω, next N_C elements discretize the totality of the cracks' surface, and $\triangle u_k$ are the components of displacement $\triangle\mathbf{u} = \mathbf{u}^+$ or displacement discontinuity (DD) $\triangle\mathbf{u} = \mathbf{u}^+ - \mathbf{u}^-$ on the former and the latter parts of the boundary, respectively.

In the following subsections, the detailed description of the algorithm is provided.

This includes the details on the integration and the limit procedures.

4.2.1 Discretization of the Boundaries

The boundaries are discretized with planar triangular elements; each element contains 6 nodal points, in which the unknowns are sought. The used arrangements of nodal points are discussed in the next Subsection. It is worth mentioning that the integration method described in Section 4.3 allows for the use of planar elements containing circular arcs as part of their contour (see Appendix C).

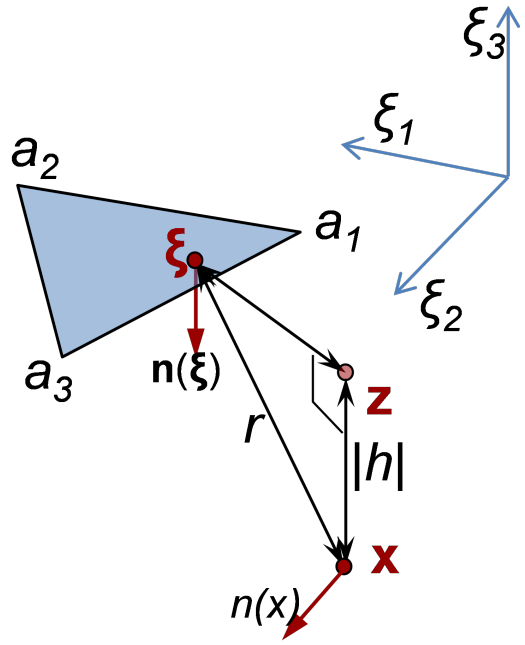

Figure 4.2: Boundary element. Local coordinate system and notations.

The local Cartesian coordinate system is introduced on the considered element E_s as in [58]: $\widehat{\mathbf{e}}_1\widehat{\mathbf{e}}_2\widehat{\mathbf{e}}_3$ is the right-handed orthonormal basis where $\widehat{\mathbf{e}}_1$ is parallel to the edge between two vertices of the element (a_1 and a_2), $\widehat{\mathbf{e}}_3 = -\mathbf{n}(\boldsymbol{\xi})$, and $\widehat{\mathbf{e}}_2 = \widehat{\mathbf{e}}_3 \times \widehat{\mathbf{e}}_1$. The origin of this coordinate system may be chosen arbitrarily, e.g. coinciding with a_1 or the

element's centroid; in the following, it is assumed to be located in the plane containing the element.

In the following, if not stated otherwise, components of vectors and tensors are given in the local coordinate system of E_s (see Fig. 4.2).

4.2.2 Arrangement of Nodes and Collocation Points

In the adopted algorithm, the numbers of nodes and collocation points are equal so each collocation point is somewhat associated with a certain node. The results reported in the next Chapter have been obtained with the following arrangements of nodal and collocation points:

a) continuous approximation: nodal points coincide with the mesh vertices; additional nodes are placed on the edges. No nodes are placed at the vertices located on the crack front curve where zero displacement discontinuity conditions are enforced (that means that the corresponding rows and columns are excluded from the influence matrix). The collocation point associated with a specific node is located inside the element with the largest area among those sharing that node and placed at 1/4 - 1/3 of the distance between the node and the element centroid. Note that such an arrangement may result in some elements containing no collocation points.

b) discontinuous approximation: nodal points coincide with collocation points and are located inside the element at 1/4 - 1/3 of the distances between the vertices and the element centroid.

An example of a mesh (a penny-shaped crack discretized with 40 elements) and arrangements of nodal and collocation points associated with a part of the mesh (a rectangle identified by the dashed line) are shown in Fig. 4.3 for both described arrangement

schemes.

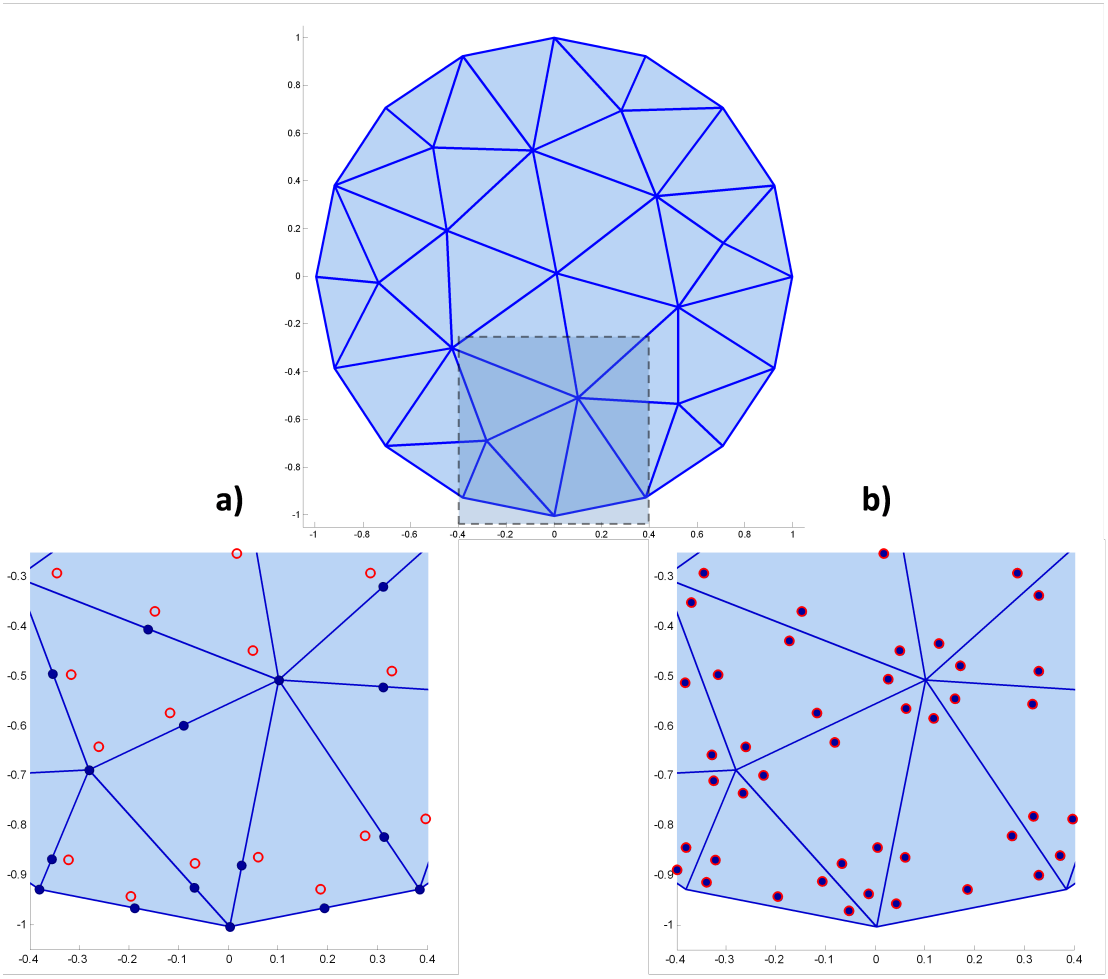

Figure 4.3: Example of the boundary mesh (penny-shaped crack) and two schemes of nodes arrangement: **a**) continuous DD **b**) discontinuous DD.

It should be emphasized that while the approximations adopted in the scheme (**a**) are continuous, they are only sufficiently smooth inside each element but can lack the required smoothness ($\Delta \mathbf{u}(\boldsymbol{\xi}) \in C^{1,\alpha}$) between the elements. Thus, in this scheme, the collocation points can be placed only inside the elements.

Special tip shape functions have not been employed in the reported algorithm. However, the second order approximations for the displacement discontinuity may allow one to capture the asymptotic behavior of stress field near the crack tips, which constant approximations do not. To further facilitate this feature, some nodes of the tip elements can be shifted towards the tip (see Fig. 4.3) in somewhat similar manner as in the so-called "quarter-point elements" used in Finite Element crack analysis.

The positions of the three additional nodes on the edges can be defined via assigning "weights" to the vertices. The edge node is placed at the "center of gravity" of the two ends of the edge. To shift the edge node towards the vertex (e.g. at the crack tip) the "weight" of the latter is increased. In the computer code, the "weights" of the crack tip nodes may be chosen as either 1 or 3; the weights of the other nodes are equal to 1.

4.2.3 Approximation of Unknowns

In the following analysis, quadratic Lagrange polynomials (see Subsection 2.1.3) are used to approximate the distribution of the unknowns (i.e. components of displacement discontinuity $\triangle\mathbf{u}$) over each boundary element. Thus,

$$\triangle u_k(\xi_1, \xi_2) = \sum_{M=1}^{6} \triangle u_k^{(N_M)} L^{(M)}(\xi_1, \xi_2) \tag{4.2}$$

where $\triangle u_k^{(N_M)}$ is the k-th component of $\triangle\mathbf{u}$ at the N_M-th nodal point (M-th node of the element, $M = 1 \ldots 6$) and the approximating (shape) function associated with the N_M-th nodal point can be expressed as follows:

$$L^{(M)}(\xi_1, \xi_2) = \sum_{\substack{m,n=0 \\ m+n\leq 2}}^{2} \gamma_{mn}^{(M)} P_{mn}(\xi_1, \xi_2) \tag{4.3}$$

where $P_{mn}(\xi_1, \xi_2) = \xi_1^m \xi_2^n$, $0 \leq m, n \leq 2$, $m + n \leq 2$, and the coefficients $\gamma_{mn}^{(M)}$ are defined by the following conditions:

$$L^{(M)}(\xi_1^{(Q)}, \xi_2^{(Q)}) = \begin{cases} 1 \; if \; M = Q \\ 0 \; if \; M \neq Q \end{cases} \tag{4.4}$$

where $\xi_1^{(Q)}, \xi_2^{(Q)}$ are the coordinates of the Q-th node of the element in the local coordinate system.

Thus, the distribution of $\triangle u_k$ on the element is determined by its values at 6 nodal points.

Eq.(4.2) can be rewritten in matrix form as follows:

$$\triangle u_k(\xi_1, \xi_2) = [\mathbf{P}_{mn}]^T \cdot \left[\mathbf{F}^{(s)}\right] \cdot \begin{bmatrix} \triangle u_k^{(N_1)} \\ : \\ \triangle u_k^{(N_6)} \end{bmatrix} \tag{4.5}$$

where $N_1 \ldots N_6$ are the nodes associated with the element E_s,

$$[\mathbf{P}_{mn}]^T = [P_{00}(\xi_1, \xi_2),\ P_{10}(\xi_1, \xi_2),\ P_{01}(\xi_1, \xi_2),\ P_{20}(\xi_1, \xi_2),\ P_{02}(\xi_1, \xi_2),\ P_{11}(\xi_1, \xi_2)]$$

the superscript T denotes transposition, and the matrix $\left[\mathbf{F}^{(s)}\right]$ is assembled of the shape functions' coefficients $\gamma_{mn}^{(N)}$ as follows:

$$\left[\mathbf{F}^{(s)}\right] = \begin{bmatrix} \gamma_{00}^{(1)} & \gamma_{00}^{(2)} & \cdots & \gamma_{00}^{(6)} \\ \gamma_{10}^{(1)} & \gamma_{10}^{(2)} & \cdots & \gamma_{10}^{(6)} \\ & \cdots & & \\ \gamma_{02}^{(1)} & \gamma_{02}^{(2)} & \cdots & \gamma_{02}^{(6)} \\ \gamma_{11}^{(1)} & \gamma_{11}^{(2)} & \cdots & \gamma_{11}^{(6)} \end{bmatrix} \tag{4.6}$$

The algorithm for calculation of γ_{mn} implemented in the computer code employs complex notations of Subsection 4.3.1 and is explained in Appendix B.

Since in Eq.(4.5) only the vector of monomials $[\mathbf{P}_{mn}]$ varies with ξ_1 and ξ_2 over the element, the first integral in Eq.4.1 associated with the element E_s can be expressed as follows:

$$\int_{E_s} H_{jk} \triangle u_k(\xi_1, \xi_2) dS_\xi = [\mathbf{I}_{mn}]^T \cdot \left[\mathbf{F}^{(s)}\right] \cdot \begin{bmatrix} \triangle u_k^{(N_1)} \\ : \\ \triangle u_k^{(N_6)} \end{bmatrix} \tag{4.7}$$

where

$$[\mathbf{I}_{mn}]^T = \left[I_{00}^{(s)},\ I_{10}^{(s)},\ I_{01}^{(s)},\ I_{20}^{(s)},\ I_{02}^{(s)},\ I_{11}^{(s)}\right]$$

and

$$I_{mn}^{(s)} = \int_{E_s} H_{jk} \xi_1^m \xi_2^n dS_\xi$$

The integral in the right-hand side of Eq.4.1 involves prescribed tractions and can be evaluated for each element as discussed in Section 4.3.

As mentioned, the system of linear algebraic equations is set by using the standard collocation method. The boundary fields (e.g., tractions) at each collocation point are represented as a sum of the contributions due to all boundary elements (which, in turn, are composed of the contributions due to all degrees of freedom associated with those elements) and matched with the prescribed boundary data at that point. Before the summation, the tractions are transformed from the coordinate system of the element under consideration to the global coordinate system (using the coordinate transformation determined by the orientation of the element [58]).

$$t_m^{(global)} = R_{mk}^{(s)} t_k^{(local)} \tag{4.8}$$

where $R_{mk}^{(s)}$ are the components of the rotation tensor $\mathbf{R^{(s)}}$ expressed as a matrix made of the components of the basis vectors $\widehat{\mathbf{e}}_1, \widehat{\mathbf{e}}_2, \widehat{\mathbf{e}}_3$ of the local coordinate system of the element E_s. The transposed tensor expresses the inverse transform $\mathbf{R^{(s)}}^{-1} = \mathbf{R^{(s)}}^T$.

Similarly, displacements (displacement discontinuities) are transformed as

$$\begin{aligned} \triangle u_m^{(local)} &= R_{km}^{(s)} \triangle u_k^{(global)} \\ \triangle u_m^{(global)} &= R_{mk}^{(s)} \triangle u_k^{(local)} \end{aligned} \tag{4.9}$$

4.2.4 Assembly and Solution of the System of Algebraic Equations

The tractions at any point on the crack/borehole boundary are evaluated using standard superposition procedure in which the contributions of all elements are first transformed into the coordinate system associated with the element on which the boundary point is located and then summed up. By exactly matching the boundary tractions at the collocation points with the prescribed boundary data, the system of linear algebraic equations in terms of unknown displacement discontinuities $\triangle \mathbf{u}^{(N)}$ on the crack elements and displacements $\mathbf{u}^{(N)} = \triangle \mathbf{u}^{(N)} = \mathbf{u}^{+(N)}$ on the other elements is assembled (the terms that involve known tractions $\mathbf{t}^{(N)}$ are transferred to the right-hand side of the system that also includes the influence of the far-field stresses (see also [59]).

The case when cracks emanate from the borehole surface needs special attention because the displacements at the borehole boundary are continuous everywhere except the points where the crack initiates (crack mouth), while they undergo unknown jumps across the crack surface. In order to describe the jumps (displacement discontinuities) at these points, pairs of coincident nodes are introduced. Each of node of the pair is associated with the borehole element located on either "+" or "–" side of the adjacent crack. While considering the crack surface element that contains these points, the difference of displacements at both nodes is considered instead of displacement discontinuity. This procedure results in additional columns (and rows) of the matrix; the integrals associated with the crack surface element adjacent to the borehole contribute to the matrix twice with opposite signs.

In the computer code developed in the present research, the assembly of the system

of linear algebraic equations is implemented with the use of parallel computing to reduce the computational time. The details on implementation of parallelization are provided in Section 4.4.

The system of equations is solved via either direct Gaussian or iterative methods (the MATLAB package and its built-in procedures are used for the present research) to obtain the unknown displacement discontinuities at the nodal points. No fast solver is implemented at this point; it will be a subject of future work.

4.2.5 Evaluation of the Fields in the Domain

After the solution of the system of algebraic equations is found, the stresses inside the domain Ω can be reconstructed using the superposition of the prescribed far-field stress with the stresses given by the following discretized analog of Eq.(2.38) with appropriately chosen normal vectors $\mathbf{n}(\mathbf{x})$:

$$t_m(\mathbf{x}) = \sum_{s=1}^{N_B} \int\limits_{E_s} T_{mj}(\mathbf{x}, \boldsymbol{\xi}) t_j(\boldsymbol{\xi}) dS_\xi - \sum_{s=1}^{N_B+N_C} \int\limits_{E_s} H_{mj}(\mathbf{x}, \boldsymbol{\xi}) \triangle u_j(\boldsymbol{\xi}) dS_\xi \tag{4.10}$$

Note that he integrals involved in (4.10) are regular and can be evaluated using the same procedures as the ones used to assemble the matrix of the system of algebraic equations (influence matrix).

The displacements at the point $\mathbf{x}$ inside the domain of interest can be obtained (up to a rigid body movement) from the discretized analog of Eq.(2.37):

$$u_m(\mathbf{x}) = \sum_{s=1}^{N_B} \int\limits_{E_s} U_{mj}(\mathbf{x}, \boldsymbol{\xi}) t_j(\boldsymbol{\xi}) dS_\xi - \sum_{s=1}^{N_B+N_C} \int\limits_{E_s} T_{jm}(\boldsymbol{\xi}, \mathbf{x}) \triangle u_j(\boldsymbol{\xi}) dS_\xi \tag{4.11}$$

In the present research, the boundary integrals involved in Eqs.(4.1), (4.10), and(4.11) are treated analytically. This also facilitates the "limit after integration" approach, which allows to make use of the same integration procedure twice: in the assembly of the system of algebraic equations and in evaluation of the fields (postprocessing). In the following Section, the detailed description of the integration procedure is provided.

4.3 Analytical Integration over a Boundary Element

The analytical integration technique makes use of the so-called Cauchy-Pompeiu integral formula of Eq.(2.9) (also known as Borel-Pompeiu, Cauchy-Green, or generalized Cauchy formula) that involves complex variable formalism (see Chapter 2). This requires introduction of various complex combinations for the geometrical parameters and the elastic fields.

4.3.1 Assumptions and Complex Nnotations for the Fields and Geometry

The following combinations associated with the vector $\mathbf{r}$ that connects the point $\xi \in E_s$ and the field point $\mathbf{x} = (x_1, x_2, x_3)$ are introduced:

$$z = x_1 + ix_2; \quad \tau = \xi_1 + i\xi_2; \quad h = \xi_3 - x_3 \tag{4.12}$$

where $i^2 = -1$. With notations (4.12) the distance r can be expressed as

$$r = \sqrt{(\tau - z)(\overline{\tau} - \overline{z}) + h^2} \tag{4.13}$$

where the bar over the symbol defines the complex conjugate, i.e. for $z = x_1 + ix_2$, $\overline{z} = x_1 - ix_2$.

For the normal vector $\mathbf{n}(\mathbf{x})$ to the plane containing the point $\mathbf{x}$, the following notations will be used:

$$\underline{n}(\mathbf{x}) = n_1(\mathbf{x}) + in_2(\mathbf{x}); \quad \overline{n}(\mathbf{x}) = n_1(\mathbf{x}) - in_2(\mathbf{x}); \quad n_{\mathbf{n}} = n_3 \tag{4.14}$$

Also, the following combinations of similar kind for traction and displacement (displacement discontinuity) components can be introduced:

$$\begin{aligned} &\underline{t} = t_1 + it_2; && \overline{t} = t_1 - it_2; && t_{\mathbf{n}} = t_3 \\ &\underline{u} = \Delta u_1 + i\Delta u_2; && \overline{u} = \Delta u_1 - i\Delta u_2; && u_{\mathbf{n}} = \Delta u_3 \end{aligned} \tag{4.15}$$

With these notations, the shape function of Eq.(4.3) can be expressed as

$$L^{(M)}(\tau,\overline{\tau}) = \sum_{\substack{m,n=0 \\ m+n\leq 2}}^{2} \kappa_{mn}^{(M)} (\tau - z)^m (\overline{\tau} - \overline{z})^n \tag{4.16}$$

where τ and $\overline{\tau}$ are understood as independent variables, the superscript $M = 1 \dots 6$ identifies the node, and the coefficients $\kappa_{mn}^{(M)} = \overline{\kappa_{nm}^{(M)}}$ can be obtained from $\gamma_{mn}^{(M)}$, which are defined by the arrangement of the nodes on the element E_s.

The combinations $\underline{u}, \overline{u}$ and $u_{\mathbf{n}}$ on the element can be expressed via their values at the corresponding nodes; the matrix forms of these expressions are similar to those of Eq.(4.5):

$$\begin{aligned}
\underline{u}(\tau,\overline{\tau}) &= [\boldsymbol{\tau}]^T \cdot \left[\widetilde{\mathbf{F}}^{(s)}\right] \cdot \begin{bmatrix} \underline{u}^{(N_1)} \\ \vdots \\ \underline{u}^{(N_6)} \end{bmatrix} \\
\overline{u}(\tau,\overline{\tau}) &= [\boldsymbol{\tau}]^T \cdot \left[\widetilde{\mathbf{F}}^{(s)}\right] \cdot \begin{bmatrix} \overline{u}^{(N_1)} \\ \vdots \\ \overline{u}^{(N_6)} \end{bmatrix} \\
u_{\mathbf{n}}(\tau,\overline{\tau}) &= [\boldsymbol{\tau}]^T \cdot \left[\widetilde{\mathbf{F}}^{(s)}\right] \cdot \begin{bmatrix} u_{\mathbf{n}}^{(N_1)} \\ \vdots \\ u_{\mathbf{n}}^{(N_6)} \end{bmatrix}
\end{aligned} \tag{4.17}$$

where $N_1 \dots N_6$ are the nodes associated with the element E_s, $[\boldsymbol{\tau}]^T$ is the following transposed vector of the monomials $(\tau - z)^m (\overline{\tau} - \overline{z})^n$:

$$[\boldsymbol{\tau}]^T = \left[1,\ \tau - z,\ \overline{\tau} - \overline{z},\ (\tau - z)^2,\ (\overline{\tau} - \overline{z})^2,\ (\tau - z)(\overline{\tau} - \overline{z})\right]$$

and the matrix $\left[\widetilde{\mathbf{F}}^{(s)}\right]$ is assembled of the shape functions' coefficients $\kappa_{mn}^{(N)}$ as follows

(see Appendix B for details):

$$\left[\widetilde{\mathbf{F}}^{(s)}\right] = \begin{bmatrix} \kappa_{00}^{(1)} & \kappa_{00}^{(2)} & \dots & \kappa_{00}^{(6)} \\ \kappa_{10}^{(1)} & \kappa_{10}^{(2)} & \dots & \kappa_{10}^{(6)} \\ & \dots & & \\ \kappa_{02}^{(1)} & \kappa_{02}^{(2)} & \dots & \kappa_{02}^{(6)} \\ \kappa_{11}^{(1)} & \kappa_{11}^{(2)} & \dots & \kappa_{11}^{(6)} \end{bmatrix} \tag{4.18}$$

Similar representations can be applied to the combinations of tractions. Thus, the integrals in Eq.4.1 associated with the element E_s

$$\int\limits_{E_s} H_{jk} \triangle u_k(\xi_1, \xi_2) dS_\xi, \int\limits_{E_s} T_{jk} t_k(\xi_1, \xi_2) dS_\xi$$

can be expressed via the following ones:

$$\int\limits_{E_s} H_{jk} (\tau - z)^m (\overline{\tau} - \overline{z})^n dS, \int\limits_{E_s} T_{jk} (\tau - z)^m (\overline{\tau} - \overline{z})^n dS$$

in a way similar to that described in Subsection 4.2.3.

4.3.2 Structure of the Integrals over an Element

It can be shown that, with the use of the above complex notations, the components of kernels **T** and **H** with respect to the local coordinate system of the element can be expressed as linear combinations of rational expressions of the following kind:

$$\frac{(\tau - z)^m (\overline{\tau} - \overline{z})^n}{r^k}$$

with the coefficients depending on parameters such as h, $\underline{n}(\mathbf{x})$, $\overline{n}(\mathbf{x})$, $n_{\mathbf{n}}(\mathbf{x})$, μ, and ν. E.g., H_{12} can be expressed as follows:

$$\begin{aligned} H_{12}(\mathbf{x},\boldsymbol{\xi}) = \frac{\mu}{4\pi(1-\nu)}\Bigg\{ & 3ih(1-3\nu)\frac{\overline{n}(\mathbf{x})(\tau-z)-\underline{n}(\mathbf{x})(\overline{\tau}-\overline{z})}{4r^5} \\ & + 3ih(1-\nu)\frac{\underline{n}(\mathbf{x})(\tau-z)-\overline{n}(\mathbf{x})(\overline{\tau}-\overline{z})}{4r^5} \\ & + 15ih\underline{n}(\mathbf{x})\frac{(\overline{\tau}-\overline{z})^3-(\tau-z)^2(\overline{\tau}-\overline{z})}{8r^7} \\ & + 15ih\overline{n}(\mathbf{x})\frac{(\tau-z)(\overline{\tau}-\overline{z})^2-(\tau-z)^3}{8r^7} \\ & - 3in_{\mathbf{n}}(\mathbf{x})(5h^2-\nu r^2)\frac{(\tau-z)^2-(\overline{\tau}-\overline{z})^2}{4r^7}\Bigg\} \end{aligned} \tag{4.19}$$

Thus, with the used polynomial approximations of the unknowns, the contribution of the element E_s into Eq. (4.10) can be represented as a combination of the integrals of the following type:

$$I_{m,n,k} = \int_{E_s} \frac{(\tau-z)^m(\overline{\tau}-\overline{z})^n}{r^k} dS,\ k = 3,\ 5,\ 7 \tag{4.20}$$

The set of typical integrals involved in Eqs.(4.1) and (4.10) with constant, linear, and quadratic approximating functions for the unknown displacement discontinuities is shown on Fig. 4.4.

Note that the integrals (4.20) have the following symmetry property:

$$I_{m,n,k} = \overline{I_{n,m,k}} \tag{4.21}$$

which allows one to save effort of evaluation of the integrals with $n > m$ by taking the complex conjugates of the final closed-form expressions of their counterparts instead.

It is also useful to separate the tractions associated with the combinations $\underline{n}(\mathbf{x})$, $\overline{n}(\mathbf{x})$, and $n_{\mathbf{n}}(\mathbf{x})$ of Eq.(4.14). The resulting combinations, two of which are complex valued and the other two are real valued, can be used either to evaluate the tractions at the collocation points or to calculate stresses inside the domain. Note that to complete

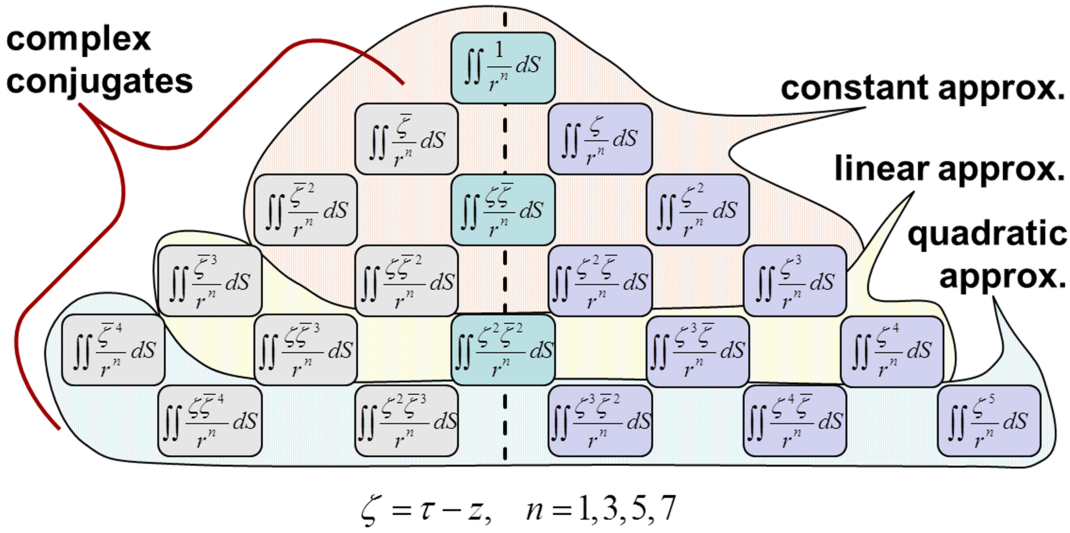

Figure 4.4: Hierarchy of integrals (4.20).

the first procedure, the corresponding limits to the boundary must be also evaluated (see Subection 4.3.4).

After substituting the shape function of Eq.(B.1) into Eq.(4.10), the contributions of the element E_s due to the singular kernel $\mathbf{T}$ (first integral of Eq.(4.10)) to the traction combinations associated with $\underline{n}(\mathbf{x})$, $\overline{n}(\mathbf{x})$, and $n_{\mathbf{n}}(\mathbf{x})$ are as follows:

$$
\begin{aligned}
t^{(T1)}(\mathbf{x}) = \sigma_{13}(\mathbf{x}) + i\sigma_{23}(\mathbf{x}) = \\
2\beta \sum_{N=1}^{6} \sum_{\substack{m,n=0 \\ m+n\leq 2}}^{2} \kappa_{mn}^{(N)} \Bigg\{ & - t_{\mathbf{n}}^{(N)} \left[(1-2\nu) I_{m+1,n,3} + 3h^2 I_{m+1,n,5} \right] \\
& + \underline{t}^{(N)} \left[-\frac{h(5-4\nu)}{2} I_{m,n,3} + \frac{3h^3}{2} I_{m,n,5} \right] \\
& - \overline{t}^{(N)} \left[\frac{3h}{2} I_{m+2,n,5} \right] \Bigg\}
\end{aligned}
\tag{4.22}
$$

$$t^{(T2)}(\mathbf{x}) = \sigma_{11}(\mathbf{x}) - \sigma_{22}(\mathbf{x}) + 2i\sigma_{12}(\mathbf{x}) =$$
$$2\beta \sum_{N=1}^{6} \sum_{\substack{m,n=0 \\ m+n\leq 2}}^{2} \kappa_{mn}^{(N)} \Bigg\{ - t_{\mathbf{n}}^{(N)} \left[3hI_{m+2,n,5} \right] - \underline{t}^{(N)} \left[2(1-2\nu) I_{m+1,n,3} + \frac{3}{2} I_{m+2,n+1,5} \right] - \overline{t}^{(N)} \left[\frac{3}{2} I_{m+3,n,5} \right] \Bigg\} \tag{4.23}$$

$$t^{(T3)}(\mathbf{x}) = \sigma_{11}(\mathbf{x}) + \sigma_{22}(\mathbf{x}) =$$
$$2\beta \sum_{N=1}^{6} \sum_{\substack{m,n=0 \\ m+n\leq 2}}^{2} \kappa_{mn}^{(N)} \Bigg\{ t_{\mathbf{n}}^{(N)} \left[-h(1+4\nu) I_{m,n,3} + 3h^3 I_{m,n,5} \right] - \underline{t}^{(N)} \left[\frac{3}{2} I_{m+1,n+2,5} \right] - \overline{t}^{(N)} \left[\frac{3}{2} I_{m+2,n+1,5} \right] \Bigg\} \tag{4.24}$$

$$t^{(T4)}(\mathbf{x}) = \sigma_{33}(\mathbf{x}) =$$
$$2\beta \sum_{N=1}^{6} \sum_{\substack{m,n=0 \\ m+n\leq 2}}^{2} \kappa_{mn}^{(N)} \Bigg\{ - t_{\mathbf{n}}^{(N)} \left[h(1-2\nu) I_{m,n,3} + 3h^3 I_{m,n,5} \right] + \underline{t}^{(N)} \left[\frac{(1-2\nu)}{2} I_{m,n+1,3} - \frac{3}{2} h^2 I_{m,n+1,5} \right] + \overline{t}^{(N)} \left[\frac{(1-2\nu)}{2} I_{m+1,n,3} - \frac{3}{2} h^2 I_{m+1,n,5} \right] \Bigg\} \tag{4.25}$$

where $\beta = \frac{1}{16\pi(1-\nu)}$.

For the part of Eq.(4.10) associated with the hypersingular kernel $\mathbf{H}$, the corresponding contributions of the element E_s are

$$
\begin{aligned}
t^{(H1)}(\mathbf{x}) = \sigma_{13}(\mathbf{x}) + i\sigma_{23}(\mathbf{x}) = \\
2\beta\mu \sum_{N=1}^{6} \sum_{\substack{m,n=0 \\ m+n\leq 2}}^{2} \kappa_{mn}^{(N)} \Big\{ & \underline{u}^{(N)} \Big[(\nu-2) I_{m,n,3} - 3\nu h^2 I_{m,n,5} - 15 h^4 I_{m,n,7} \Big] \\
& + \overline{u}^{(N)} \Big[-3\nu I_{2+m,n,5} + 15 h^2 I_{2+m,n,7} \Big] \\
& + u_{\mathbf{n}}^{(N)} \Big[-6h I_{1+m,n,5} + 30 h^3 I_{1+m,n,7} \Big] \Big\}
\end{aligned} \tag{4.26}
$$

$$
\begin{aligned}
t^{(H2)}(\mathbf{x}) = \sigma_{11}(\mathbf{x}) - \sigma_{22}(\mathbf{x}) + 2i\sigma_{12}(\mathbf{x}) = \\
2\beta\mu \sum_{N=1}^{6} \sum_{\substack{m,n=0 \\ m+n\leq 2}}^{2} \kappa_{mn}^{(N)} \Big\{ & \underline{u}^{(N)} \Big[-12\nu h I_{1+m,n,5} + 15 h I_{2+m,1+n,7} \Big] \\
& + \overline{u}^{(N)} \Big[15 h I_{3+m,n,7} \Big] \\
& + u_{\mathbf{n}}^{(N)} \Big[6(2\nu-1) I_{2+m,n,5} + 30 h^2 I_{2+m,n,7} \Big] \Big\}
\end{aligned} \tag{4.27}
$$

$$
\begin{aligned}
t^{(H3)}(\mathbf{x}) = \sigma_{11}(\mathbf{x}) + \sigma_{22}(\mathbf{x}) = \\
4\beta\mu \sum_{N=1}^{6} \sum_{\substack{m,n=0 \\ m+n\leq 2}}^{2} \kappa_{mn}^{(N)} \Big\{ & \underline{u}^{(N)} \Big[6(\nu-1) h I_{m,1+n,5} + 15 h I_{1+m,2+n,7} \Big] \\
& + \overline{u}^{(N)} \Big[6(\nu-1) h I_{1+m,n,5} + 15 h I_{2+m,1+n,7} \Big] \\
& + u_{\mathbf{n}}^{(N)} \Big[-(2\nu+1) I_{m,n,3} \\
& \qquad + 6(\nu+2) h^2 I_{m,n,5} - 15 h^4 I_{m,n,7} \Big] \Big\}
\end{aligned} \tag{4.28}
$$

$$t^{(H4)}(\mathbf{x}) = \sigma_{33}(\mathbf{x}) =$$
$$4\beta\mu \sum_{N=1}^{6} \sum_{\substack{m,n=0 \\ m+n\leq 2}}^{2} \kappa_{mn}^{(N)} \Big\{ \underline{u}^{(N)} \Big[-3hI_{m,1+n,5} + 15h^3 I_{m,1+n,7} \Big]$$
$$+ \overline{u}^{(N)} \Big[-3hI_{1+m,n,5} + 15h^3 I_{1+m,n,7} \Big]$$
$$+ u_{\mathbf{n}}^{(N)} \Big[-I_{m,n,3} - 6h^2 I_{m,n,5} + 15h^4 I_{m,n,7} \Big] \Big\} \tag{4.29}$$

The integrals of Eq.(4.20) can be obtained from the following generic integral:

$$I_{mn} = I_{m,n,1} = \int_{E_s} \frac{(\tau - z)^m (\overline{\tau} - \overline{z})^n}{r} dS \tag{4.30}$$

by differentiation over h^2 as follows:

$$\begin{aligned} I_{m,n,3} &= -2 \frac{\partial}{\partial (h^2)} I_{mn} \\ I_{m,n,5} &= \frac{4}{3} \frac{\partial^2}{\partial (h^2)^2} I_{mn} \\ I_{m,n,7} &= -\frac{8}{15} \frac{\partial^3}{\partial (h^2)^3} I_{mn} \end{aligned} \tag{4.31}$$

In the next Subsection, the evaluation of generic integral (4.30) for triangular elements is described. Extension of the integration technique to elements containing circular arcs as parts of the contour is discussed in Appendix C.

4.3.3 Evaluation of the Generic Integral

Area integral (4.30) can be reduced to a contour integral with the use of Cauchy-Pompeiu (Borel-Pompeiu) representation formula of Eq.(2.9) in combination with Sokhotski-Plemelj formulae (2.11) (in case when the point $\mathbf{x}$ is projected to a point $\mathbf{z}_0 \in \partial E_s$). In

order to do this, one should find the fiunction $f(\tau,\overline{\tau})$ such that $\frac{\partial f(\tau,\overline{\tau})}{\partial\overline{\tau}}\Big/(\tau-z)$ is equal to the integrand in Eq.(4.30). Note that this function does not have to be holomorphic. In can be shown that, for the triangular element E_s, one has

$$I_{mn}=\int\limits_{E_s}\frac{(\tau-z)^m(\overline{\tau}-\overline{z})^n}{r}dS=\frac{1}{2i}\int\limits_{\partial E_s}\frac{f(\tau,\overline{\tau})d\tau}{\tau-z}-\begin{cases}\pi f(z) & \mathbf{z}\in E_s\\ \frac{\gamma}{2}f(z) & \mathbf{z}\in\partial E_s\\ 0 & \mathbf{z}\notin E_s\end{cases}\tag{4.32}$$

where $f(\tau,\overline{\tau})$ is given by the following expression:

$$f(\tau,\overline{\tau})=\begin{cases}-2(r/h^2)(\tau-z)^{m+1}\,(\overline{\tau}-\overline{z})^{n+1}\;{}_2F_1\left(1,n+\frac{3}{2},\frac{3}{2},\frac{r^2}{h^2}\right), & h\neq 0,\\ -2r(2n+1)^{-1}(\tau-z)^m\,(\overline{\tau}-\overline{z})^n\,, & h=0,\end{cases}\tag{4.33}$$

in which ${}_2F_1$ is the hypergeometric function [21].

For particular cases of n and m involved in constant, linear, and quadratic approximations for the unknown functions, $f(\tau,\overline{\tau})$ of (4.33) can be presented in closed form (for any h) as follows:

$$f(\tau,\overline{\tau})=\begin{cases}2r(\tau-z)^m & n=0\\ \frac{2}{3}r(r^2-3h^2)(\tau-z)^{m-1} & n=1\\ \frac{2}{15}r(3r^4-10h^2r^2+15h^4)(\tau-z)^{m-2} & n=2\end{cases}\tag{4.34}$$

By virtue of Eq.(4.21), the choice of the indices m and n in the above expressions can be limited to the cases of $m\geq n$. This is important to assure that the power exponents of the monomials involved in Eq.(4.34) are not negative and therefore the behavior of $f(\tau,\overline{\tau})$ is not singular as $\tau\to z$.

Note that the countour integral involved in Eq.(4.32) is path-dependent, as the function $\frac{f(\tau,\overline{\tau})}{\tau-z}$ is, in general, not holomorphic. For the triangular element E_s, $\partial E_s=\bigcup\limits_{p=1}^{3}[\mathbf{a}_p,\mathbf{b}_p]$, $\mathbf{b}_p=\mathbf{a}_{p+1}$, $\mathbf{b}_3=\mathbf{a}_1$, $a_p=a_{1p}+ia_{2p}$, $b_p=b_{1p}+ib_{2p}$, and the contour integral can be evaluated as a sum of integrals over the three sides of the triangle. For each

side (straight segment with the beginning point $\mathbf{a_p}$ and the end point $\mathbf{b_p}$), the variable τ and its conjugate are related through the following equation (that defines a specific integration path):

$$\overline{\tau} = \overline{a}_p + \frac{\overline{b}_p - \overline{a}_p}{b_p - a_p}(\tau - a_p) \tag{4.35}$$

Thus, the distance r can be expressed via the following rational function of τ:

$$r(\tau) = \sqrt{(\tau - z)\left[D_p\,(\tau - z) + 2\overline{d}_p\right] + h^2} \tag{4.36}$$

where $D_p = (\overline{b}_p - \overline{a}_p)/(b_p - a_p)$ and $d_p = d_{1p} + id_{2p} = \frac{1}{2}\left[a_p - z - \overline{D}_p(\overline{a}_p - \overline{z})\right]$. Note that the latter has the meaning of complex combination of the components of the vector originating at the point $\mathbf{z}$ and perpendicular to the contour segment $[\mathbf{a}_p, \mathbf{b}_p]$ (see Fig. 4.5). Also note that $|d_p| = 0$ if $\mathbf{z} \in (\mathbf{a}_p, \mathbf{b}_p)$, and $D_p = -\overline{d}_p/d_p$ if $\mathbf{z} \notin [\mathbf{a}_p, \mathbf{b}_p]$.

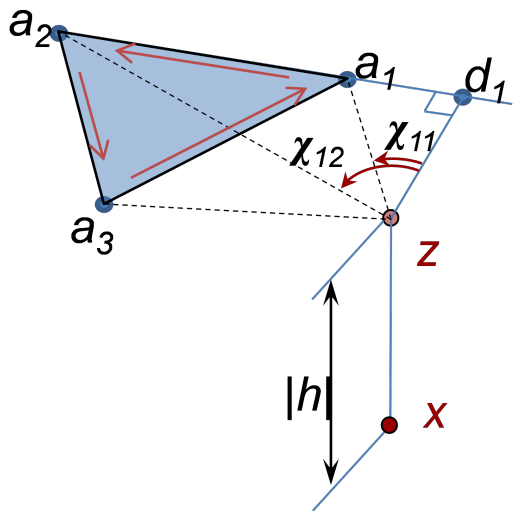

Figure 4.5: Boundary element. Contour integration scheme and notations.

With the above notations, expressions for the function f of (4.34) can be rewritten

as follows:

$$f(\tau,\overline{\tau}) = \begin{cases} 2r(\tau)(\tau-z)^m & n=0 \\ \frac{2}{3}r(\tau)\left[D_p(\tau-z)^{m+1} + 2\overline{d}_p(\tau-z)^m - 2h^2(\tau-z)^{m-1}\right] & n=1 \\ \frac{2}{15}r(\tau)\left[3D_p^2(\tau-z)^{m+2} + 12\overline{d}_p D_p(\tau-z)^{m+1}\right. & \\ \left. -4D_p(3|d_p|^2+h^2)(\tau-z)^m - 8\overline{d}_p h^2(\tau-z)^{m-1} + 8h^4(\tau-z)^{m-2}\right] & n=2 \end{cases} \tag{4.37}$$

Substitution of expressions (4.37) into Eq.(4.32) results, for all cases of n, in the integrals of the same following type:

$$J_{k,p}(z) = \int_{a_p}^{b_p} r(\tau)(\tau-z)^k d\tau \tag{4.38}$$

with $-1 \leq k \leq 4$.

The results of analytical integration of (4.38) are reported in [54]. Here, the final closed-form expressions for the total integral over the contour ∂E_s are provided:

$$J_k = \int_{\partial E_s} r(\tau)(\tau-z)^k d\tau = \sum_{p=1}^{3} \begin{cases} \left[-|d_p|L_0 - |h|\,G_0\right]|_{\tau=a_p}^{\tau=b_p} & k=-1 \\ \frac{1}{2}\left[rd_p + C_m(|d_p|^2+h^2)L_0\right]\Big|_{\tau=a_p}^{\tau=b_p} & k=0 \\ \frac{\overline{D}_p}{k+2}\left[r^3(\tau-z)^{k-1}\Big|_{\tau=a_p}^{\tau=b_p} - \overline{d}_p(2k+1)J_{k-1,p}(z)\right. & \\ \left. -h^2(k-1)J_{k-2,p}(z)\right] & k\geq 1 \end{cases} \tag{4.39}$$

where $C_p = \frac{b_p-a_p}{|b_p-a_p|}$ and L_0, G_0 are given by the following expressions:

$$L_0 = \begin{cases} \tan^{-1}\frac{|d_p|(d_p-\tau+z)}{dr} & \mathbf{z} \notin [\mathbf{a}_p, \mathbf{b}_p] \\ \sinh^{-1}\frac{\tau-z}{|h|} & \mathbf{z} \in (\mathbf{a}_p, \mathbf{b}_p) \end{cases}$$

$$G_0 = \begin{cases} \tanh^{-1}\frac{|h|(d_p-\tau+z)}{d_p r} & \mathbf{z} \notin [\mathbf{a}_p, \mathbf{b}_p] \\ \ln\frac{r+|h|}{|\tau-z|} & \mathbf{z} \in (\mathbf{a}_p, \mathbf{b}_p) \end{cases} \tag{4.40}$$

The integral involved in (4.39) for $k=-1$ and $\mathbf{z} \in (\mathbf{a}_p, \mathbf{b}_p)$ is understood as Cauchy principal value integral.

The integrals (4.39) should be assembled using Eq.(4.37) as follows:

$$\int_{\partial E_s} \frac{f(\tau,\overline{\tau})d\tau}{\tau - z} = \begin{cases} 2J_{m-1} & n=0 \\ \frac{2}{3}\left[D_p J_m + 2\overline{d}_p J_{m-1} - 2h^2 J_{m-2}\right] & n=1 \\ \frac{2}{15}\left[3D_p^2 J_{m+1} + 12\overline{d}_p D_p J_m - 4D_p(3|d_p|^2 + h^2)J_{m-1}\right. & \\ \left. -8\overline{d}_p h^2 J_{m-2} + 8h^4 J_{m-3}\right] & n=2 \end{cases} \tag{4.41}$$

and substituted into Eq.(4.32) to get the final closed-form expression of the integral (4.30).

4.3.4 Evaluation of Boundary Tractions (Limits to the Boundary)

The expressions for $t^{(T1)}(\mathbf{x}) - t^{(T4)}(\mathbf{x})$ and $t^{(H1)}(\mathbf{x}) - t^{(H4)}(\mathbf{x})$ of Eqs.(4.22 – 4.29) represent the case when the point $\mathbf{x}$ is located outside of the crack surface. To meet the prescribed tractions on that surface and obtain the unknown displacements or displacement discontinuities, one has to perform a limiting procedure in which the point $\mathbf{x}$ is allowed to reach some point on the surface. This procedure is, in fact, straightforward, except for the case when this point belongs to the element or is located on the plane that contains it; in this case, the limits of tractions can be taken assuming that $\mathbf{x} \to \mathbf{z}$ or $h \to 0$.

As mentioned in Subection 4.2.2, $\mathbf{z}$ must be an internal point of the element. Although some particular integrals involved in Eqs.(4.22 – 4.29) may diverge when $h \to 0$, the divergent terms cancel out after the assembly, which leads to finite closed-form expressions for $t^{(T1)}(\mathbf{x}) - t^{(T4)}(\mathbf{x})$ and $t^{(H1)}(\mathbf{x}) - t^{(H4)}(\mathbf{x})$. Note that the limits of the former four combinations depend on the direction of approach to the boundary, as discussed in Section 2.5. In the algorithm, this direction is chosen as that of the external normal to the surface.

The final expressions for the limits of Eqs.(4.22 – 4.25) are as follows:

$$
\begin{aligned}
t^{(T1)}(\mathbf{z}) =& 2\beta(1-2\nu)\sum_{N=1}^{6}\sum_{p=1}^{3}\left[\widehat{U}_{pq}^{(N)}+i\widehat{V}_{pq}^{(N)}\right]t_{\mathbf{n}}^{(N)}\Big\|_{q=p}^{p+1} \pm 2\beta(1-\nu)\underline{t}^{(N)}\kappa_{00}^{(N)}\gamma \\
t^{(T2)}(\mathbf{z}) =& \beta\sum_{N=1}^{6}\sum_{p=1}^{3}\Bigg[(7-8\nu)\left(\widehat{U}_{pq}^{(N)}+i\widehat{V}_{pq}^{(N)}+\frac{5}{2}ic_pE_{pq}\kappa_{00}^{(N)}\right)\underline{t}^{(N)} \\
&+\left(\widehat{X}_{pq}^{(N)}+i\widehat{Y}_{pq}^{(N)}\right)\bar{t}^{(N)}\Bigg]\Big\|_{q=p}^{p+1} \\
t^{(T3)}(\mathbf{z}) =& \beta\sum_{N=1}^{6}\sum_{p=1}^{3}\left[6\mathrm{Re}(\widehat{U}_{pq}^{(N)}\bar{t}^{(N)})+i\mathrm{Im}(\widehat{W}_{pq}^{(N)}\bar{t}^{(N)})\right]\Big\|_{q=p}^{p+1} \\
&\mp 4\beta\nu t_{\mathbf{n}}^{(N)}\kappa_{00}^{(N)}\gamma \\
t^{(T4)}(\mathbf{z}) =& 2\beta(2\nu-1)\sum_{N=1}^{6}\sum_{p=1}^{3}\left[\mathrm{Re}(\widehat{U}_{pq}^{(N)}\bar{t}^{(N)})+i\mathrm{Im}(\widehat{V}_{pq}^{(N)}\bar{t}^{(N)})\right]\Big\|_{q=p}^{p+1} \\
&\pm 2\beta(1-\nu)t_{\mathbf{n}}^{(N)}\kappa_{00}^{(N)}\gamma
\end{aligned}
\tag{4.42}
$$

where "+" or "–" signs are taken depending on the direction of approach to the boundary,

$$
\begin{aligned}
\widehat{U}_{pq}^{(N)} =& L_{pq}\left[2c_p\kappa_{00}^{(N)}+2|d_p|\left(c_p^2\kappa_{10}^{(N)}-\kappa_{01}^{(N)}\right)+|d_p|^2\left(3c_p^3\kappa_{20}^{(N)}-\overline{c_p}\kappa_{02}^{(N)}-c_p\kappa_{11}^{(N)}\right)\right] \\
\widehat{V}_{pq}^{(N)} =& 4c_p^2|d_p|E_{pq}\kappa_{10}^{(N)}+c_p^2P_{pq}\kappa_{20}^{(N)}+|d_p|\rho_q\left(\overline{c_p}\kappa_{02}^{(N)}+c_p\kappa_{11}^{(N)}\right) \\
\widehat{W}_{pq}^{(N)} =& 5|d_p|E_{pq}\kappa_{00}^{(N)}+24c_p^2|d_p|E_{pq}\kappa_{10}^{(N)}+6c_p^3P_{pq}\kappa_{20}^{(N)}+6|d_p|\rho_q\left(\overline{c_p}\kappa_{02}^{(N)}+c_p\kappa_{11}^{(N)}\right) \\
\widehat{X}_{pq}^{(N)} =& c_p^2\left[-2c_p\kappa_{00}^{(N)}-6|d_p|\left(c_p^2\kappa_{10}^{(N)}-\kappa_{01}^{(N)}\right)-3|d_p|^2\left(5c_p^3\kappa_{20}^{(N)}+\overline{c_p}\kappa_{02}^{(N)}-3c_p\kappa_{11}^{(N)}\right)\right] \\
\widehat{Y}_{pq}^{(N)} =& c_p^3\left(4+\frac{1}{2}E_{pq}^2\right)\kappa_{00}^{(N)}-4c_p^4|d_p|\left(3-E_{pq}^2\right)\kappa_{10}^{(N)}+12c_p^2|d_p|E_{pq}\kappa_{01}^{(N)} \\
&-c_p^5|d_p|\rho_q\left(15+10E_{pq}^2-2E_{pq}^4\right)\kappa_{20}^{(N)}-3c_p|d_p|\rho_q\kappa_{02}^{(N)}+3c_p^3|d_p|P_{pq}\kappa_{11}^{(N)}
\end{aligned}
\tag{4.43}
$$

and

$$
\begin{aligned}
L_{pq} =& \tanh^{-1}(\sin\chi_{pq}) \\
=& \left(\log(1+\sin\chi_{pq}) - \log(1-\sin\chi_{pq})\right)/2 \\
P_{pq} =& 4|d_p|E_{pq} + \rho_q \\
E_{pq} =& \exp(i\chi_{pq}) \\
\gamma =& \sum_{p=1}^{3} \chi_{pq} \Bigg\|_{q=p}^{p+1} \\
\chi_{pq} =& \arg(a_q) - \arg(d_p) \\
c_p =& \frac{d_p}{|d_p|} \\
\rho_q =& \|\mathbf{a}_q - \mathbf{z}\| = \frac{|d_p|}{\cos\chi_{pq}}
\end{aligned}
\tag{4.44}
$$

The limit expressions for (4.26 – 4.29) are as follows:

$$
\begin{aligned}
t^{(H1)}(\mathbf{z}) =& \beta\mu \sum_{N=1}^{6} \left[(2-\nu)U_{pq}^{(N)}\underline{u}^{(N)} + 2\nu V_{pq}^{(N)}\overline{u}^{(N)}\right] \Bigg\|_{q=p}^{p+1} \\
t^{(H2)}(\mathbf{z}) =& 4\beta\mu \sum_{N=1}^{6} (1-2\nu)V_{pq}^{(N)}u_{\mathbf{n}}^{(N)} \Bigg\|_{q=p}^{p+1} \\
t^{(H3)}(\mathbf{z}) =& 2\beta\mu \sum_{N=1}^{6} (1+2\nu)U_{pq}^{(N)}u_{\mathbf{n}}^{(N)} \Bigg\|_{q=p}^{p+1} \\
t^{(H4)}(\mathbf{z}) =& 4\beta\mu \sum_{N=1}^{6} U_{pq}^{(N)}u_{\mathbf{n}}^{(N)} \Bigg\|_{q=p}^{p+1}
\end{aligned}
\tag{4.45}
$$

where

$$U_{pq}^{(N)} = \sum_{p=1}^{3} \Bigg\{ \kappa_{00}^{(N)} \frac{\sin \chi_{pq}}{|d_p|} + L_{pq} \left(2\mathrm{Re}(\kappa_{10}^{(N)} c_p) - \kappa_{11}^{(N)} |d_p| \right) + 2|d_p| \mathrm{Re} \left(\kappa_{20}^{(N)} c_p^2 \left[L_{pq} + 2iE_{pq} \right] \right) \Bigg\}$$

$$\begin{aligned} V_{pq}^{(N)} = \sum_{p=1}^{3} \Bigg\{ & \kappa_{00}^{(N)} \frac{c_p^2}{2|d_p|} \left[\sin \chi_{pq} - 2iE_{pq} \cos \chi_{pq} \right] \\ & - \kappa_{10}^{(N)} \frac{c_p^3}{8} \left[4L_{pq} + iE_{pq} \left(E_{pq}^2 + 8 \right) \right] \\ & + \kappa_{01}^{(N)} \frac{c_p}{8} \left[12L_{pq} + 5iE_{pq} \right] \\ & - \kappa_{20}^{(N)} \frac{|d_p| c_p^4}{2} \left[3L_{pq} - 2iE_{pq} \left(E_{pq}^2 - 3 \right) \right] \\ & - \kappa_{02}^{(N)} \frac{3|d_p|}{2} L_{pq} + \kappa_{11}^{(N)} \frac{3|d_p| c_p^2}{2} \left[L_{pq} + 2iE_{pq} \right] \Bigg\} \end{aligned} \tag{4.46}$$

4.4 Adaptation of the Method for Parallel Computing

The assembly of the matrix of the system of linear equations involves two nested cycles over the nodes and over the collocation points. Each node is associated with three consequent columns of the matrix, while each collocation point corresponds to three consequent rows. This double cycle hardly allows for parallelization; however, with some modifications to the algorithm, its most time-consuming procedures, i.e. integration over the elements, can be performed in parallel way. Thus, it is suggested that the main steps of the matrix assembly be as follows:

- Organization of the triangulation data. These must include the following:
  - The $3 \times N_{ver}$ matrix of coordinates of vertices of the mesh.
  - The connectivity $3 \times N_{ele}$ matrix ($N_{ele} = N_B + N_C$), each column of which contains the numbers of the vertices constituing the corresponding triangle.

- Mesh preprocessing.
  - First, the list of the edges is created (each entry contains the numbers of the beginning and the end points of the corresponding edge, the number of the elements containing this edge, and the list of these elements).
  - Next, the matrix of nodes' coordinates is created. The new nodes are introduced as explained in Subsection 4.2.2 and added to this matrix.
  - The connectivity matrix is updated to include the new nodes of each element.
  - The indicators - the integer numbers that identify the nodes' location (the crack surface, or crack tip, or crack mouth, etc.) - are assigned to the nodes.
  - The connectivity matrix is modified at each crack mouth to incorporate the corresponding coincident nodes as described in Subsection 4.2.4.
  - $N_{col} = N_{nod}$ collocation points are distributed on the mesh (see Subsection 4.2.2). At this stage, the prescribed load is assigned to each collocation point.
- In case of the continuous approximation scheme (**a**) of Subsection 4.2.2 being used, the "inverse" of the connectivity matrix is created, each column of which contains the number of elements sharing the corresponding node, the list of these elements, and the position (from 1 to 6) of the node within each of these elements.
  - If the discontinuous approximation scheme (**b**) is used, each node is associated with one particular element. Thus, the "inverse" connectivity matrix is not necessary.
- Local 3×3 rotation matrices are calculated for each element as described in Subsection 4.2.3. Each matrix is associated with only one element, therefore this procedure can be parallelized.

- Local influence matrices are calculated. Each of these matrices contains the contribution of all six nodes of a particular element to the traction at a particular collocation point (see Eqs.(4.22 – 4.29) and Subsection 4.3.4). Thus, each local matrix contains 3×18 elements. This procedure involves the use of the local rotation matrices and can also be performed in parallel way.

- The "global" matrix is assembled of the local influence matrices involving the **H** kernel. For every node, the influence of all elements that contain this node is summed up. At this stage, the "inverse" connectivity matrix is used.

- The right-hand side is assembled with the use of the local influence matrices involving the **T** kernel. Since every collocation point is associated with only one element, this procedure can also be parallelized.

It can be seen that such algorithm allows for saving computational time for the price of the memory allocated for the additional data arrays: the "inverse" connectivity matrix, N_{ele} local rotation matrices, and N_{ele} local influence matrices.

Chapter 5

Numerical Examples

5.1 A Penny-Shaped Crack

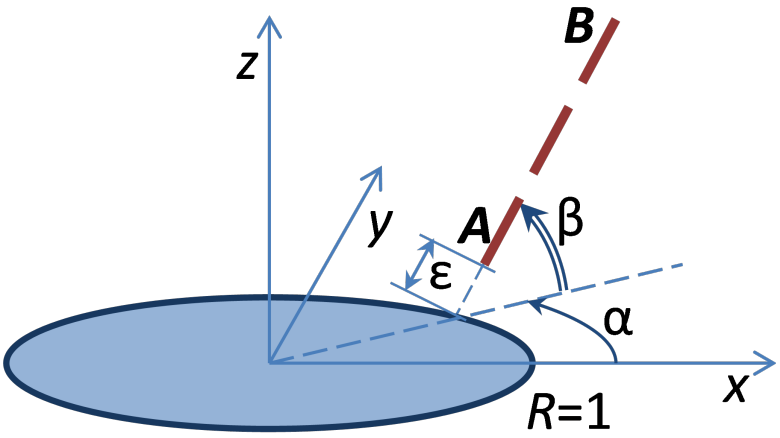

Figure 5.1: Penny-shaped crack. Location of points for evaluation of stresses near the crack tip.

The problem of a penny-shaped crack in an infinite domain under normal or shear load is well-known and well studied ([15],[74]-[79]). The analytical solutions for the displacement discontinuities and for the stresses around the crack have been briefly

summarized in the Appendix of [58] and are reproduced in Appendix D of this dissertation. In [58], the numerical solution of this problem with constant approximation of unknowns was also reported. Here, those results are compared with the new results obtained with the use of quadratic approximations.

The problem is governed by the following parameters: the radius of the crack R, Poisson's ratio ν, and the dimensionless far-field stress $S = \sigma^{\infty}_{jk}/\mu$. The following results are provided for $\nu = 0.25$, $R = 1$, and two cases of S: $S = \sigma^{\infty}_{zz}/\mu$ for normal loading and $S = \sigma^{\infty}_{xz}/\mu$ for shear loading.

Fig. 5.2 compares the dimensionless displacement discontinuities $\triangle u_k/RS$ along the crack surface obtained using the two quadratic approximation schemes: continuous (**a**, see Subsection 4.2.2) with 121 elements and discontinuous (**b**, see Subsection 4.2.2) with 40 elements. Different numbers of elements are chosen to keep roughly the same number of degrees of freedom (243 and 240 collocation points, respectively). The reference analytical solution is identified by the solid line. One can see that the scheme **a** provides better results for displacement discontinuities under both normal and shear loads. It can be due to the fact that in this scheme the zero DD conditions were enforced at vertices on the crack front.

Fig. 5.3 compares the results for the dimensionless displacement discontinuities (both for normal and shear loads) obtained using continuous quadratic approximation scheme (**a**) with 243 collocation points and constant approximation scheme with 258 collocation points. The reference analytical solution is again identified by the solid line. It could be seen that, for roughly the same numbers of degrees of freedom, continuous quadratic approximation scheme yields much better accuracy, especially in the crack tip region.

Fig. 5.4 demonstrates the mesh convergence of the method by comparing the results for the dimensionless displacement discontinuities (for both normal and shear loads) obtained on meshes with 121 and 1025 elements.

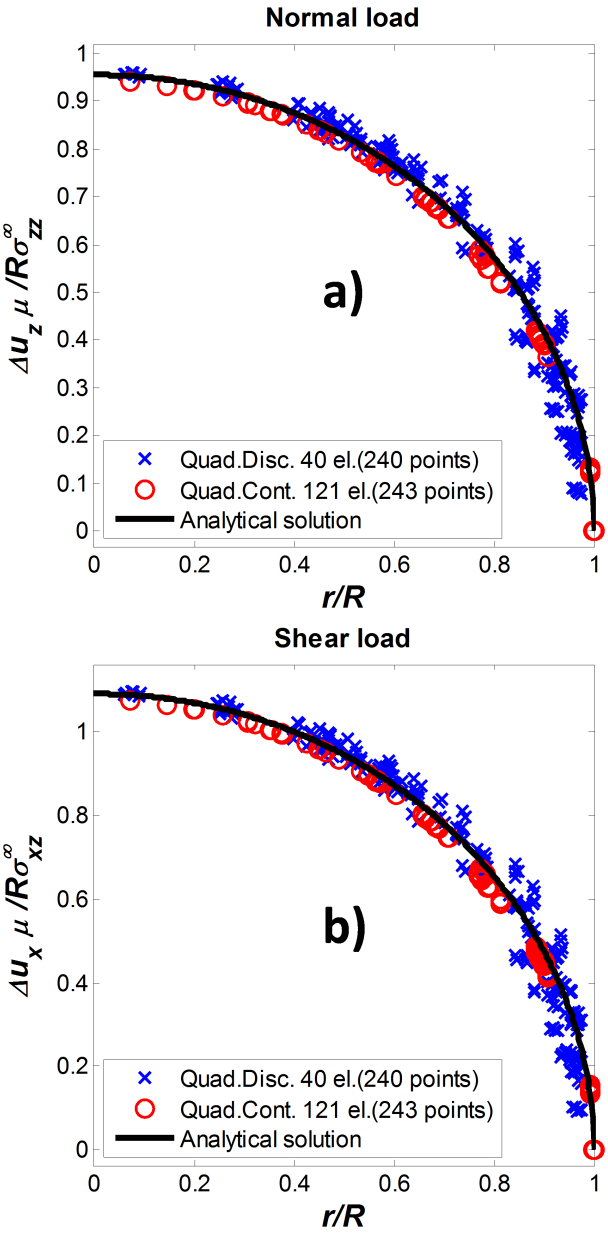

Figure 5.2: Normalized displacement discontinuity ($\triangle \mathbf{u}/RS$) on a penny-shaped crack. Continuous (scheme (**a**)) and discontinuous (scheme (**b**)) quadratic approximations. a) normal load with $S = \sigma^{\infty}_{zz}/\mu$; b) shear load with $S = \sigma^{\infty}_{xz}/\mu$.

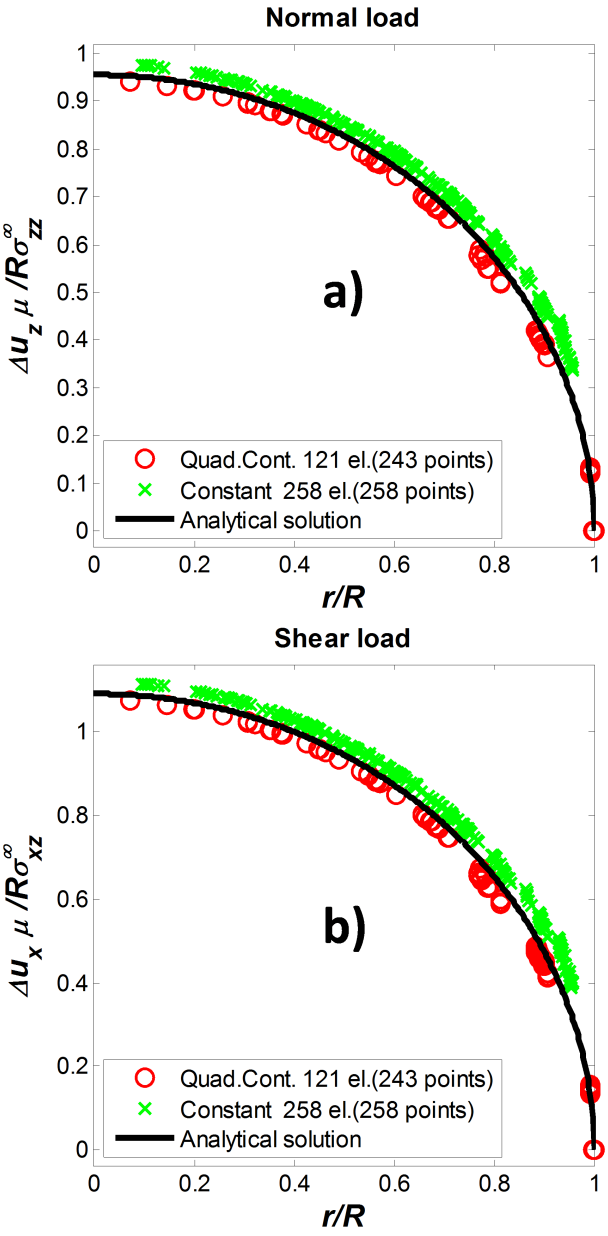

Figure 5.3: Normalized displacement discontinuity ($\triangle \mathbf{u}/RS$) on a penny-shaped crack. Continuous (scheme (**a**)) and constant approximations. a) normal load with $S = \sigma^{\infty}_{zz}/\mu$; b) shear load with $S = \sigma^{\infty}_{xz}/\mu$.

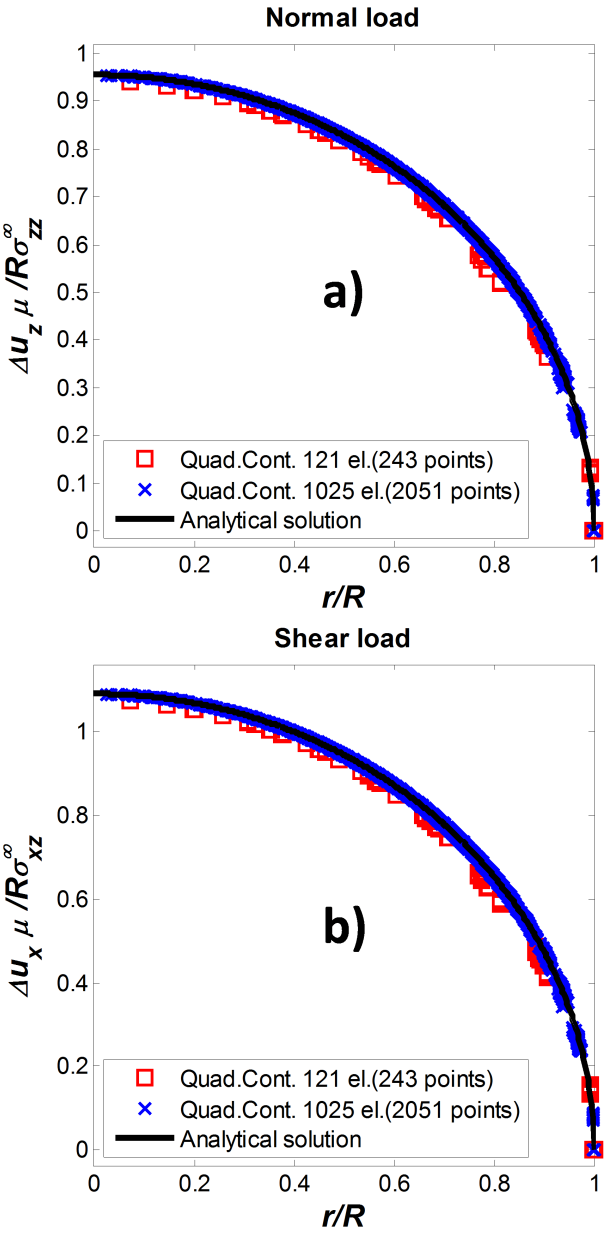

Figure 5.4: Normalized displacement discontinuity ($\triangle \mathbf{u}/RS$) on a penny-shaped crack. Quadratic approximations (scheme (**a**)) on meshes with 121 and 1025 elements. a) normal load with $S = \sigma^{\infty}_{zz}/\mu$; b) shear load with $S = \sigma^{\infty}_{xz}/\mu$.

The stresses near the crack tip were evaluated on the line AB shown in Fig. 5.1 using both quadratic schemes **a** and **b** and constant approximations. The results (dimensionless stresses $\sigma_{zz}/\sigma_{zz}^{\infty}$ for normal load and $\sigma_{jk}/\sigma_{xz}^{\infty}$ for shear load vs. dimensionless distance from the crack tip d/R) presented in Figs. 5.5 – 5.15 are calculated on the lines characterized by different angles α, β using quadratic and constant approximation schemes. The dimensionless stresses along the line with $\alpha = \beta = 45^o$ are also tabulated in Tables 5.1 and 5.2 along with the corresponding analytical solutions (see [15],[74]-[79]).

It could be seen from these figures and tables that both quadratic approximation schemes **a** and **b** somehow reflect the asymptotic behavior of stresses where constant approximations already fail to do. The accuracy of the tabulated solution, except for the region very close to the crack tip (less than 1/10 the size of an element), as well as near the points where the stresses are close to zero, is within 10% for quadratic approximations (121 elements) and up to 64% for constant approximations (258 elements). Note that no special crack tip shape functions were employed in the described method.

Table 5.1: Penny-shaped crack under normal ($S = \sigma_{zz}^{\infty}/\mu$) load. Dimensionless stresses ($\widetilde{\sigma}_{jk} = \sigma_{jk}/\mu S$) at points near the crack tip (line AB with $\alpha = \beta = 45^o$ in Fig. 5.1).

Analytical solution						
d	x=y	z	$\widetilde{\sigma}_{xx} = \widetilde{\sigma}_{yy}$	$\widetilde{\sigma}_{xy}$	$\widetilde{\sigma}_{xz} = \widetilde{\sigma}_{yz}$	$\widetilde{\sigma}_{zz}$
0.005	0.7096	0.0035	2.6699	0.4135	0.5989	8.0034
0.205	0.8096	0.1450	0.0636	-0.0074	0.0451	1.5024
0.405	0.9096	0.2864	0.0012	-0.0266	0.0123	1.2344
0.605	1.0096	0.4278	-0.0111	-0.0281	0.0008	1.1360
0.805	1.1096	0.5692	-0.0130	-0.0253	-0.0039	1.0873
1.005	1.2096	0.7106	-0.0122	-0.0218	-0.0056	1.0595

Constant approximations (258 elements)								
d	x=y	z	$\widetilde{\sigma}_{xx}$	$\widetilde{\sigma}_{yy}$	$\widetilde{\sigma}_{xy}$	$\widetilde{\sigma}_{xz}$	$\widetilde{\sigma}_{yz}$	$\widetilde{\sigma}_{zz}$
0.005	0.7096	0.0035	3.4939	3.5542	-2.5778	0.3943	0.3863	26.2161
0.205	0.8096	0.1450	0.0411	0.0453	-0.0379	0.0226	0.0228	1.5868
0.405	0.9096	0.2864	-0.0063	-0.0043	-0.0364	0.0044	0.0051	1.2584
0.605	1.0096	0.4278	-0.0147	-0.0141	-0.0331	-0.0031	-0.0028	1.1473
0.805	1.1096	0.5692	-0.0152	-0.0150	-0.0285	-0.0061	-0.0060	1.0938
1.005	1.2096	0.7106	-0.0137	-0.0136	-0.0240	-0.0072	-0.0071	1.0637

Quadratic approximations (121 elements)								
d	x=y	z	$\widetilde{\sigma}_{xx}$	$\widetilde{\sigma}_{yy}$	$\widetilde{\sigma}_{xy}$	$\widetilde{\sigma}_{xz}$	$\widetilde{\sigma}_{yz}$	$\widetilde{\sigma}_{zz}$
0.005	0.7096	0.0035	2.6828	2.9155	0.8992	0.6430	0.6706	6.1098
0.205	0.8096	0.1450	0.0660	0.0646	-0.0100	0.0493	0.0488	1.5292
0.405	0.9096	0.2864	0.0001	-0.0000	-0.0291	0.0120	0.0121	1.2449
0.605	1.0096	0.4278	-0.0121	-0.0122	-0.0298	0.0002	0.0002	1.1413
0.805	1.1096	0.5692	-0.0138	-0.0138	-0.0266	-0.0044	-0.0044	1.0904
1.005	1.2096	0.7106	-0.0127	-0.0128	-0.0227	-0.0061	-0.0061	1.0616

Table 5.2: Penny-shaped crack under shear ($S = \sigma_{xz}^{\infty}/\mu$) load. Dimensionless stresses ($\widetilde{\sigma}_{jk} = \sigma_{jk}/\mu S$) at points near the crack tip (line AB with $\alpha = \beta = 45^o$ in Fig. 5.1).

Analytical solution					
d	x=y	z	$\widetilde{\sigma}_{xy}$	$\widetilde{\sigma}_{xz}$	$\widetilde{\sigma}_{yz}$
0.005	0.7096	0.0035	-1.8236	4.7566	-0.3589
0.205	0.8096	0.1450	-0.2570	1.1087	-0.0959
0.405	0.9096	0.2864	-0.1530	1.0149	-0.0742
0.605	1.0096	0.4278	-0.1022	0.9938	-0.0582
0.805	1.1096	0.5692	-0.0720	0.9886	-0.0459
1.005	1.2096	0.7106	-0.0525	0.9881	-0.0366
Constant approximations (258 elements)					
d	x=y	z	$\widetilde{\sigma}_{xy}$	$\widetilde{\sigma}_{xz}$	$\widetilde{\sigma}_{yz}$
0.005	0.7096	0.0035	-9.2875	6.8749	-5.6704
0.205	0.8096	0.1450	-0.2958	1.0851	-0.1389
0.405	0.9096	0.2864	-0.1672	1.0069	-0.0885
0.605	1.0096	0.4278	-0.1100	0.9899	-0.0657
0.805	1.1096	0.5692	-0.0771	0.9863	-0.0507
1.005	1.2096	0.7106	-0.0561	0.9865	-0.0399
Quadratic approximations (121 elements)					
d	x=y	z	$\widetilde{\sigma}_{xy}$	$\widetilde{\sigma}_{xz}$	$\widetilde{\sigma}_{yz}$
0.005	0.7096	0.0035	-1.1884	4.7212	0.2779
0.205	0.8096	0.1450	-0.2670	1.1147	-0.1019
0.405	0.9096	0.2864	-0.1581	1.0147	-0.0779
0.605	1.0096	0.4278	-0.1054	0.9932	-0.0606
0.805	1.1096	0.5692	-0.0742	0.9880	-0.0476
1.005	1.2096	0.7106	-0.0541	0.9876	-0.0378

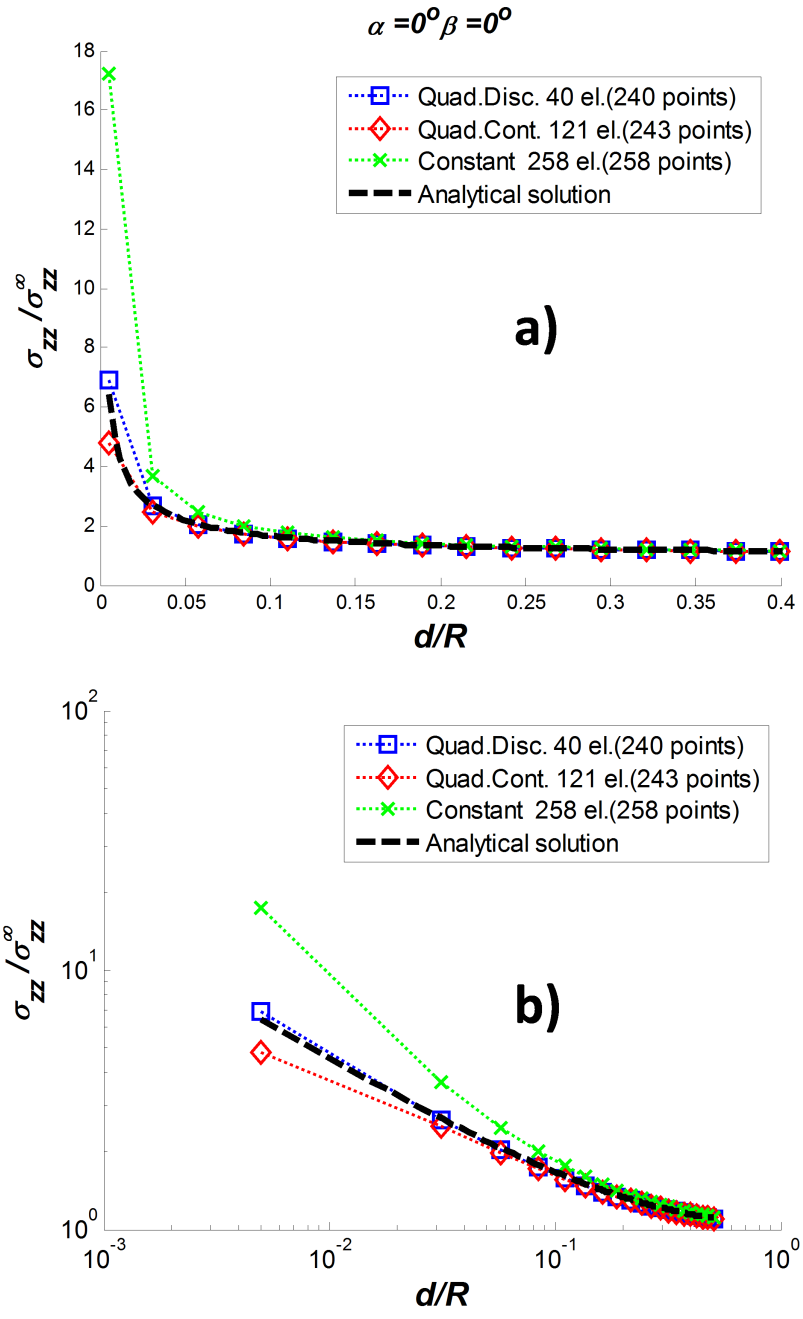

Figure 5.5: Dimensionless normal stress ($\sigma_{zz}/\sigma_{zz}^{\infty}$) near the tip of a penny shape crack under normal load. $\alpha = 0, \beta = 0$. **a**) linear scale; **b**) log-log scale.

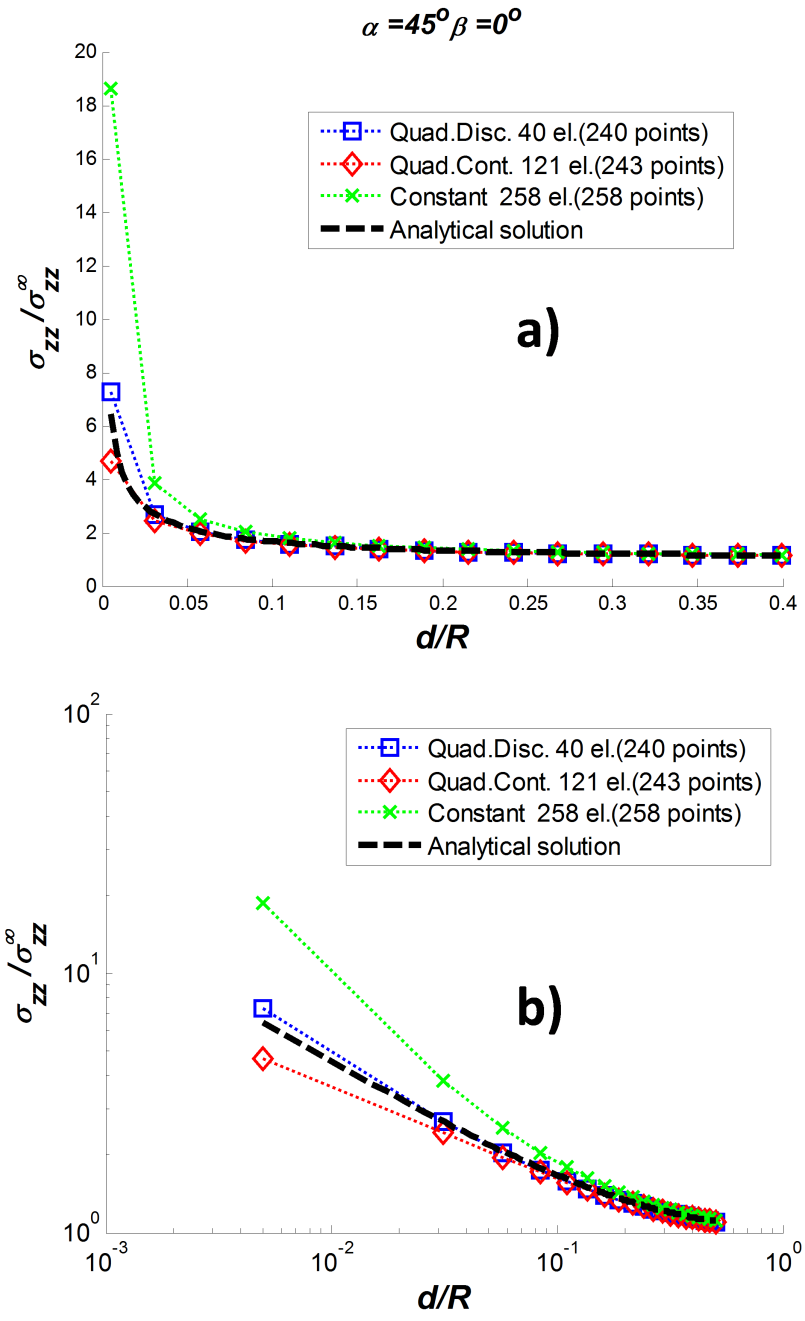

Figure 5.6: Dimensionless normal stress ($\sigma_{zz}/\sigma_{zz}^{\infty}$) near the tip of a penny shape crack under normal load. $\alpha = 45^o, \beta = 0$. **a**) linear scale; **b**) log-log scale.

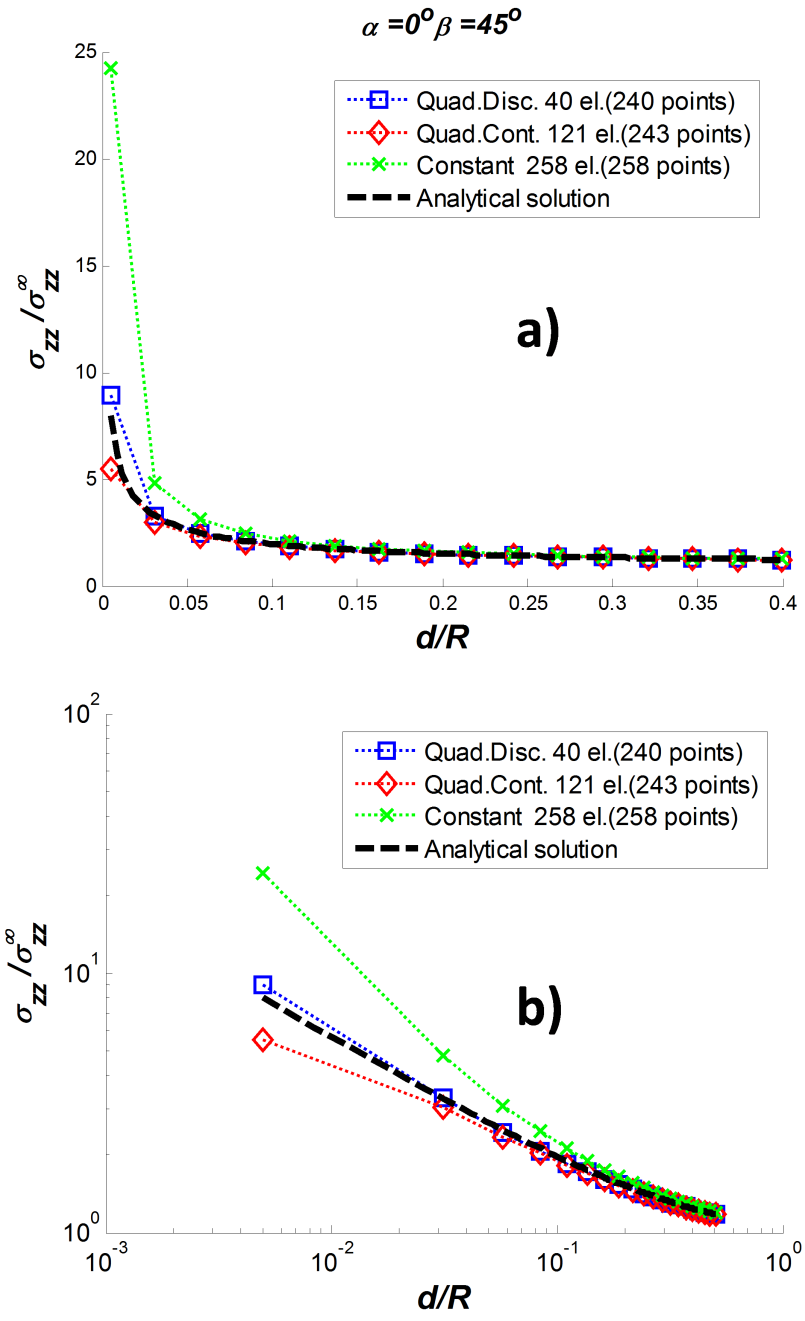

Figure 5.7: Dimensionless normal stress ($\sigma_{zz}/\sigma_{zz}^{\infty}$) near the tip of a penny shape crack under normal load. $\alpha = 0, \beta = 45^o$. **a**) linear scale; **b**) log-log scale.

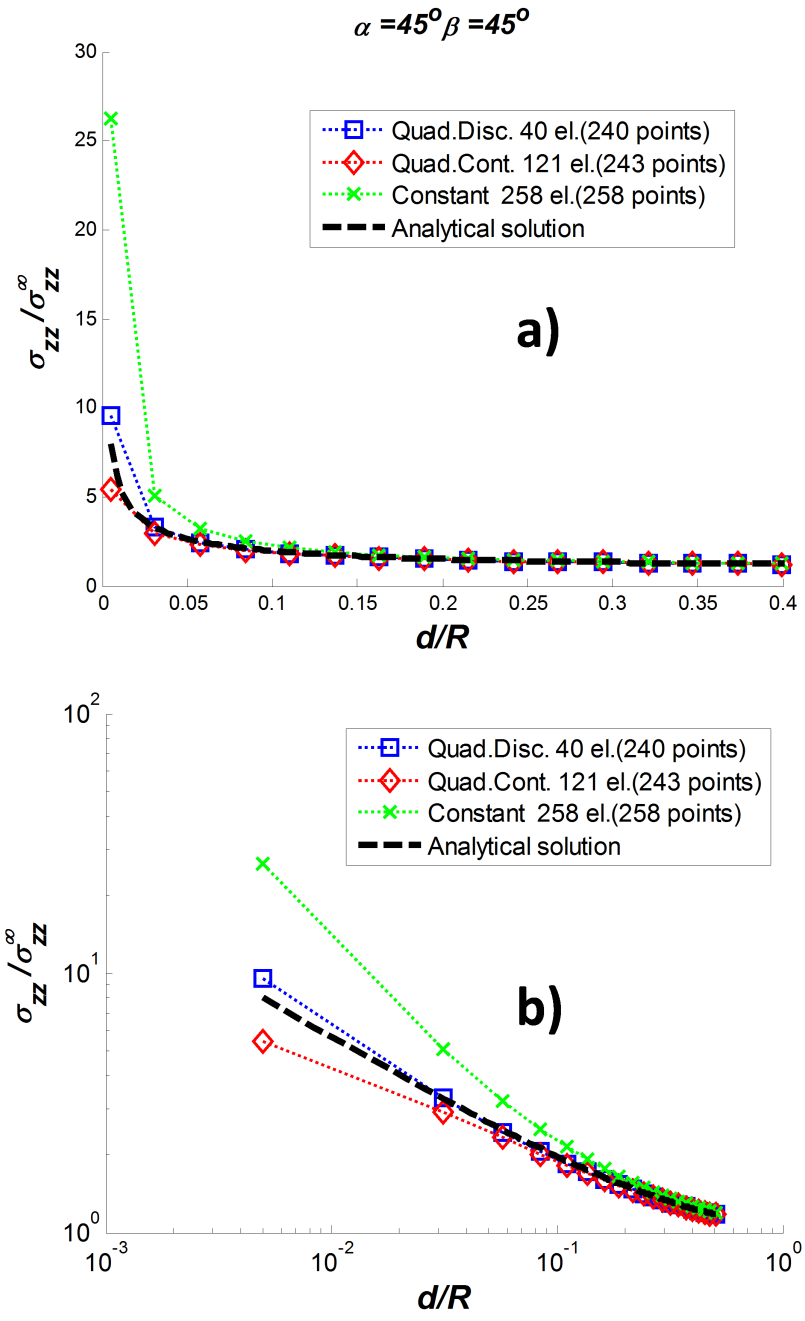

Figure 5.8: Dimensionless normal stress ($\sigma_{zz}/\sigma_{zz}^{\infty}$) near the tip of a penny shape crack under normal load. $\alpha = 45^o, \beta = 45^o$. **a**) linear scale; **b**) log-log scale.

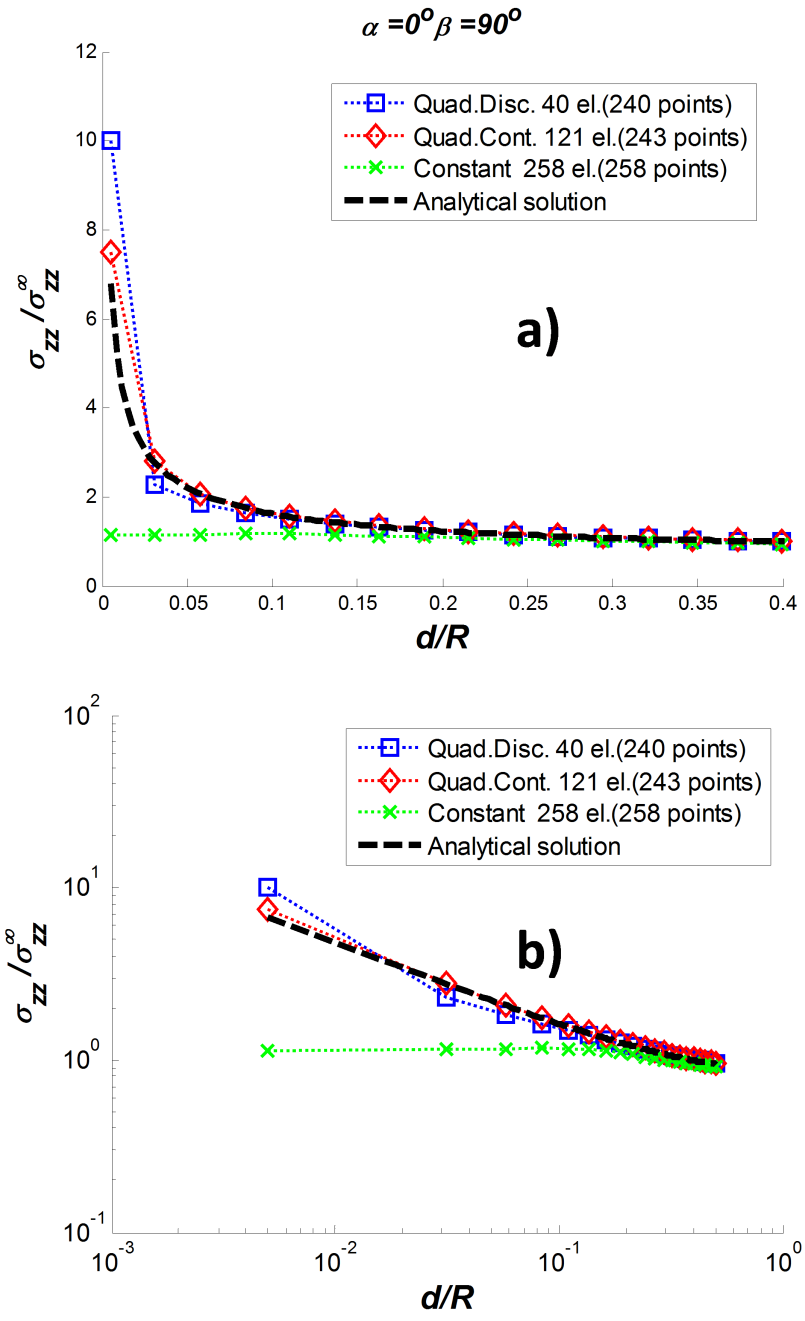

Figure 5.9: Dimensionless normal stress ($\sigma_{zz}/\sigma_{zz}^{\infty}$) near the tip of a penny shape crack under normal load. $\alpha = 0, \beta = 90^o$. **a**) linear scale; **b**) log-log scale.

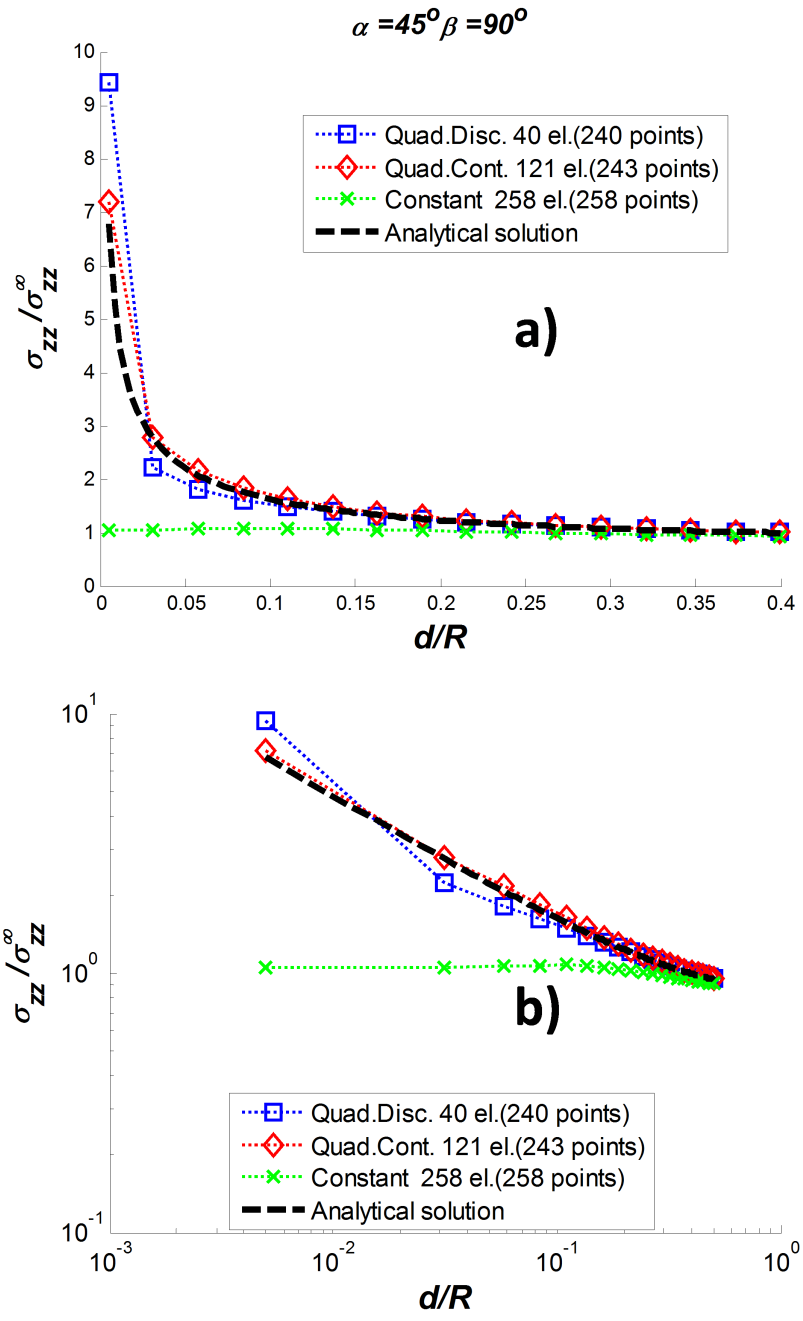

Figure 5.10: Dimensionless normal stress ($\sigma_{zz}/\sigma_{zz}^{\infty}$) near the tip of a penny shape crack under normal load. $\alpha = 45^o, \beta = 90^o$. **a**) linear scale; **b**) log-log scale.

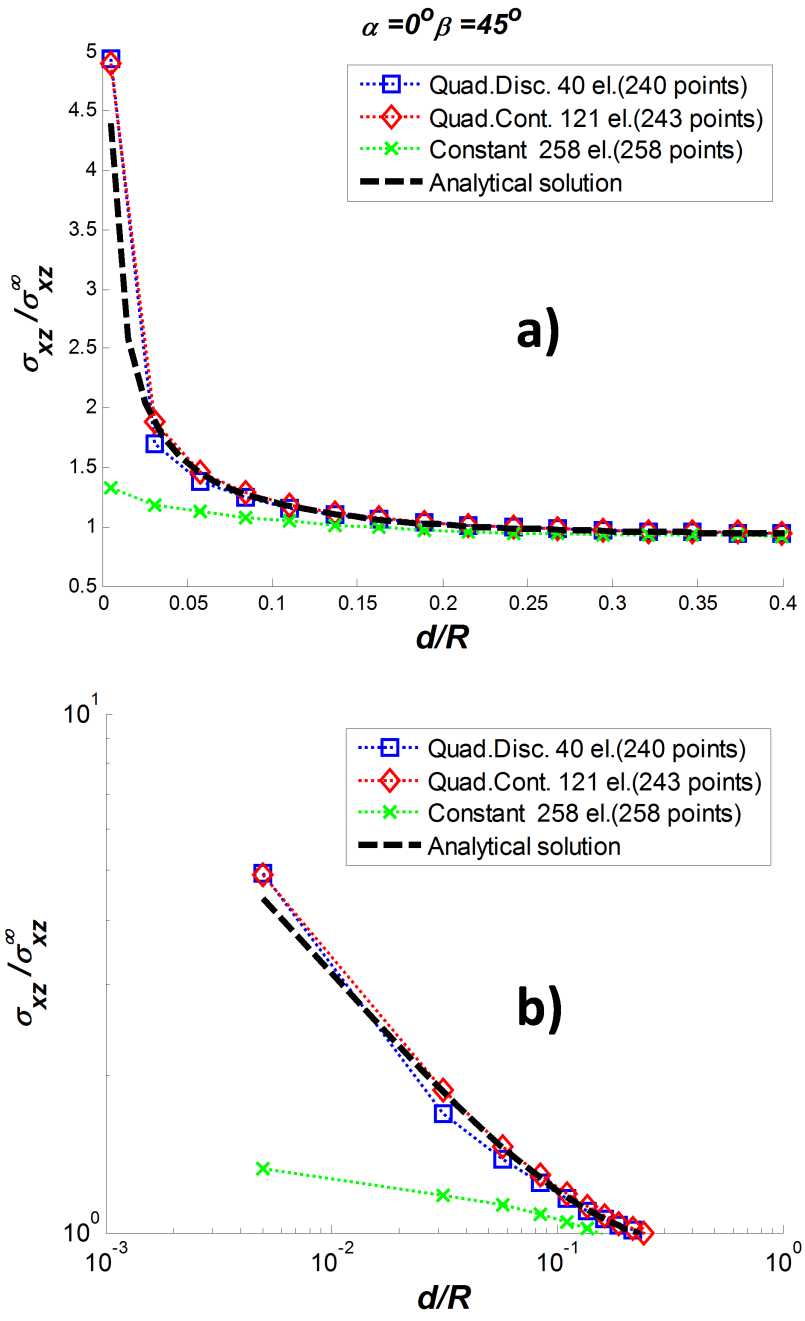

Figure 5.11: Dimensionless shear stresses ($\sigma_{xz}/\sigma_{xz}^{\infty}$) near the tip of a penny shape crack under shear load. $\alpha = 0, \beta = 45^o$. **a**) linear scale; **b**) log-log scale.

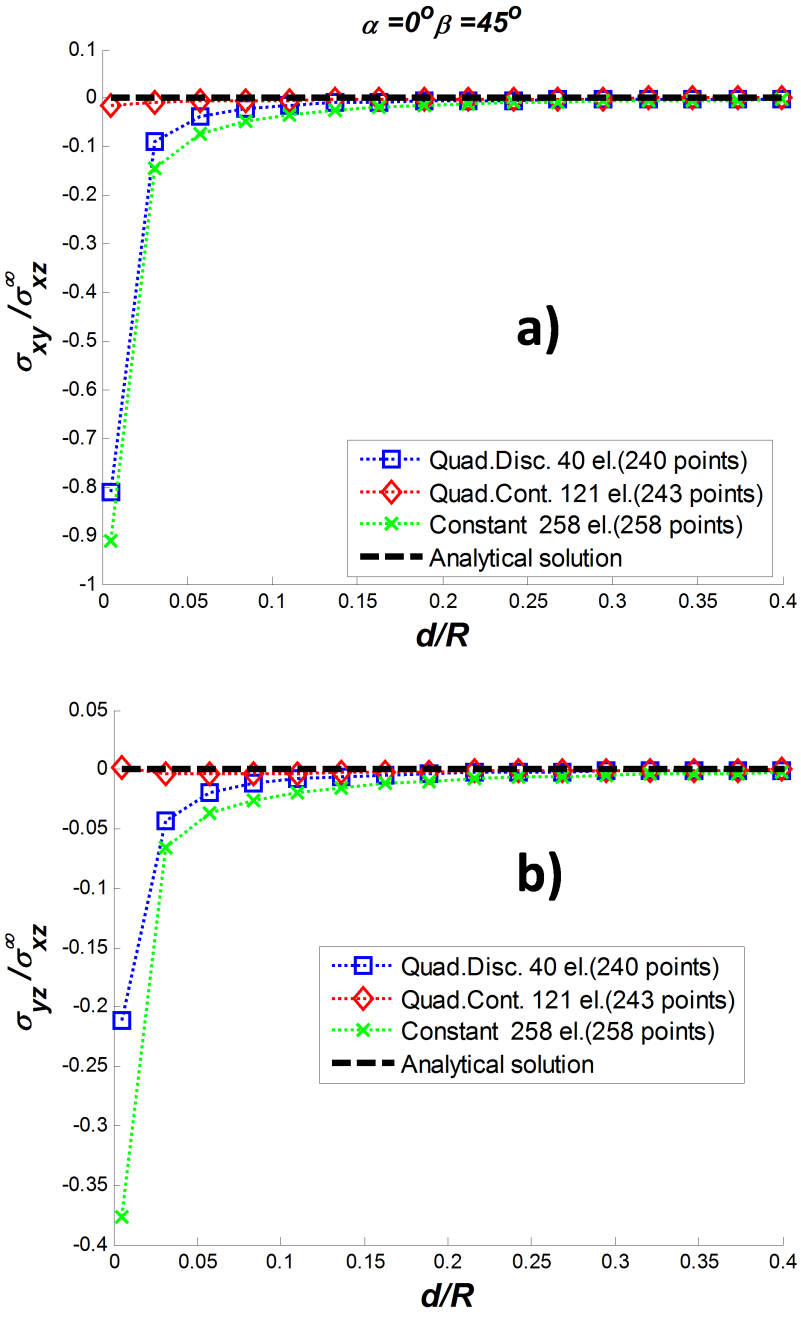

Figure 5.12: Dimensionless shear stresses $(\sigma_{xy}/\sigma^{\infty}_{xz}, \sigma_{yz}/\sigma^{\infty}_{xz})$ near the tip of a penny shape crack under shear load. $\alpha = 0, \beta = 45^o$. **a**) $\sigma_{xy}/\sigma^{\infty}_{xz}$; **b**) $\sigma_{yz}/\sigma^{\infty}_{xz}$.

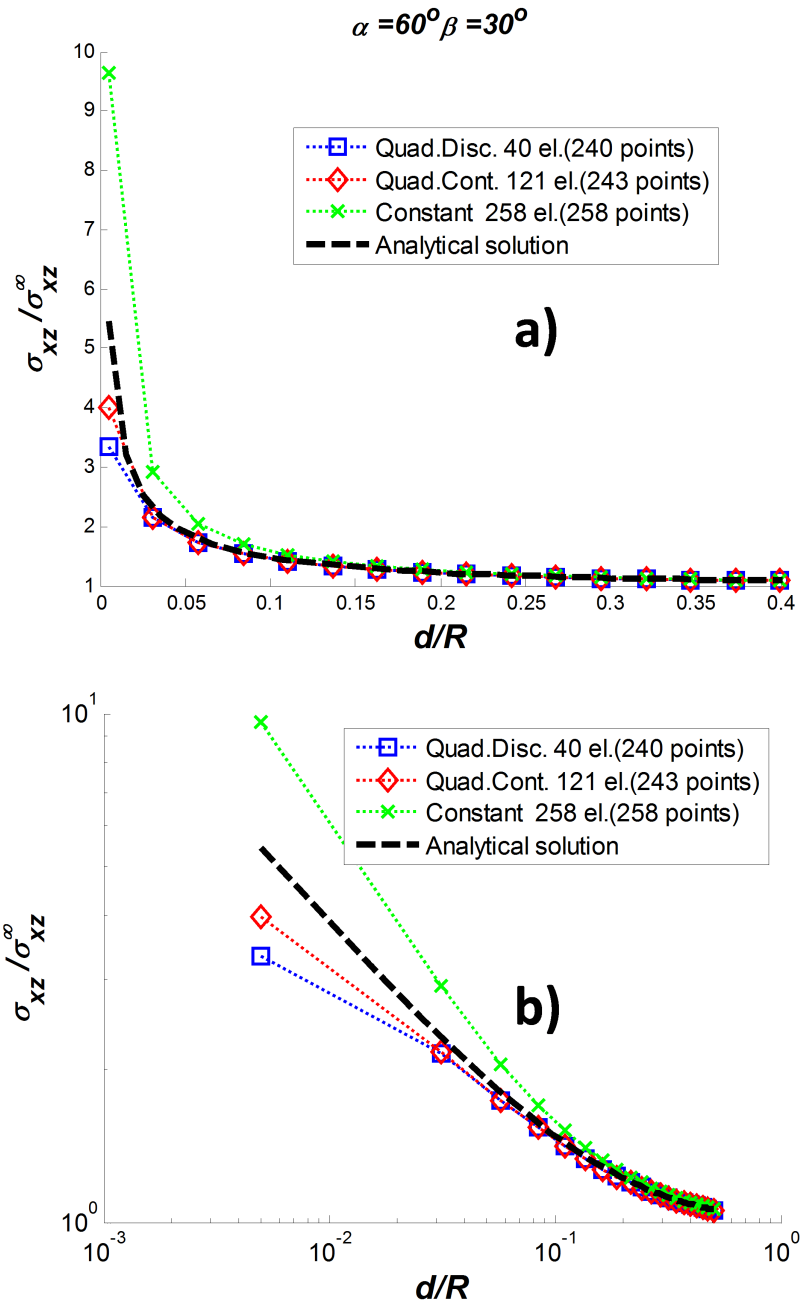

Figure 5.13: Dimensionless shear stresses ($\sigma_{xz}/\sigma^{\infty}_{xz}$) near the tip of a penny shape crack under shear load. $\alpha = 60^o, \beta = 30^o$. **a**) linear scale; **b**) log-log scale.

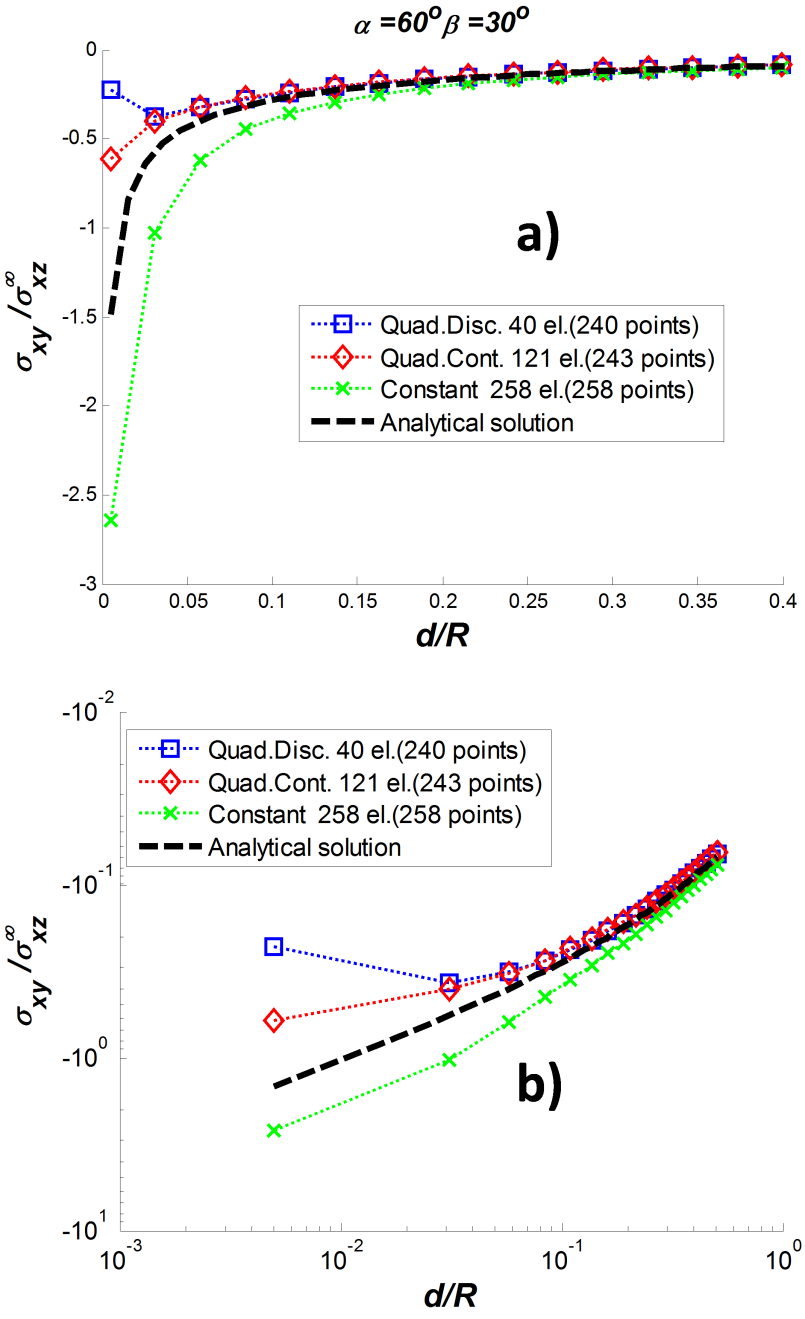

Figure 5.14: Dimensionless shear stresses ($\sigma_{xy}/\sigma_{xz}^{\infty}$) near the tip of a penny shape crack under shear load. $\alpha = 60^o, \beta = 30^o$. **a**) linear scale; **b**) log-log scale.

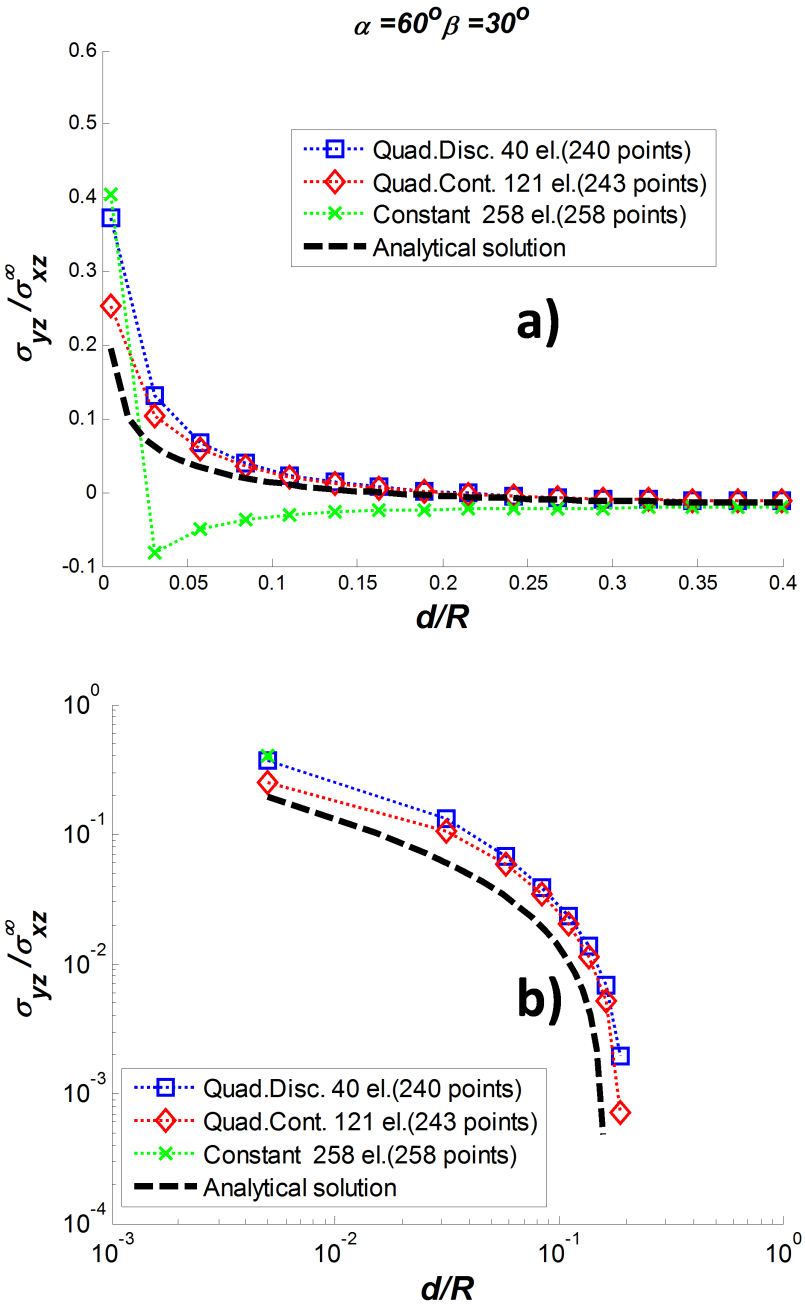

Figure 5.15: Dimensionless shear stresses ($\sigma_{yz}/\sigma_{xz}^{\infty}$) near the tip of a penny shape crack under shear load. $\alpha = 60^o, \beta = 30^o$. **a**) linear scale; **b**) log-log scale.

The two following benchmark problems were solved with the use of constant approximation of unknowns. The results are reproduced as reported in [58].

5.2 Two Non-Parallel Penny-Shaped Cracks

Consider two penny-shaped cracks shown in Fig. 5.16. The first crack is located in the plane $z = 0$ and centered at the origin of the coordinate system, while the second crack of the same radius R is centered at the point $(R,\, 0,\, R)$ and rotated 30^o around the y axis and 15^o around the x axis.

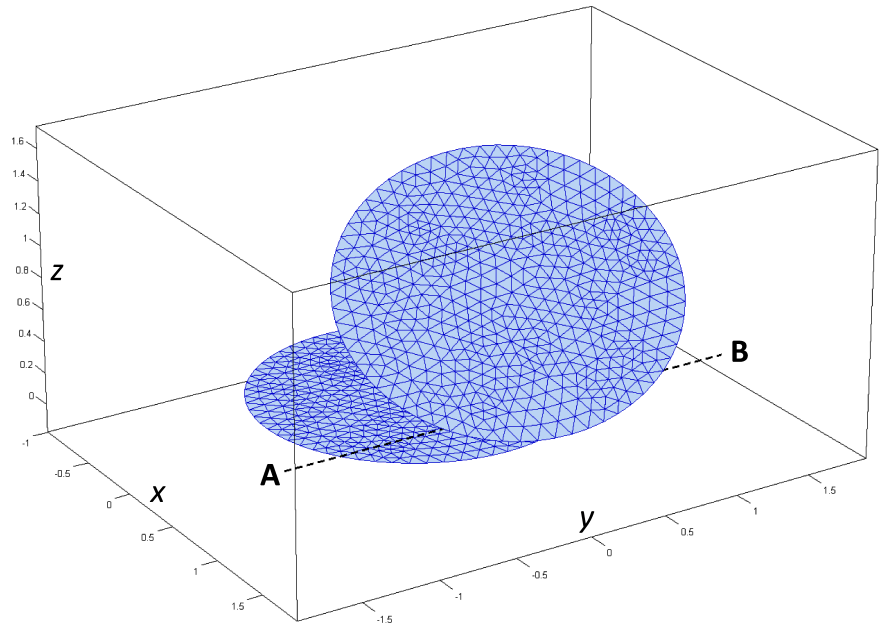

Figure 5.16: Two non-parallel cracks. The boundary mesh and the location of points for evaluation of stresses.

A mesh of 1032 elements was used for each crack. $R = 1$ and $\nu = 0.25$ were assumed in the calculations. Uniaxial far-field tension in z-direction was applied, $S = \sigma^{\infty}_{zz}/\mu$.

The results for stress components along the line connecting the points $\mathbf{A}\,(R,\, -1.5R,\, 0.25R)$ and $\mathbf{B}\,(R,\, 1.5R,\, 0.25R)$ (see Fig. 5.16) are shown on Fig. 5.17; the stresses at selected

points on this line are tabulated in the Table 5.3. The stresses along the line **AB** due to a single crack (the first one) are also plotted on the corresponding figures. As expected, the crack interaction plays a significant role on all stress components along the whole interval **AB**; the closer located areas are most affected. The example may serve as a benchmark solution, due to the lack of tabulated results for multiple crack problems.

Table 5.3: Two non-parallel cracks. Normalized stresses ($\sigma_{ij}/\sigma_{zz}^{\infty}$) at selected points along the line **AB** ($x/R = 1$, $z/R = 0.25$) for $\nu = 0.25$.

y/R	σ_{xx}	σ_{xy}	σ_{yy}	σ_{xz}	σ_{yz}	σ_{zz}
-1.5	0.021	0.018	-0.006	0.025	-0.016	1.12
-1.2	0.042	-0.042	-0.013	0.053	-0.103	1.18
-1.02	0.049	-0.07	-0.036	0.056	-0.22	1.12
-0.48	-0.14	-0.010	0.024	-0.22	-0.050	0.80
0	-0.16	-0.03	0.025	-0.41	0.05	0.69
0.36	-0.135	-0.032	0.0074	-0.29	0.072	0.91
0.96	0.041	-0.055	0.053	0.0047	0.17	1.066
1.5	0.028	-0.028	0.025	0.016	0.057	1.076

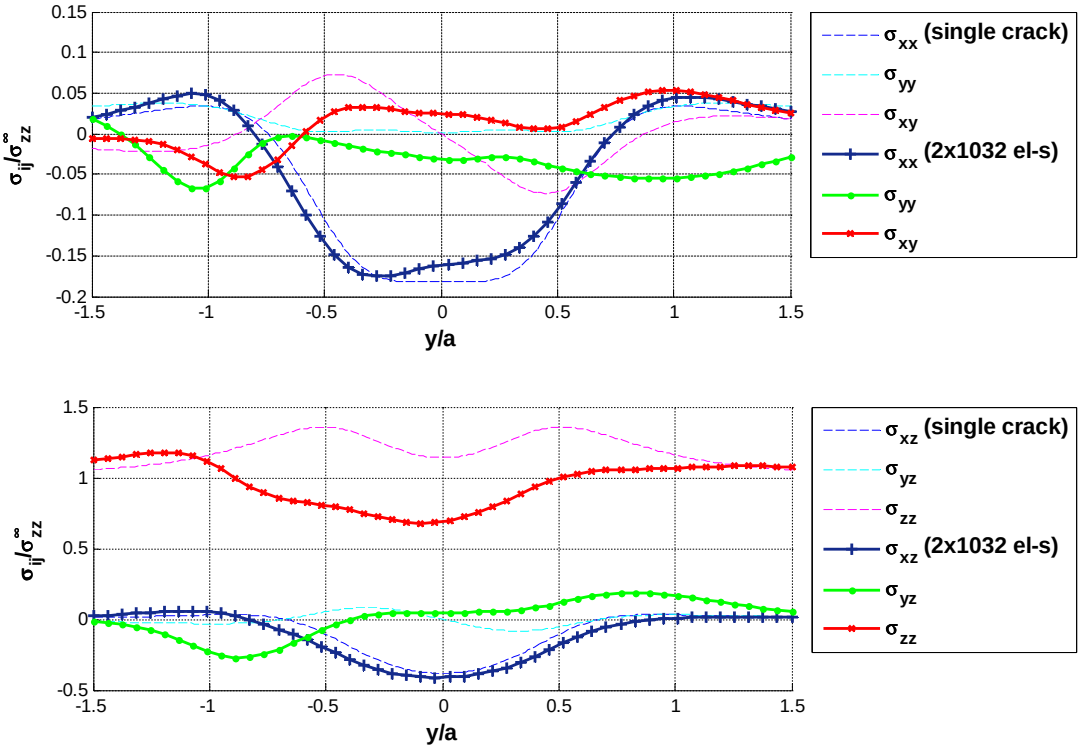

Figure 5.17: Two non-parallel penny-shaped cracks. Normalized stresses ($\sigma_{jk}/\sigma_{zz}^{\infty}$) along the line **AB** on Fig. 5.16.

5.3 A Semi-Cylindrical Crack under Biaxial Far-Field Tension

Consider a long semi-cylindrical crack of radius $R = 1$ and length $L = 10$ loaded in the directions perpendicular to the axis of the cylinder with $S = \sigma_{xx}^{\infty}/\mu = \sigma_{zz}^{\infty}/\mu$ (see Fig. 5.18). In the middle cross-section, the two-dimensional plane strain problem of a semi-circular crack in an infinite medium under biaxial tension at infinity can represent an approximate solution of such three-dimensional problem. The analytical solution for the plane strain problem can be found in [56].

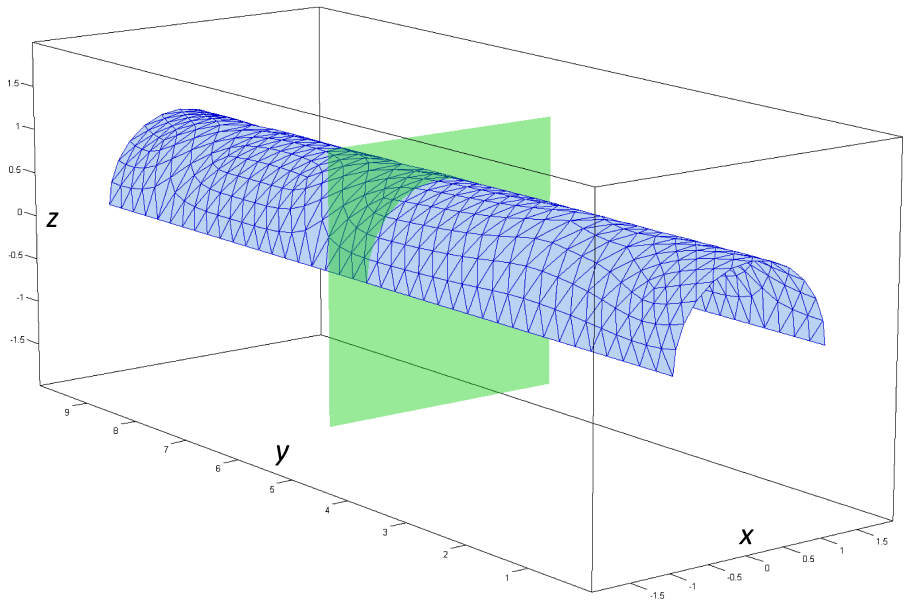

Figure 5.18: Semi-cylindrical crack under biaxial tension. The boundary mesh.

Fig. 5.18 shows the mesh of 1072 elements used in the three-dimensional simulation performed with the present approach as well as the calculated displacement discontinuity vectors at the collocation points. Poisson ratio $\nu = 0.3$ was assumed in the calculations.

Fig. 5.19 shows the stress field (normalized stress components along different straight lines) in the middle cross-section of the cylinder ($y = 0.5L$) compared to the plane strain solution. The results for the maximum relative errors $\delta\sigma_{ij}^{max} = \max\left|\sigma_{ij} - \sigma_{ij}^{2D}\right| / \sigma_{ij}^{2D}$ (σ_{ij}^{2D} are the stress components of the plane strain solution) on the selected lines are presented in Table 5.4. Taking into account that the reference problem is an approximation of the original three-dimensional one, the agreement between the results for all stress components is quite satisfactory.

Table 5.4: Semi-cylindrical crack. Relative errors for the stresses in the central cross-section.

z/R	$\delta\sigma_{xx}^{max}$, %	$\delta\sigma_{xz}^{max}$, %	$\delta\sigma_{zz}^{max}$, %
-2.0	0.76	4.51	8.96
-1.0	1.15	12.7	9.17
-0.5	4.00	24.1	18.3
2.0	0.74	3.17	8.52

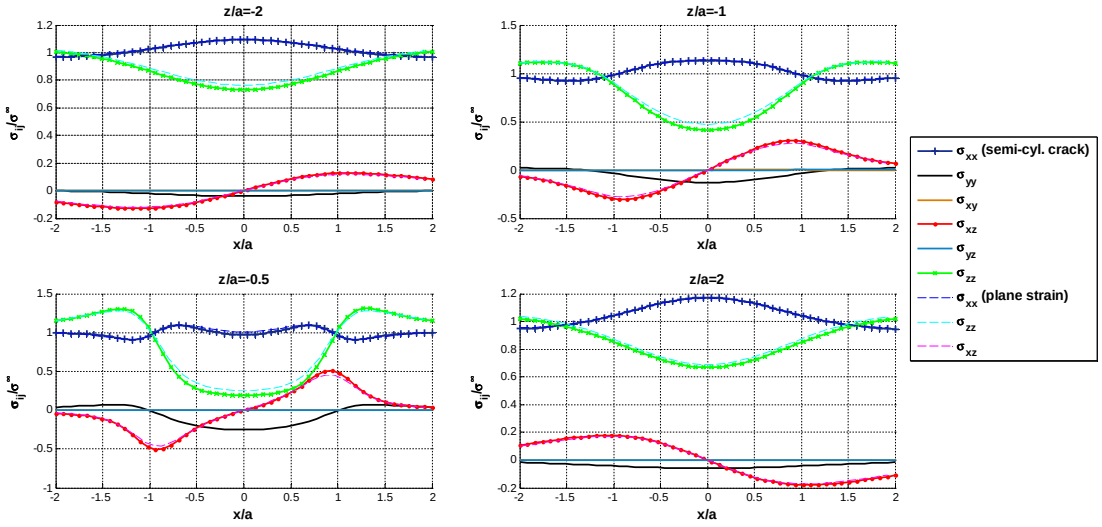

Figure 5.19: Normalized stresses (σ_{ij}/S, $S = \sigma_{xx}^{\infty} = \sigma_{zz}^{\infty}$) in the central cross-section of a semi-cylindrical crack under biaxial tension.

In the next examples, the results for quadratic approximations used continuous approximation scheme (**a**, see Subsection 4.2.2).

5.4 Two Coaxial Cylindrical Cracks

Consider two coaxial cracks of cylindrical shape of the same radius (Fig. 5.20) under biaxial far-field tension perpendicular to the axis. Assume that the length in the axial direction is much longer than the curvature radius. Thus, it is reasonable to expect that the fields in the middle cross-section of such system would mimic the solution of a 2D problem of two cracks along the same circle (Fig. 5.21). The corresponding 2D problem can be solved analytically [56] or numerically [51].

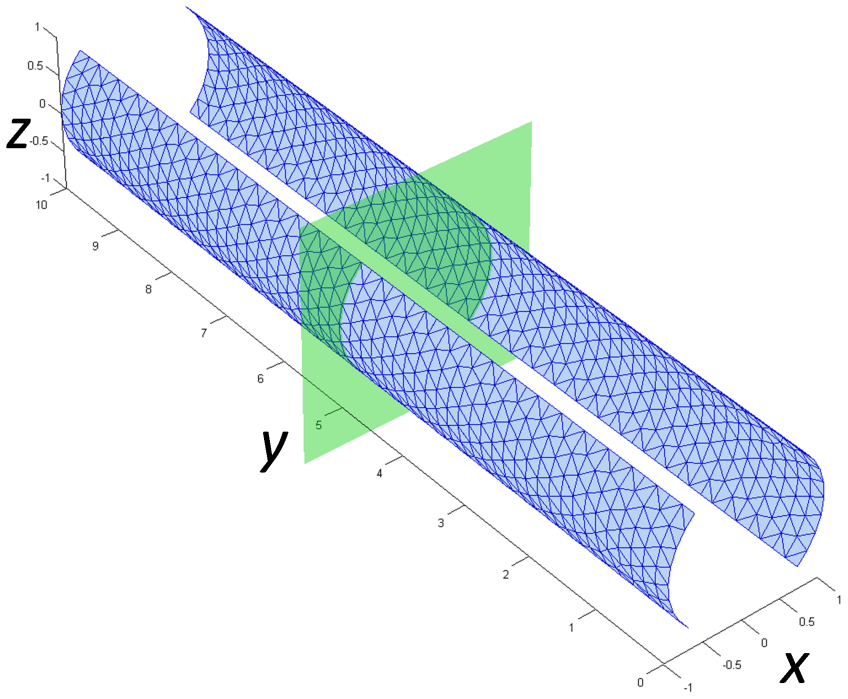

Figure 5.20: Two coaxial cylindrical cracks under biaxial tension. Mesh with 1604 elements.

The three-dimensional problem was solved for the following parameters: curvature radius $R = 1$, aspect ratio (length vs. curvature radius) $L/R = 10$, aperture angle $\vartheta = 45^o$. The dimensionless far-field stresses are set as follows: $S = \sigma_{xx}^{\infty}/\mu = \sigma_{zz}^{\infty}/\mu$. The results (dimensionless stress components in $x - z$ plane) are calculated on two straight lines in the central cross section starting at one of the crack tips (lines AB and CD shown in Fig. 5.21). d is the distance from the crack tip.

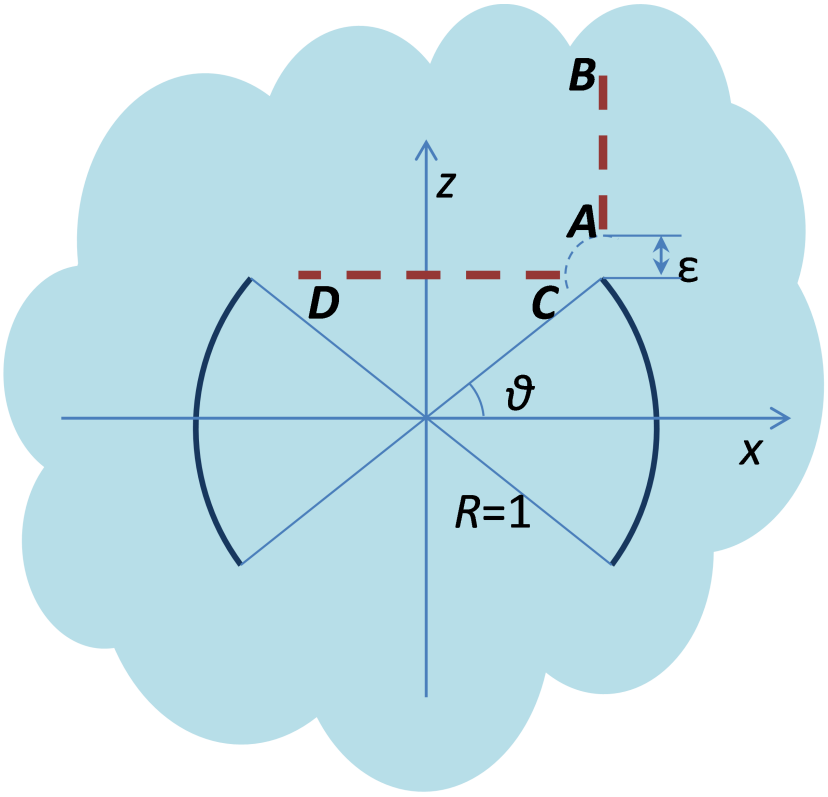

Figure 5.21: The central cross section of two coaxial cylindrical cracks. Location of points for evaluation of stresses near a crack tip.

Figs. 5.22 – 5.27 compare the three-dimensional results calculated using quadratic and constant approximations to the two-dimensional results obtained using the algorithm described in [51] with circular elements. Note that this algorithm employed special square root crack tip elements while the three-dimensional algorithm did not.

Table 5.5 presents the dimensionless stresses calculated at some points near one of the crack tips (on the lines AB and CD in Fig. 5.21). Table 5.6 presents the dimensionless stresses on the axial line of the cylinder ($x = z = 0$). The latter stresses are also plotted in Fig. 5.28 ($\sigma_{xz}/\mu S$ is not shown as it was equal to zero within the 0.005 accuracy).

The graphic and tabulated results confirm that the two-dimensional plane strain model provides reasonable estimates of the stresses in the middle cross-section.

Table 5.5: Two cylindrical cracks under biaxial tension ($S = \sigma^{\infty}_{xx}/\mu = \sigma^{\infty}_{zz}/\mu$). Dimensionless stresses ($\widetilde{\sigma}_{jk} = \sigma_{jk}/\mu S$) in the central cross-section near the crack tip (on the lines AB and CD in Fig. 5.21).

d	x	z	2D solution			3D BEM solution		
			$\widetilde{\sigma}_{xx}$	$\widetilde{\sigma}_{zz}$	$\widetilde{\sigma}_{xz}$	$\widetilde{\sigma}_{xx}$	$\widetilde{\sigma}_{zz}$	$\widetilde{\sigma}_{xz}$
0.005	0.7071	0.7121	6.8466	5.8725	0.5510	6.4854	5.5940	0.8229
0.105	0.7071	0.8121	1.7864	1.6298	-0.0338	1.7166	1.5902	-0.0391
0.205	0.7071	0.9121	1.4436	1.3356	-0.0676	1.4044	1.3150	-0.0667
0.305	0.7071	1.0121	1.3118	1.2127	-0.0751	1.2834	1.1997	-0.0727
0.405	0.7071	1.1121	1.2449	1.1444	-0.0739	1.2216	1.1353	-0.0709
0.505	0.7071	1.2121	1.2057	1.1015	-0.0687	1.1853	1.0948	-0.0656
0.005	0.7021	0.7071	6.7404	2.6827	2.7857	5.4604	2.8641	2.9524
0.105	0.6021	0.7071	1.6536	0.9347	0.5080	1.6320	0.9310	0.4496
0.205	0.5021	0.7071	1.2620	0.8593	0.3281	1.2567	0.8590	0.2982
0.305	0.4021	0.7071	1.0927	0.8481	0.2356	1.0922	0.8489	0.2174
0.405	0.3021	0.7071	0.9992	0.8524	0.1677	1.0001	0.8536	0.1563
0.505	0.2021	0.7071	0.9445	0.8598	0.1091	0.9459	0.8612	0.1023

Table 5.6: Dimensionless stresses ($\widetilde{\sigma}_{jk} = \sigma_{jk}/\mu S$) on the axis of two cylindrical cracks under biaxial tension ($S = \sigma^{\infty}_{xx}/\mu = \sigma^{\infty}_{zz}/\mu$).

y	$\widetilde{\sigma}_{xx}$	$\widetilde{\sigma}_{yy}$	$\widetilde{\sigma}_{zz}$
2D	0.0000	-	1.1458
5.0	0.0275	-0.2120	1.1439
6.0	0.0275	-0.2106	1.1433
7.0	0.0272	-0.2067	1.1413
8.0	0.0227	-0.1921	1.1348
9.0	0.0378	-0.1103	1.1078
10.0	0.7162	-0.1309	1.0627
11.0	1.0582	-0.0480	1.0202
12.0	1.0224	0.0031	1.0047

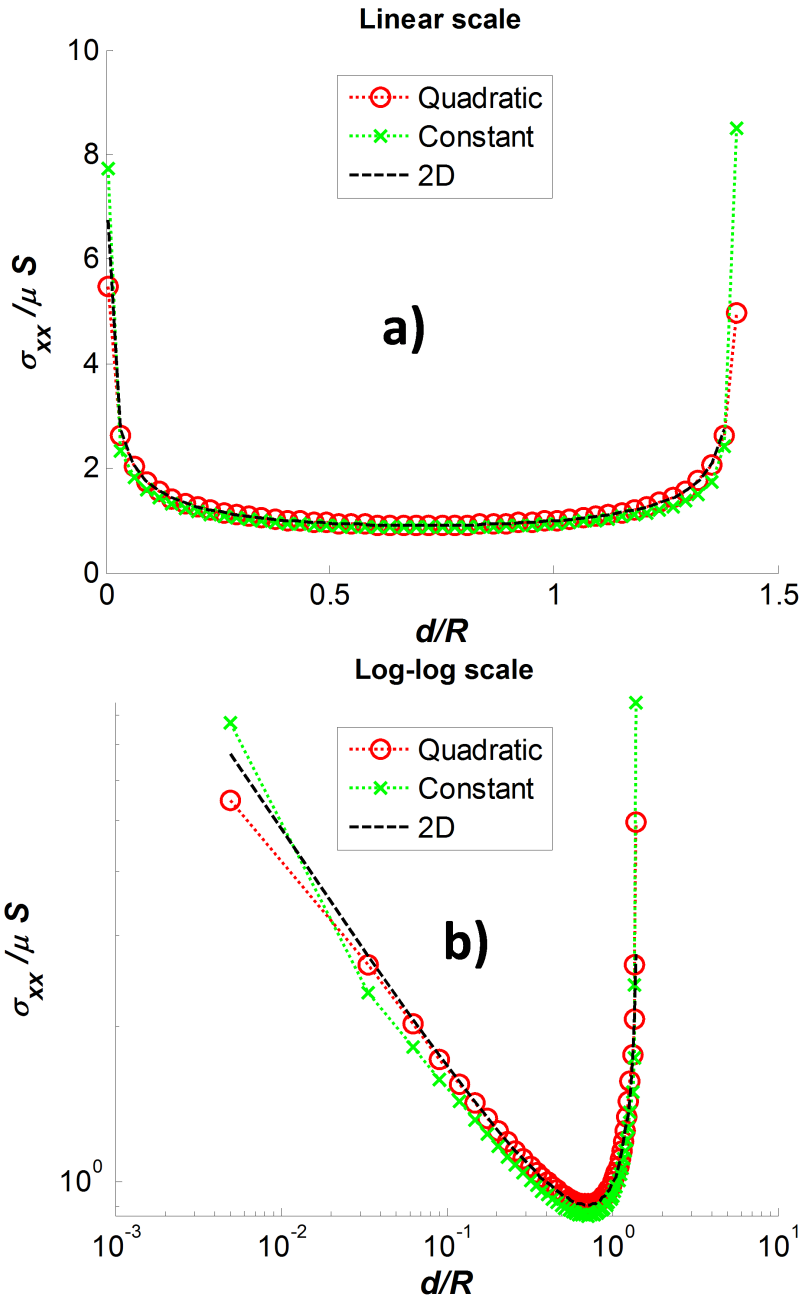

Figure 5.22: Two coaxial cylindrical cracks under biaxial tension. Dimensionless stress $\sigma_{xx}/\mu S$ near the crack tip (on the line AB in Fig. 5.21). **a**) linear scale; **b**) log-log scale.

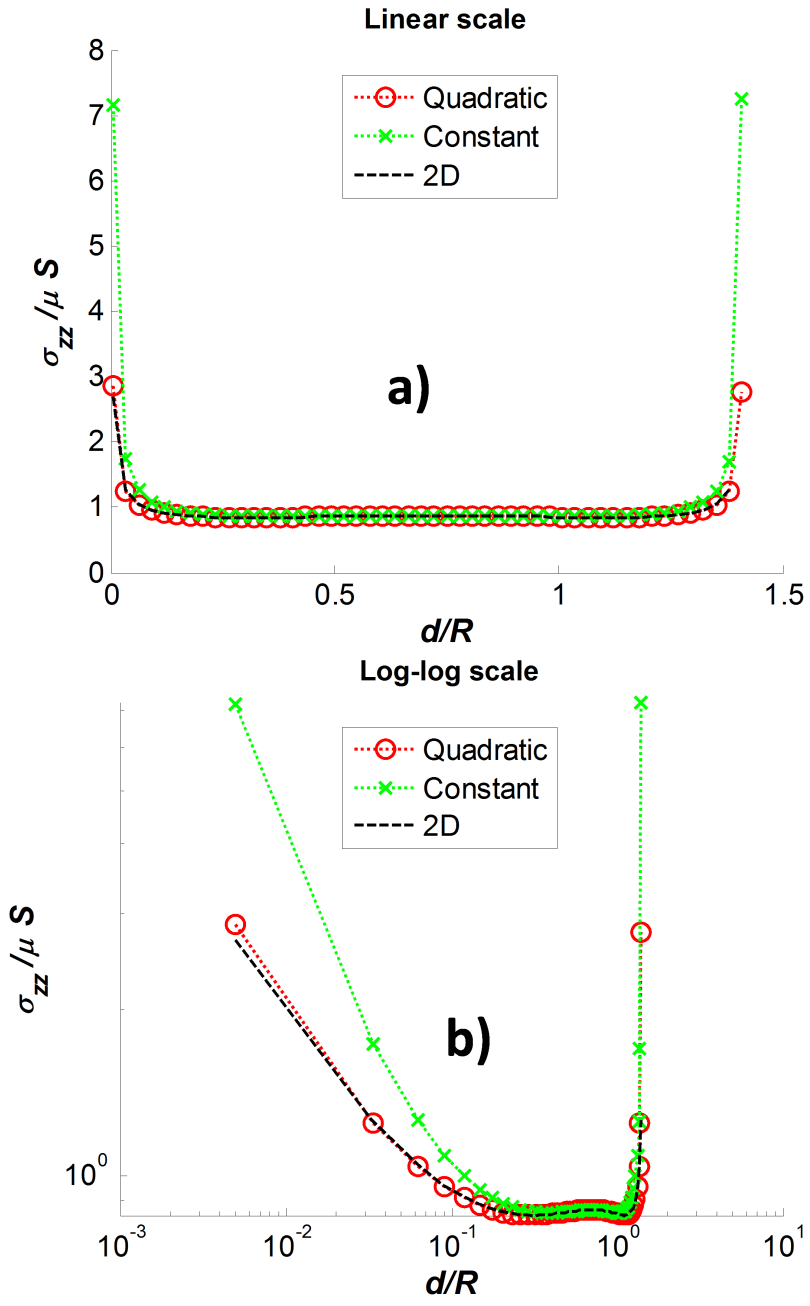

Figure 5.23: Two coaxial cylindrical cracks under biaxial tension. Dimensionless stress $\sigma_{zz}/\mu S$ near the crack tip (on the line AB in Fig. 5.21). **a**) linear scale; **b**) log-log scale.

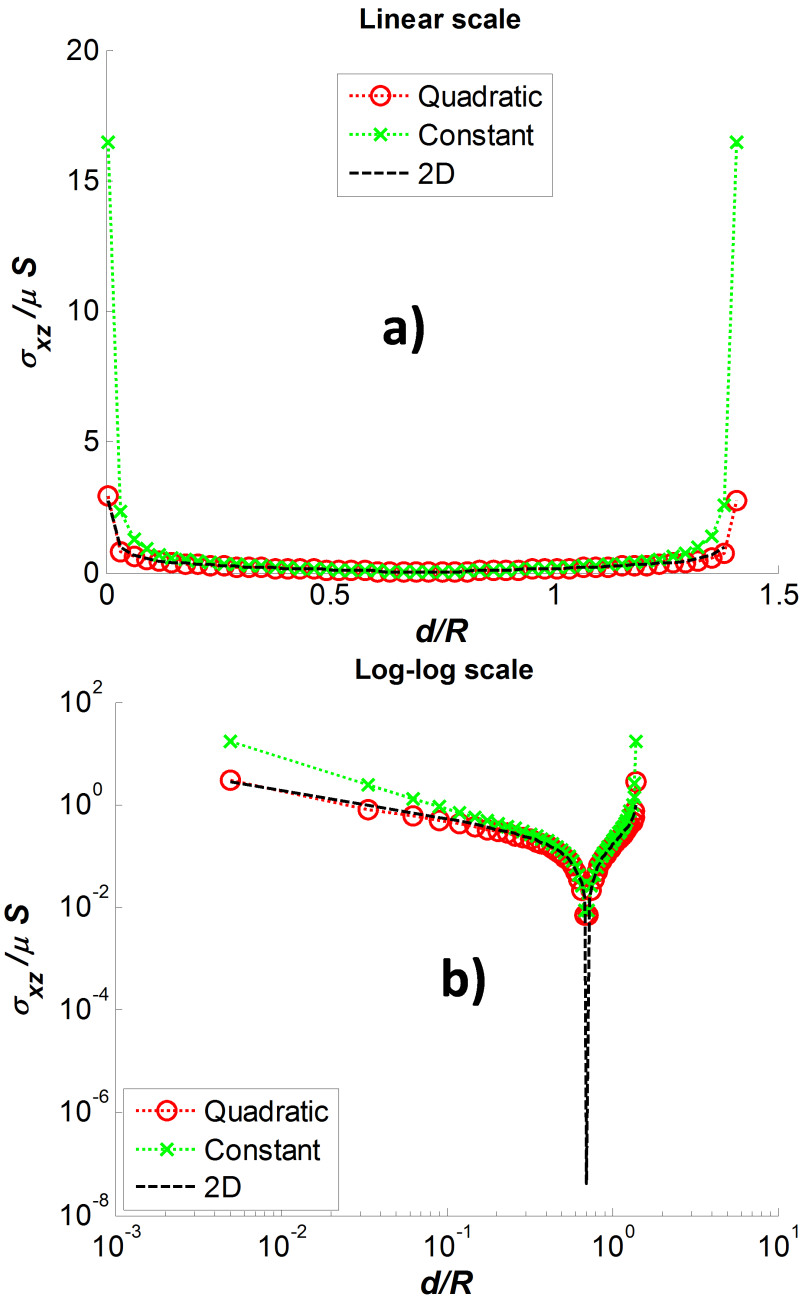

Figure 5.24: Two coaxial cylindrical cracks under biaxial tension. Dimensionless shear stress $\sigma_{xz}/\mu S$ near the crack tip (on the line AB in Fig. 5.21). **a**) linear scale; **b**) log-log scale.

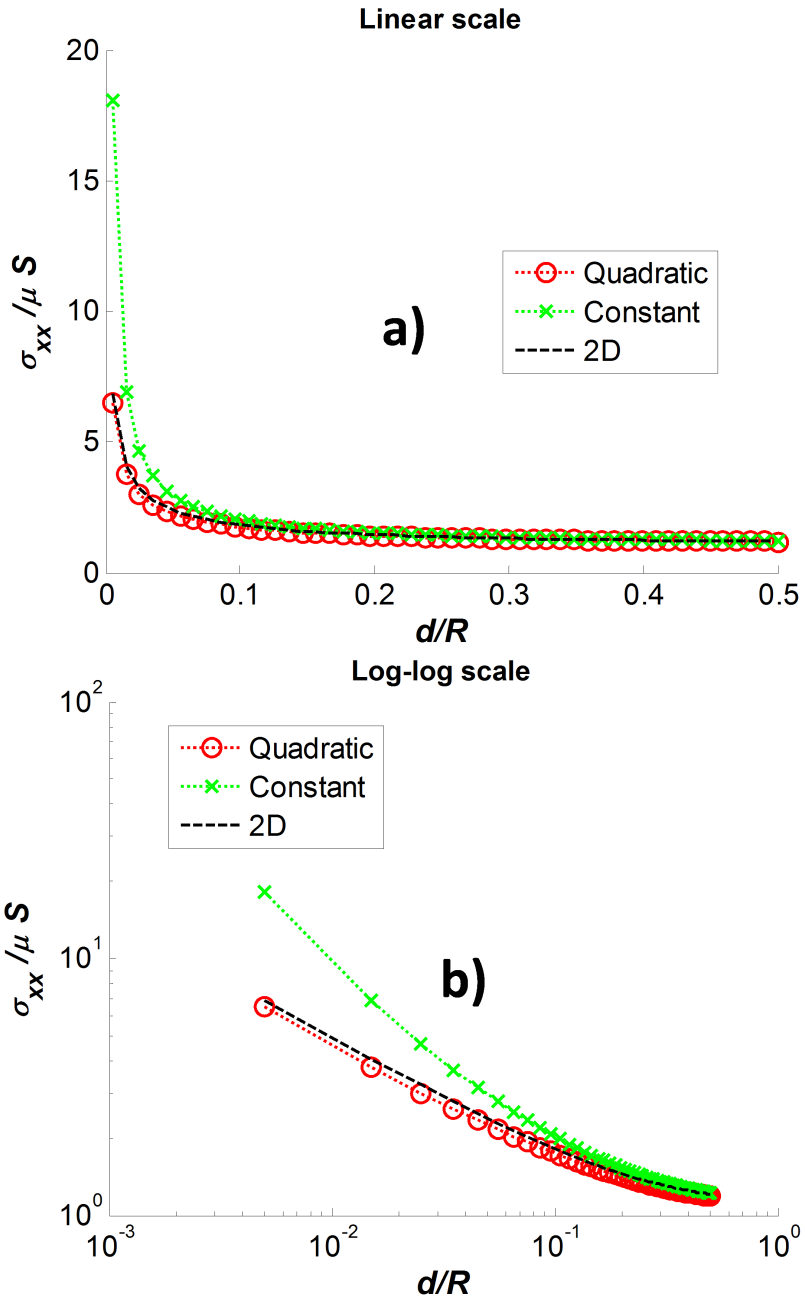

Figure 5.25: Two coaxial cylindrical cracks under biaxial tension. Dimensionless stress $\sigma_{xx}/\mu S$ near the crack tip (on the line CD in Fig. 5.21). **a**) linear scale; **b**) log-log scale.

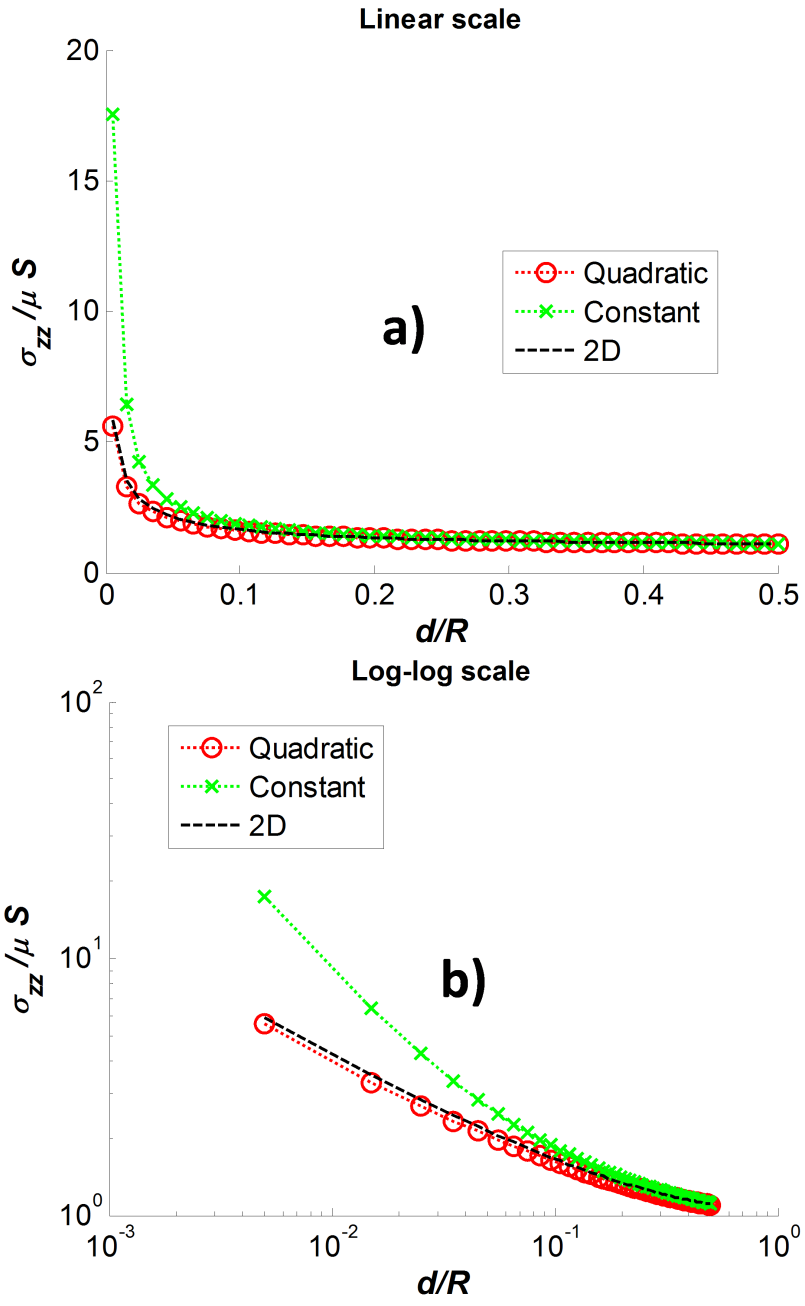

Figure 5.26: Two coaxial cylindrical cracks under biaxial tension. Dimensionless stress $\sigma_{zz}/\mu S$ near the crack tip (on the line CD in Fig. 5.21). **a**) linear scale; **b**) log-log scale.

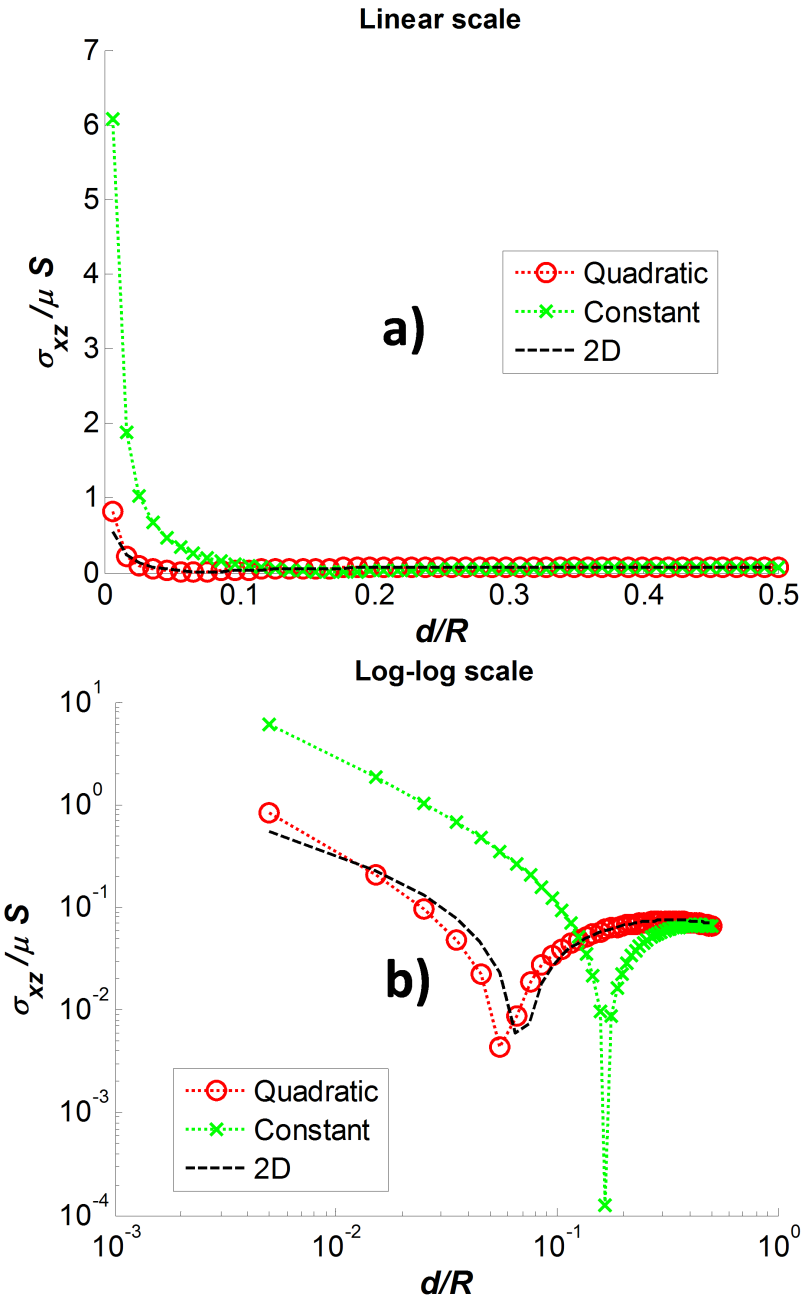

Figure 5.27: Two coaxial cylindrical cracks under biaxial tension. Dimensionless shear stress $\sigma_{xz}/\mu S$ near the crack tip (on the line CD in Fig. 5.21). **a**) linear scale; **b**) log-log scale.

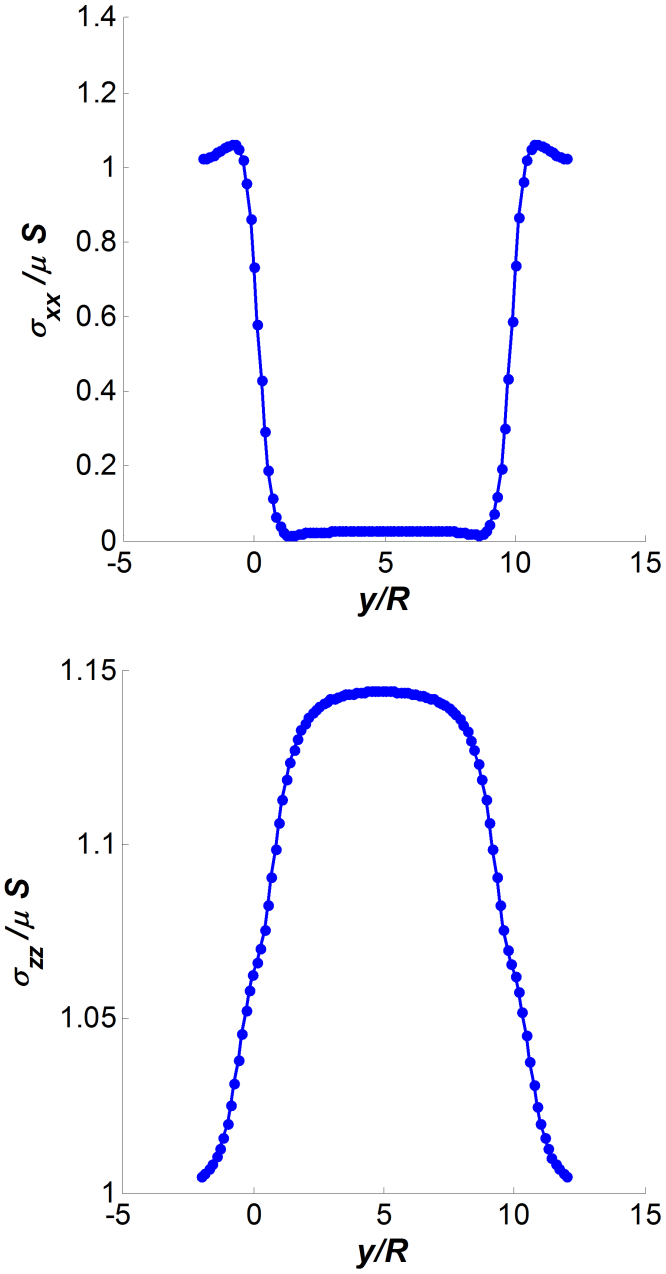

Figure 5.28: Two coaxial cylindrical cracks under biaxial tension. Dimensionless stresses ($\sigma_{xx}/\mu S$, $\sigma_{zz}/\mu S$) along the axial line.

5.5 A Uniformly Pressurized Borehole

Consider two cases of an infinite elastic medium containing a cylindrical hole that is uniformly pressurized in the radial direction and characterized by the following geometrical parameters (i) $L/R = 4$, Fig. 5.30 and (ii) $L/R = 10$, Fig. 5.31, where L is the length of the hole in axial direction and R is its radius.

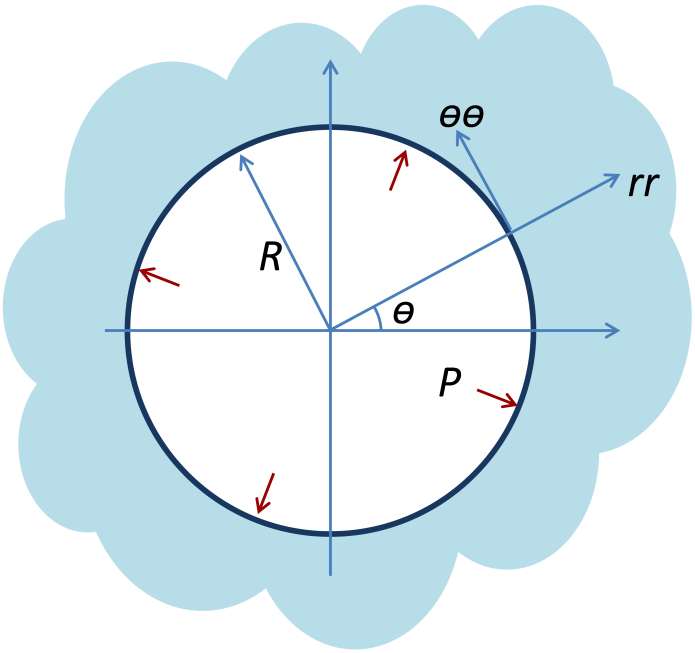

Figure 5.29: A circular hole in an infinite plane.

Three types of meshes were used to discretize cylindrical boundaries. For the first case, Fig. 5.30, one mesh characterized by the ratio $h_0/R = 0.52$, in which h_0 is the characteristic length scale of the boundary elements, was used. For the second case, Fig. 5.31, the following two meshes were used (i) $h_0/R = 0.52$ and (ii) $h_0/R = 0.26$.

As length L is longer than the radius R, it is reasonable to expect (especially in the

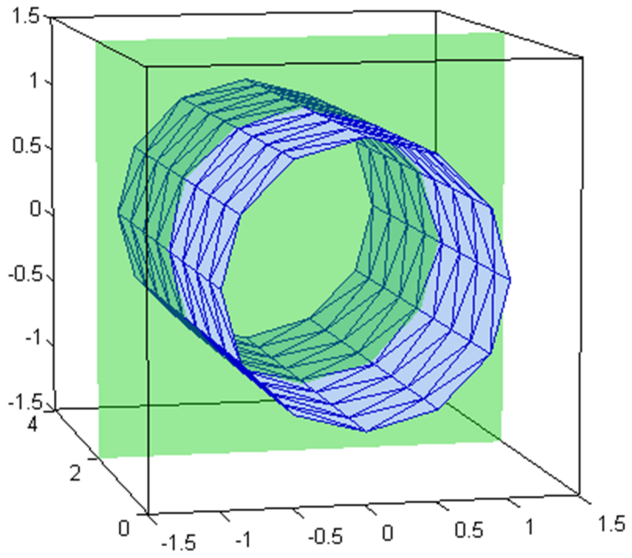

Figure 5.30: A mesh with $h_0/R = 0.52$ for a cylindrical hole with $L/R = 4$.

second case) that the fields in the middle cross-section of the hole (shown on Figs. 5.30 – 5.31) would mimic the solution of the two-dimensional problem of a circular hole subjected to uniform normal load, Fig. 5.29. The latter problem is axisymmetric and has the following analytical solution ([56]):

$$\sigma_{rr}/P = -R^2/r^2,\ \sigma_{\theta\theta}/P = R^2/r^2,\ \sigma_{r\theta}/P = 0 \tag{5.1}$$

in which P is applied pressure, r is the radial distance from the center of the circle, θ is shown in Fig. 5.29 and σ_{rr}, $\sigma_{\theta\theta}$, $\sigma_{r\theta}$ are the stresses in the local coordinate system shown on that figure.

Normalized circumferential (hoop) stress $\sigma_{\theta\theta}/P$ along a radial line is plotted on Fig. 5.32 for the holes with both aspect ratios. The results for the case $L/R = 10$ are shown for the finer mesh only, although the coarse mesh provided quite accurate results as well. It can be seen that the hoop stress is indeed consistent with two-dimensional

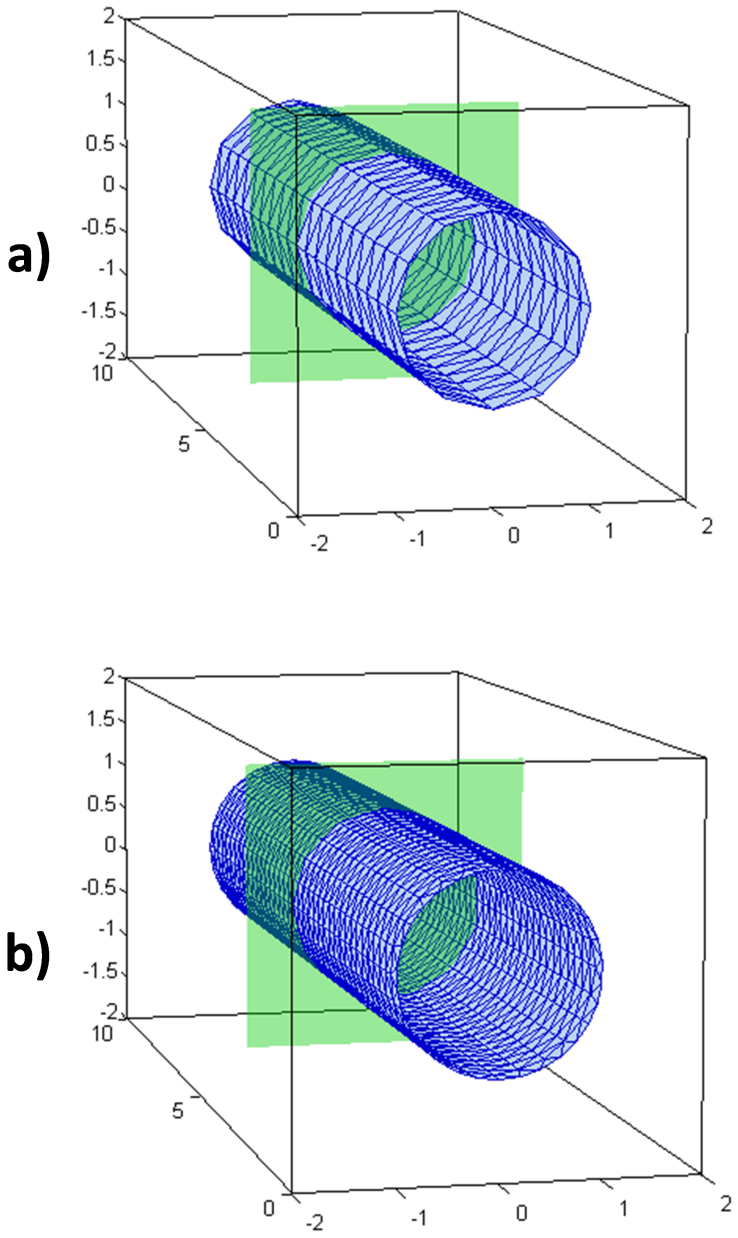

Figure 5.31: Mesh examples for a cylindrical hole with $L/R = 10$: **a**) $h_0/R = 0.52$; **b**) $h_0/R = 0.26$.

stress of the second equation of Eq.(5.1) even for the case of the hole with smaller aspect ratio. The stresses evaluated on the lines with different θ should be the same and this was indeed observed with reasonable accuracy.

Normalized stress σ_{rr}/P near the hole with smaller aspect ratio computed along two radial lines is plotted on Fig. 5.33. While this stress should be again the same for all radial lines, the computed stress does vary with θ due to the discretization induced errors. In addition the two-dimensional solution is not well reproduced for this aspect ratio.

The same normalized stress is plotted in Fig. 5.34 for the hole with larger aspect ratio discretized with both meshes. It can be seen that this stress reproduces the two-dimensional stress of the first equation of Eq.(5.1) quite well. The figure also illustrates mesh convergence of the solution. The results obtained for different θ are reasonably consistent; the dependence on θ is pronounced only for small distances to the borehole, less than the characteristic mesh scale.

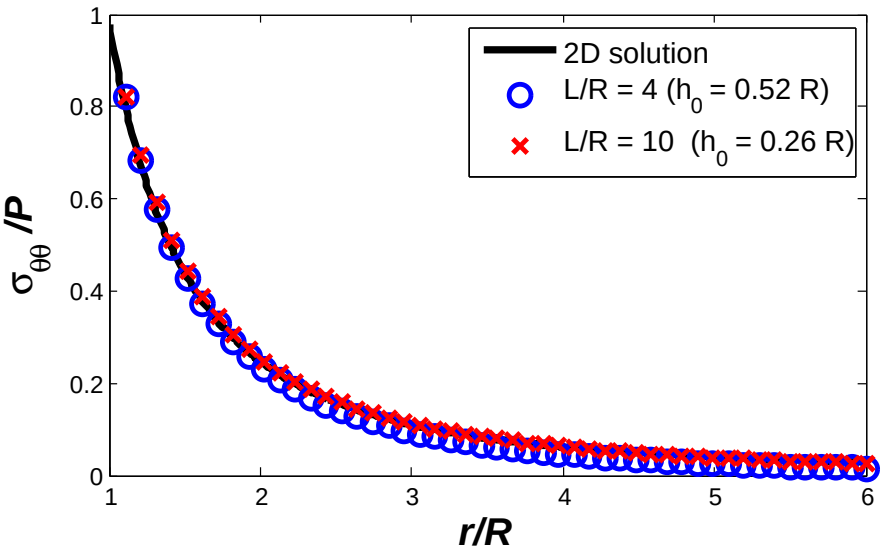

Figure 5.32: A uniformly pressurized borehole. Normalized hoop stress along a radial line.

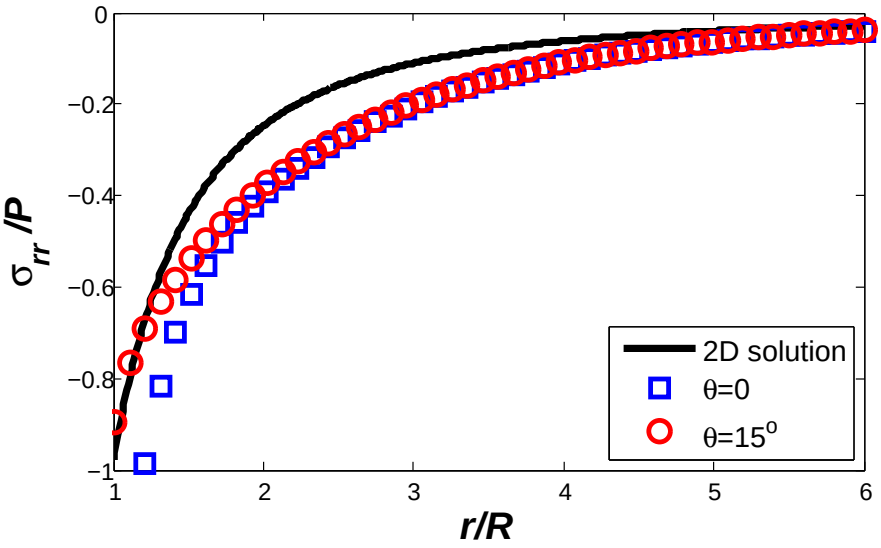

Figure 5.33: A uniformly pressurized borehole. Normalized radial stress σ_{rr}/P along two radial lines for$L/R = 4$.

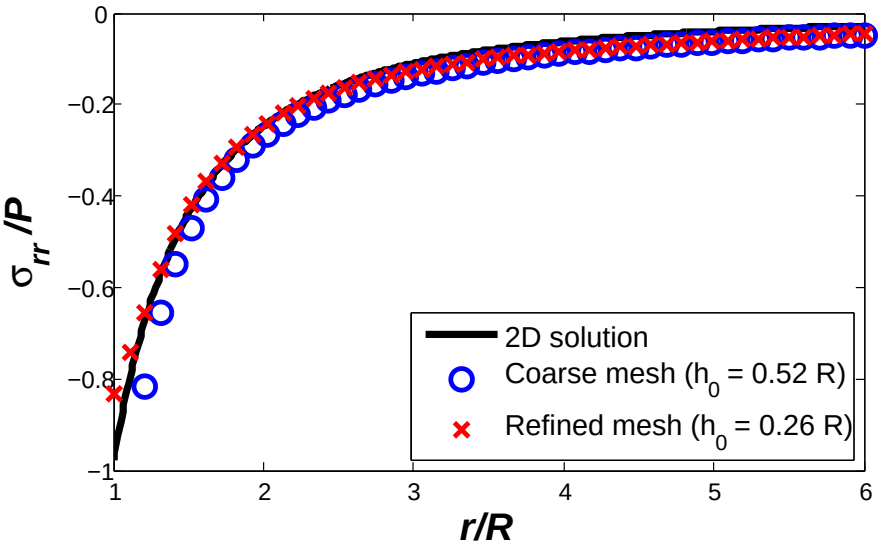

Figure 5.34: A uniformly pressurized borehole. Normalized radial stress σ_{rr}/P along a radial line for $L/R = 10$.

5.6 A Pressurized Borehole with Emanating Cracks

Consider a homogeneous elastic isotropic medium with a cylindrical hole of radius R and length L, representing a section of a wellbore, the general case of which is shown on Fig. 5.35. Two pre-existing planar cracks with circular front of radius R_c and length in axial direction a originate from the borehole parallel to its axis. Uniform pressure P is applied to the boundary of the borehole and uniform loads σ_{11}^{∞}, σ_{22}^{∞}, σ_{12}^{∞} are applied at the infinity. It is assumed that, in general, the axis of the borehole is inclined to the vertical direction by the angle α.

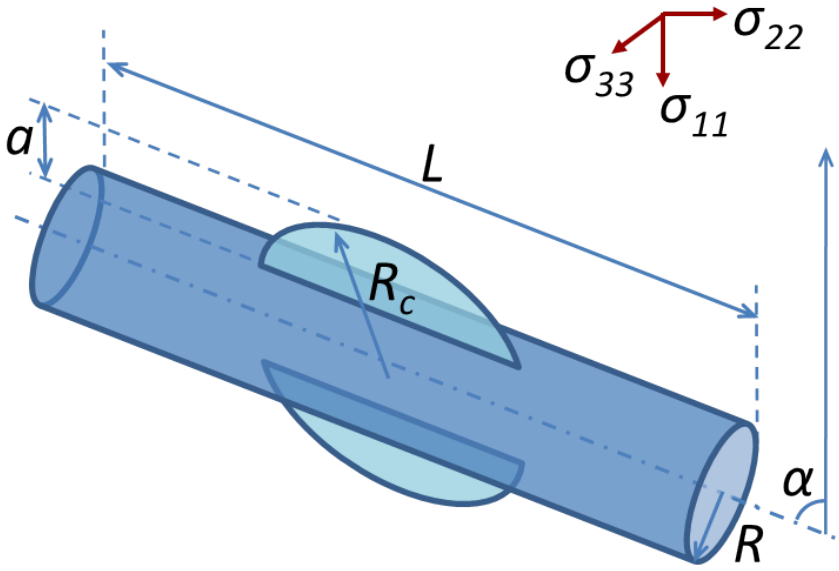

Figure 5.35: An example of borehole-crack system.

In the following example, a simplified problem is considered; the load at infinity is considered zero, the borehole axis is horizontal, each crack occupies a segment of the circle with the center at the center of symmetry of the borehole. The following geomerical parameters were taken: $L/R = 8$, $a/R = 1$, $R_c/R = 2$, in which L is the

axial length of the borehole, R is its radius, a is the length of each crack in radial direction, and R_c is the radius of the crack front (tip) circle. Two loading cases were studied:

a) the cracks and the borehole are uniformly pressurized with the same pressure P

b) only the borehole is pressurized and the cracks are traction-free

The problem was solved using the approach presented in the manuscript using quadratic approximations for the unknown displacements at the boundary of the hole and displacement discontinuities at the cracks surfaces. The meshes were characterized by the length scale of the boundary elements h_0 (same for all boundaries) given by the ratios $h_0/R = 0.48$ (422 elements) and $h_0/R = 0.2$ (3140 elements), respectively.

Normalized stresses σ_{xx}/P, σ_{zz}/P, σ_{xz}/P along several lines in the middle cross-section of the borehole shown on Fig. 5.35 (a dashed line at angle θ with respect to the crack plane is shown on Fig. 5.37) are evaluated and compared with the corresponding stresses due to the solution of the two-dimensional problem shown in that figure. The latter problem is solved using an algorithm described in [51] that employed quadratic approximation for the unknown functions, 72 circular arc elements for the hole boundary and 12 srtaight elements for each of two cracks.

The results are shown in Figs. 5.38, 5.39, 5.41, and 5.43a – 5.46a for the loading case (a) and in Figs. 5.40, 5.42, and 5.43b – 5.46b for the loading case (b). It cannot be expected that the two-dimensional solutions will be accurately reproduced in such fully three-dimensional setting, however, reasonable qualitative agreement is observed.

As expected (see e.g. [13]), higher stresses are observed in case of pressurized cracks than in that of traction-free cracks. The shear stress vanishes with reasonable accuracy on the vertical line (Fig. 5.45). The observed non-zero values are due to non-symmetrical placement of collocation points.

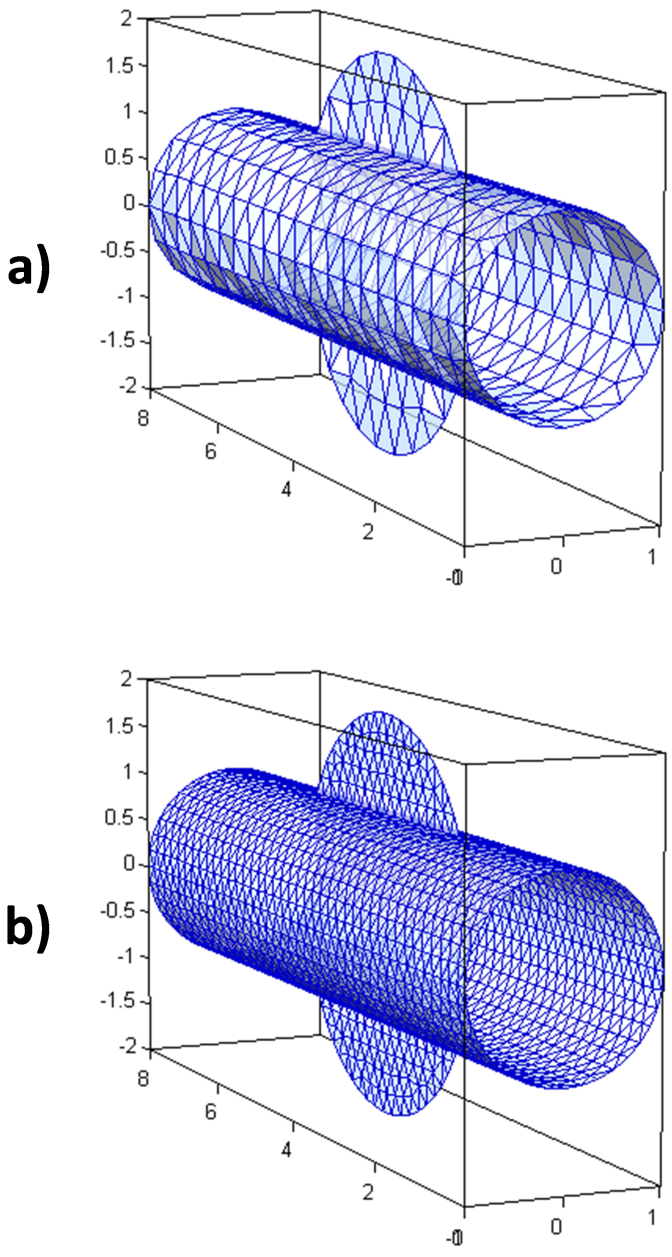

Figure 5.36: Two cracks emanating from a borehole, $L/R = 8$, $a/R = 1$, $R_c/R = 2$. Two examples of boundary mesh, $h_0/R = 0.48$ and $h_0/R = 0.2$.

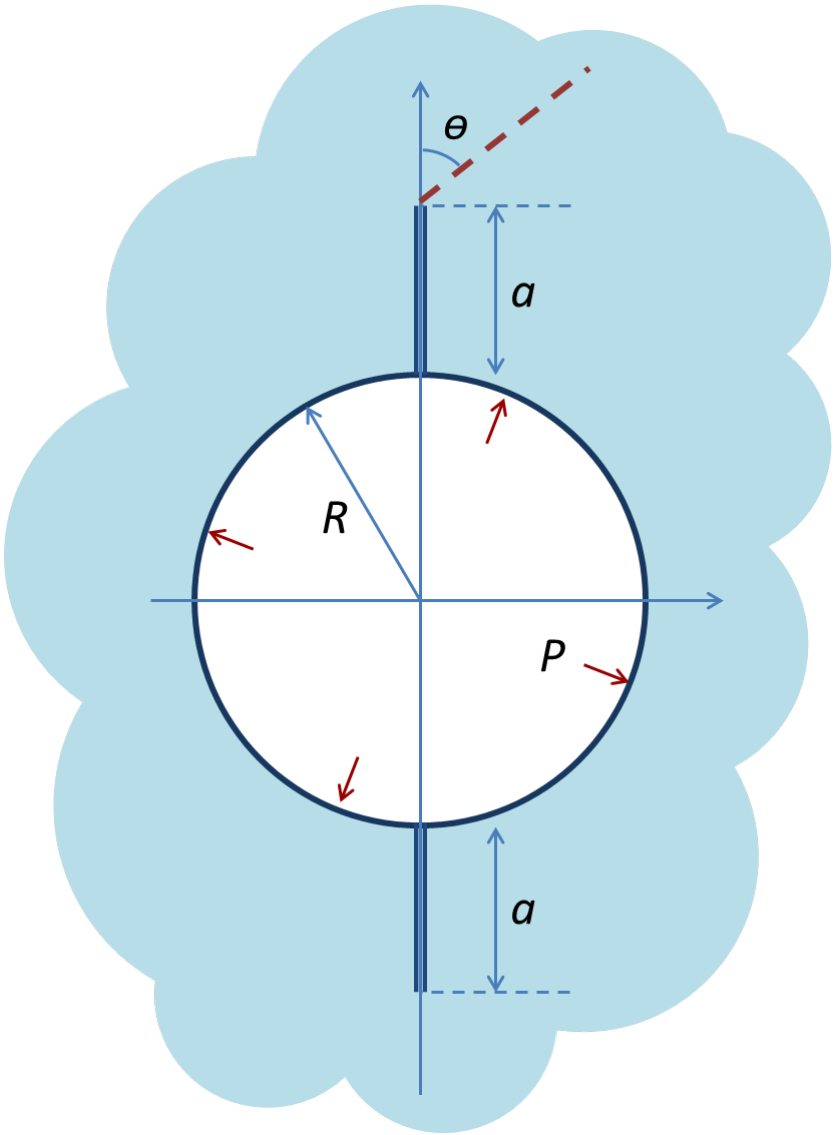

Figure 5.37: Two cracks emanating from a circular hole in an infinite plane.

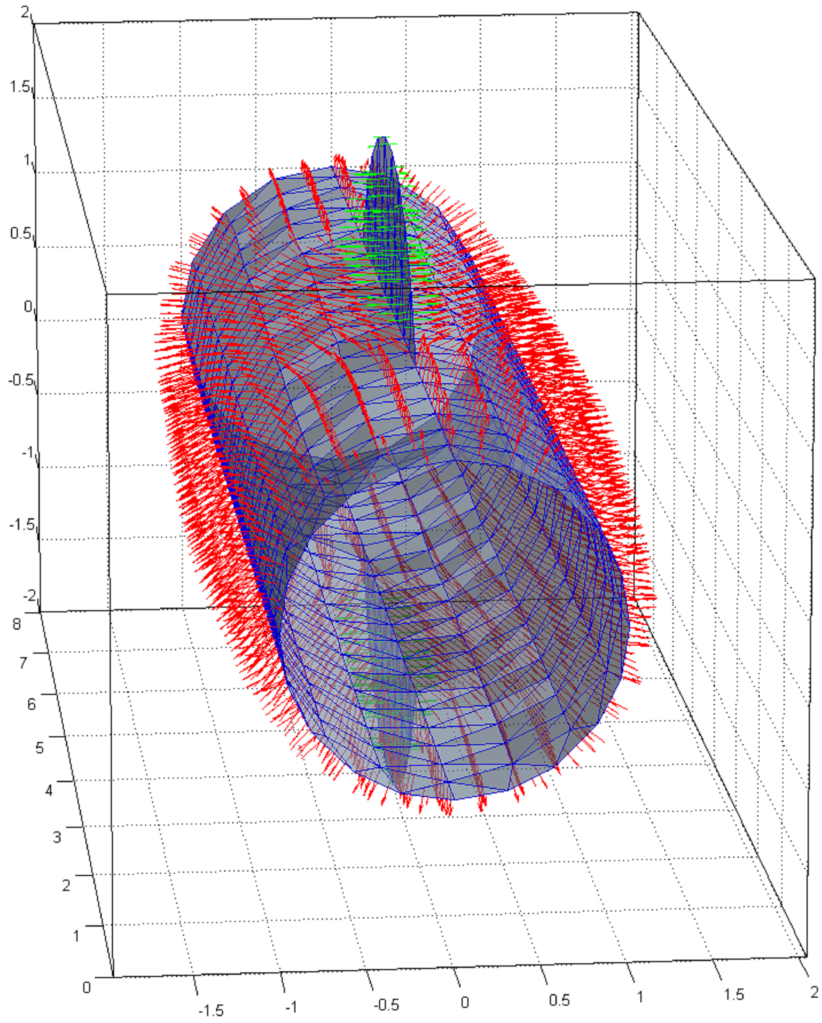

Figure 5.38: Normalized boundary displacements $\frac{\mathbf{u}^{(N)}\mu}{PR}$ and displacement discontinuities $\frac{\triangle\mathbf{u}^{(N)}\mu}{PR}$ on a borehole with two pressurized emanating cracks; $h_0/R = 0.48$.

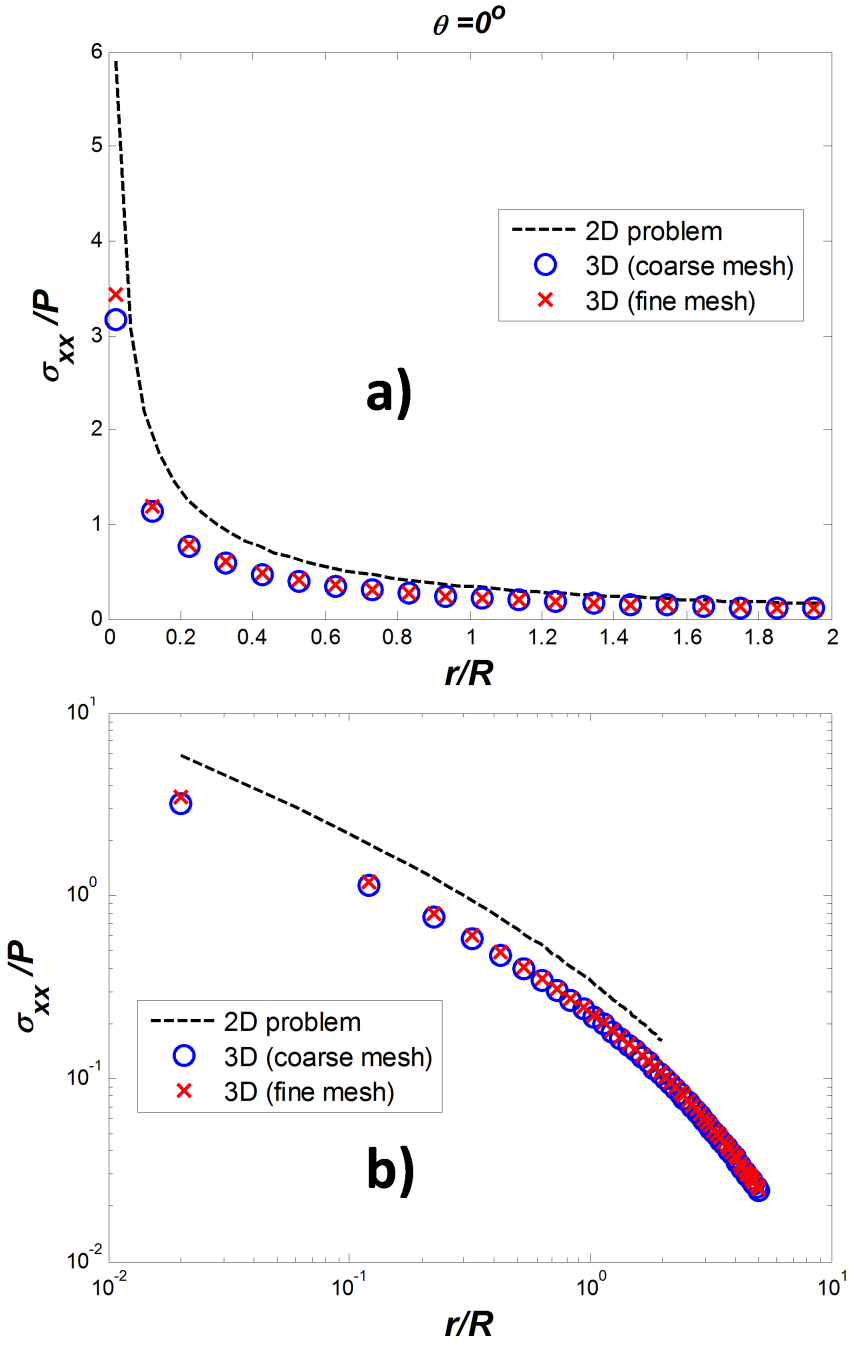

Figure 5.39: Normalized stress σ_{xx}/P in the middle cross-section of a borehole with two pressurized emanating cracks. **a**) linear scale; **b**) log-log scale.

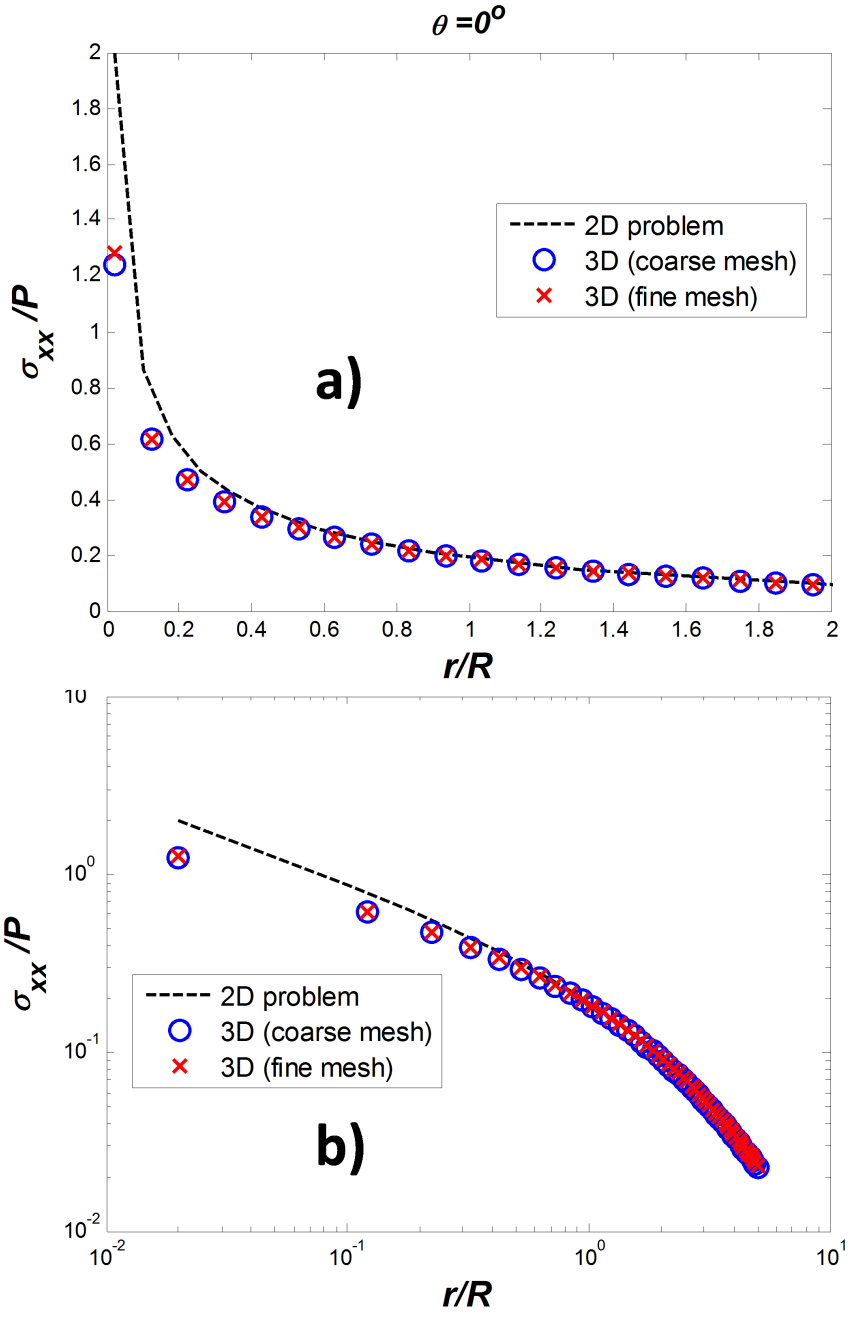

Figure 5.40: Normalized stress σ_{xx}/P in the middle cross-section of a borehole with two traction-free emanating cracks. **a**) linear scale; **b**) log-log scale.

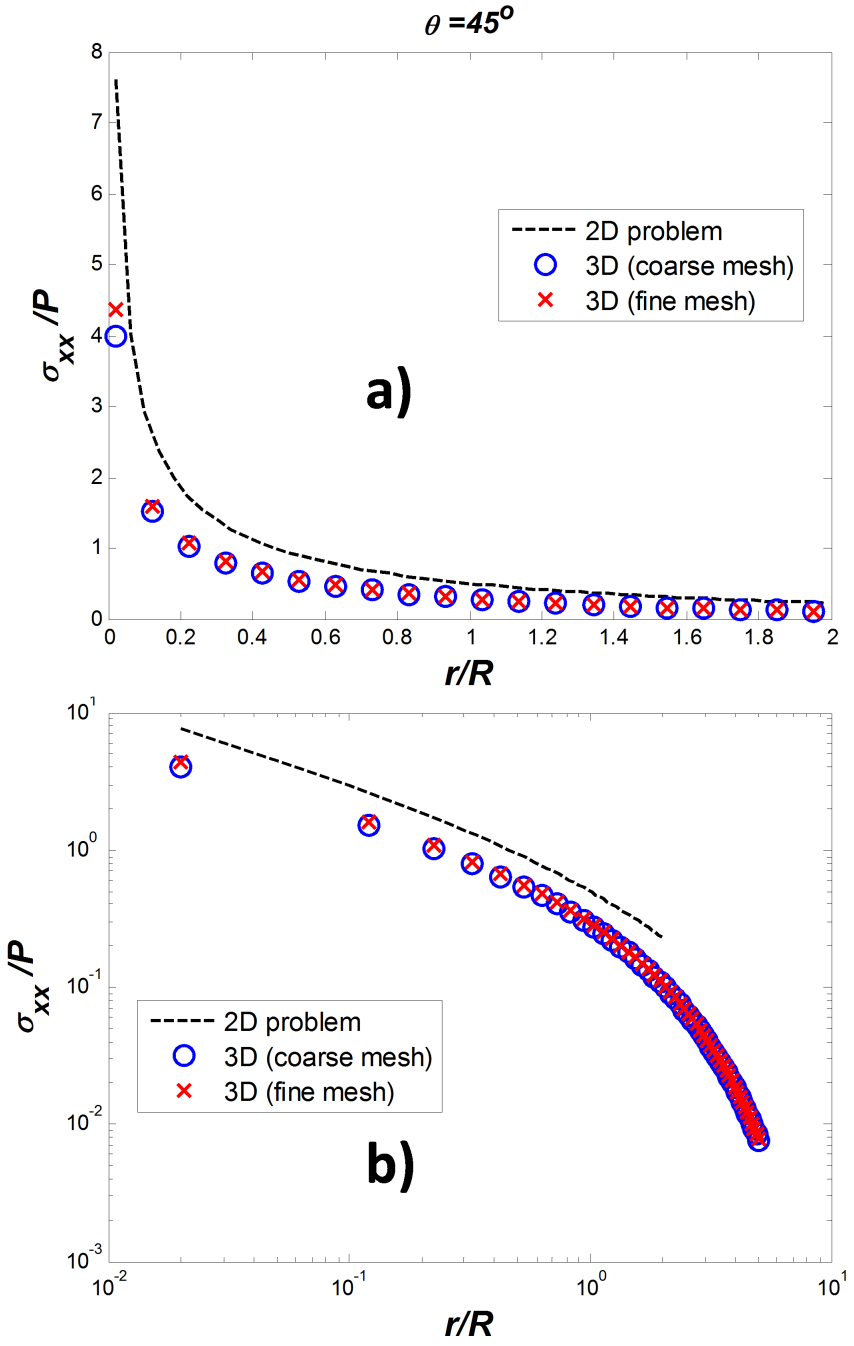

Figure 5.41: Normalized stress σ_{xx}/P in the middle cross-section of a borehole with two pressurized emanating cracks. **a**) linear scale; **b**) log-log scale.

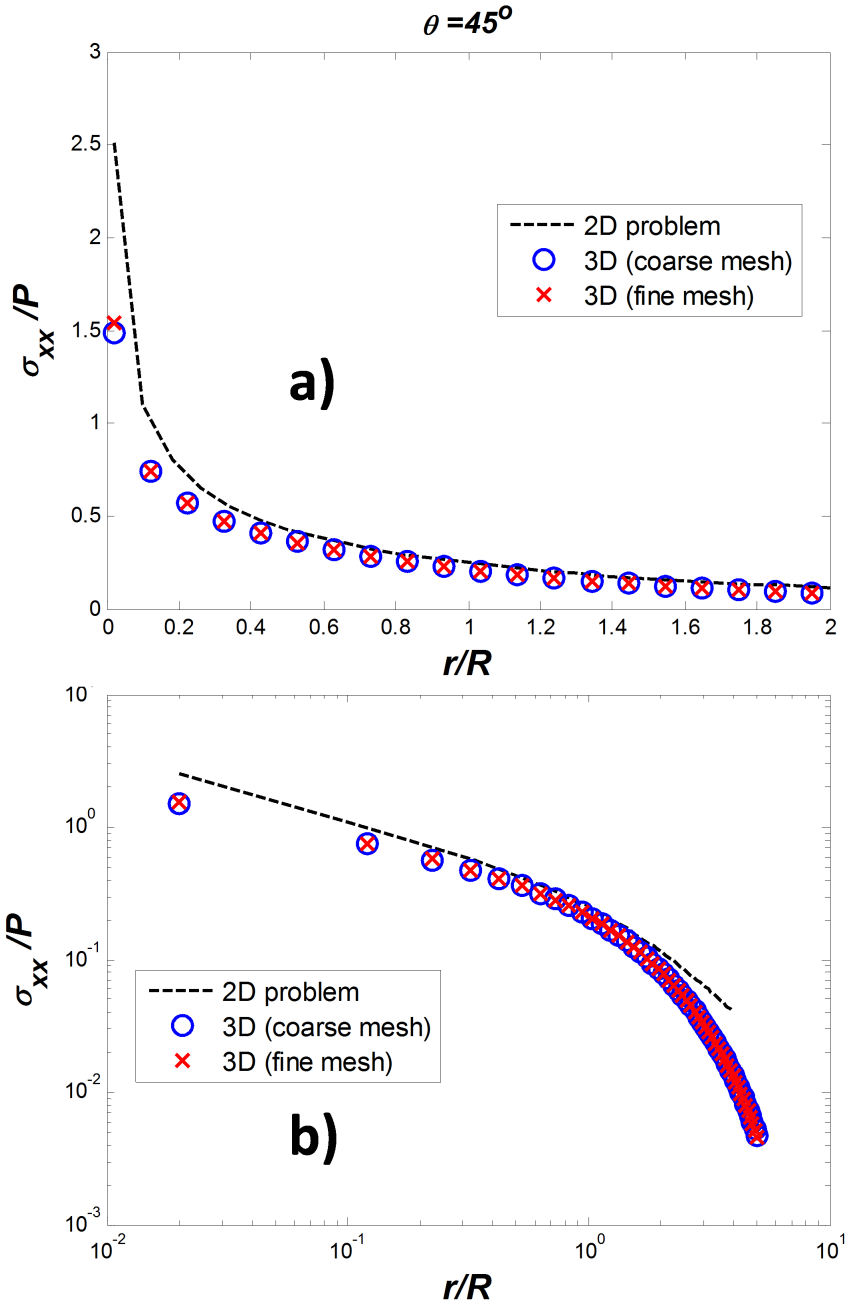

Figure 5.42: Normalized stress σ_{xx}/P in the middle cross-section of a borehole with two traction-free emanating cracks. **a**) linear scale; **b**) log-log scale.

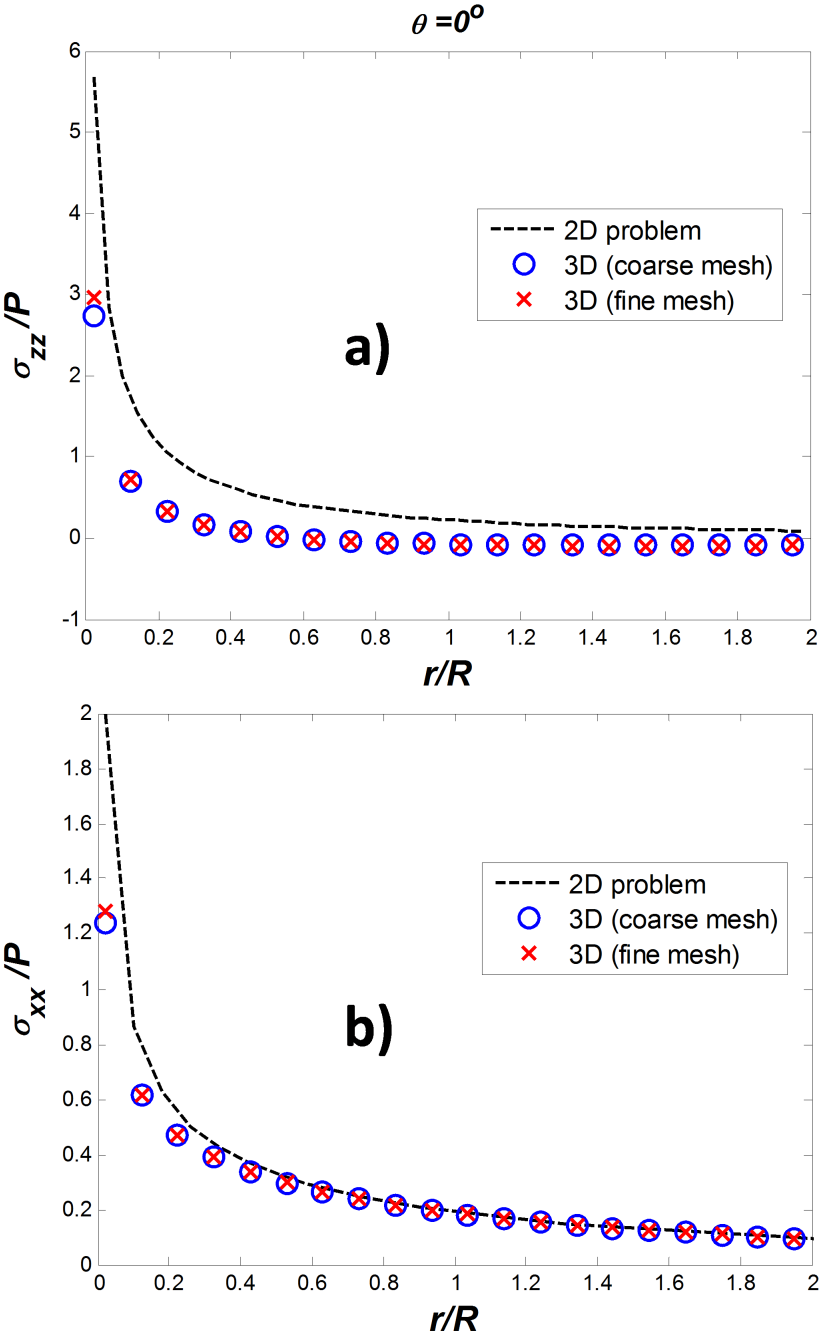

Figure 5.43: Normalized stress σ_{zz}/P in the middle cross-section of a borehole with two emanating cracks. **a**) pressurized cracks; **b**) traction-free cracks.

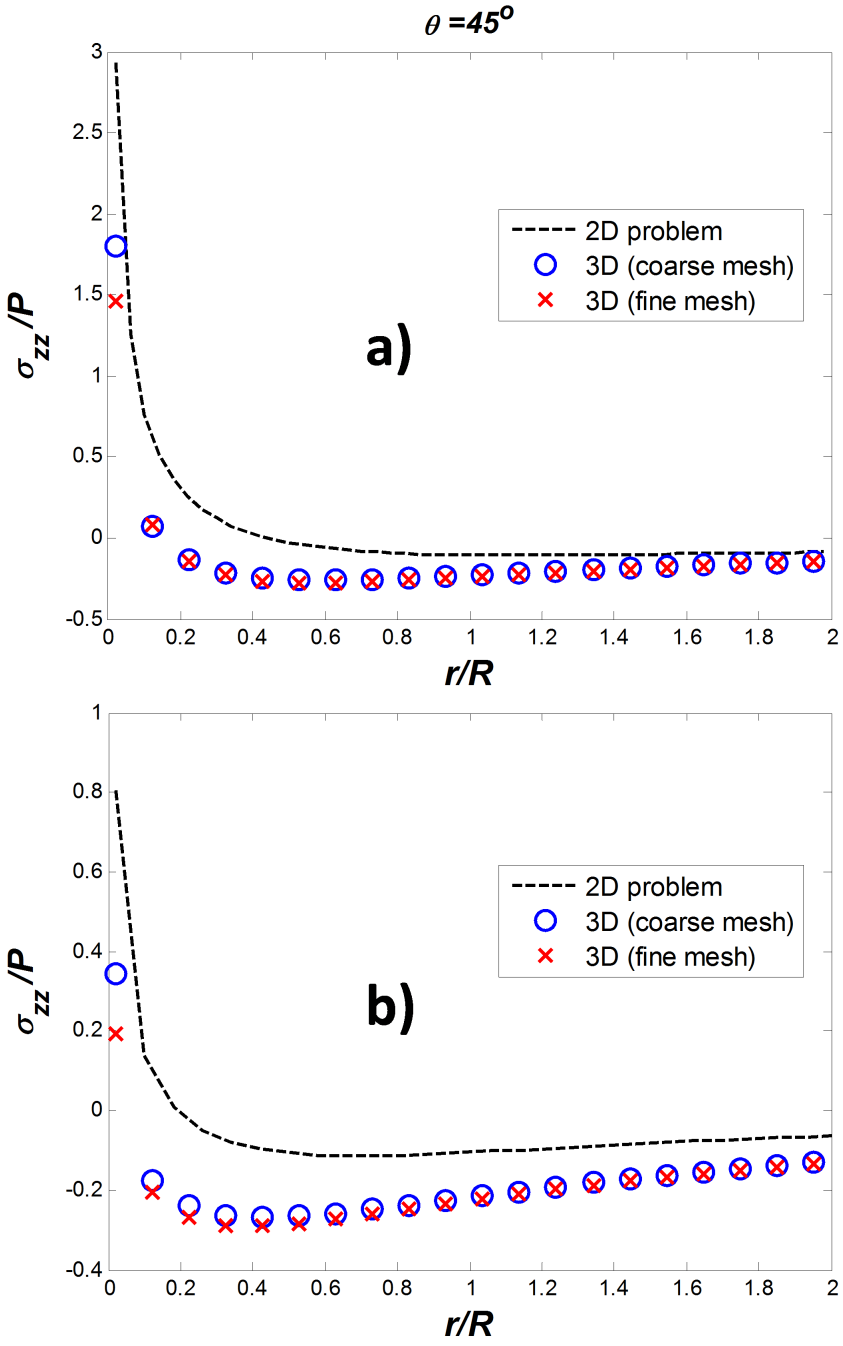

Figure 5.44: Normalized stress σ_{zz}/P in the middle cross-section of a borehole with two emanating cracks. **a**) pressurized cracks; **b**) traction-free cracks.

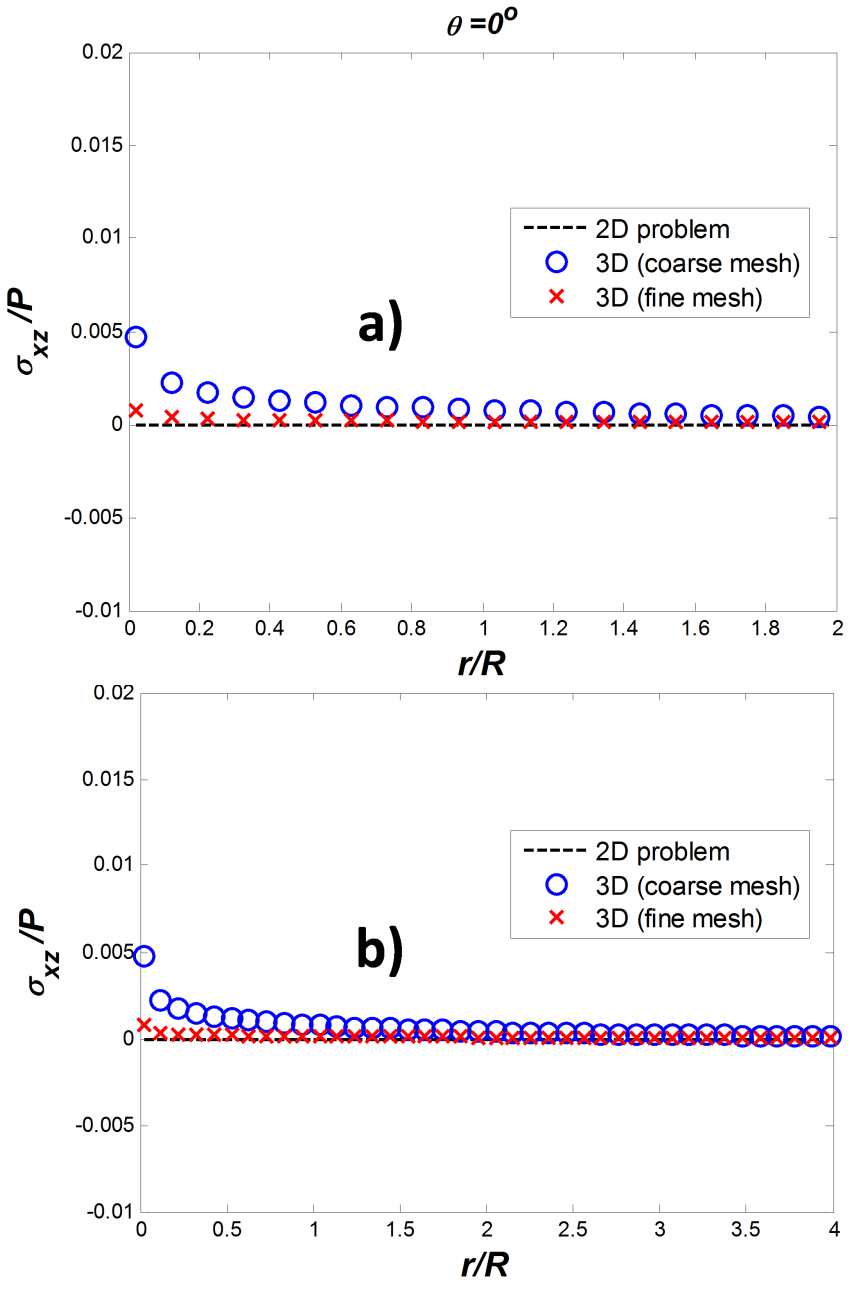

Figure 5.45: Normalized stress σ_{xz}/P in the middle cross-section of a borehole with two emanating cracks. **a**) pressurized cracks; **b**) traction-free cracks.

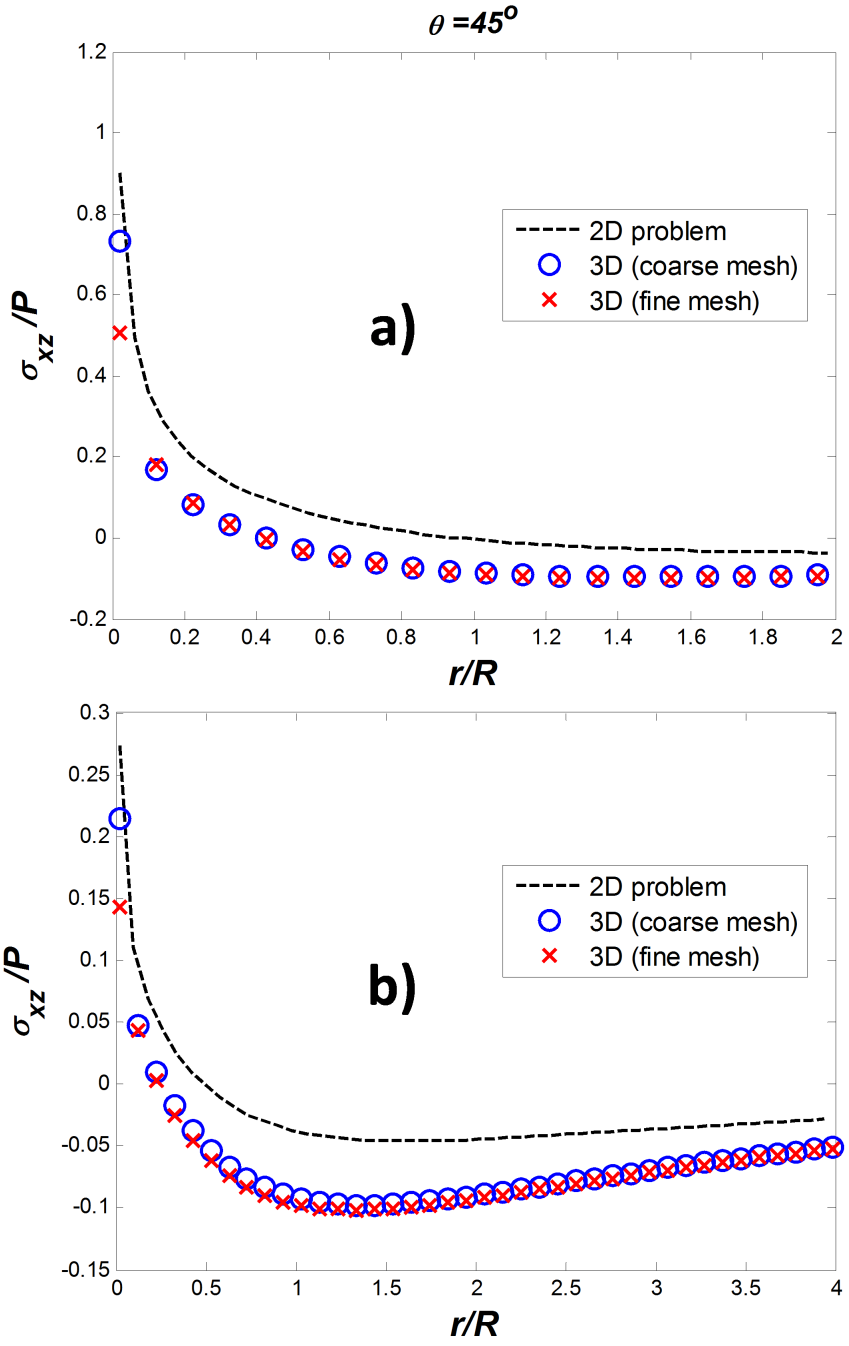

Figure 5.46: Normalized stress σ_{xz}/P in the middle cross-section of a borehole with two emanating cracks. **a**) pressurized cracks; **b**) traction-free cracks.

Chapter 6

Conclusion and Future Work

A new Boundary Element Method-based technique for analysis of multiple three-dimensional cracks of arbitrary shapes is proposed. The technique employs planar triangular elements to discretize the boundaries and quadratic polynomials to approximate the boundary unknowns, with two options of the arrangement of the nodal points on the elements. The novel features of the technique include the following:

- the use of complex variable formalism involving various combinations of the geometrical parameters and the elastic fields, e.g. components of tractions and displacement discontinuities in the plane of the considered element;
- analytical integration with the use of Cauchy-Pompeiu formula to reduce the surface integrals to the contour ones;
- "limit after integration" approach, i.e. enforcing the boundary conditions after the discretization and analytical handling of the internal fields, by allowing the field point to reach the boundaries.

The use of complex variable formalism significantly reduces the effort of the analytical integration over the boundary elements and the number of the integral terms,

as compared to real variables-based approaches. Since the limits as the field point approaches the boundary are taken after the approximation of the boundary and the unknown functions, no singular integrals are involved. Furthermore, there is no need for an additional procedure for evaluation of the elastic fields inside the domain; they are evaluated by the same procedure as the one used to set up the system of linear algebraic equations for the boundary unknowns. Analytical integration leads to higher accuracy of calculations and allows for saving computational time. In addition, it could help to facilitate the use of fast solving techniques, e.g. the Fast Multipole Method (see, e.g., [47]).

Significant features of the code include using MATLAB as the programming tool. MATLAB is a high-level language for numerical computations that features built-in linear algebra functions, parallel computing, graphics for data visualization, and could be easily integrated with external applications and languages. This would constitute a significant advantage over specific available Fortran-based codes.

The approach developed to date can be used in a straightforward manner to model quasistatic crack propagation. The present elastostatic model can be used on each step in combination with the appropriate crack propagation criterion.

Computational cost associated with the three-dimensional problems of the kind considered here is quite high. Therefore, future work will be concerned with the efficient assembly of the matrix of the linear algebraic system with the use of parallel computing (partly implemented in the computer code used for the reported simulations) and the solution of this system via available fast solvers. The further developments will include incorporation of fluid flow, e.g. the models described in [1, 14], into the computer code. This work is in progress.

In addition, the method can be generalized to allow for treatment of inhomogeneities (using standard multi-region formulation, see e.g. [42]), and arbitrary body force distribution. The analytical expressions obtained here could also be useful in developing multipole expansions employed in fast multipole methods.

References

[1] Adachi J., Siebrits E., Peirce A., Desroches J. Computer simulation of hydraulic fractures. *International Journal of Rock Mechanics and Mining Sciences* 2007; **44**: 739–757

[2] Aliabadi M.H. *Boundary element method: Applications to solids and structures* vol. **2** Chicester: John Wiley & Sons, Ltd.; 2002

[3] Banerjee P.K., Butterfield R. *Boundary Element Methods in Engineering.* London: McGraw-Hill; 1981

[4] Barber J.R. *Solid mechanics and its applications: Elasticity.* London, New York: Springer Science; 2010

[5] Bonnet M. *Boundary Integral Equation Methods for Solids and Fluids.* Chicester, England: John Wiley & Sons, Ltd.; 1999

[6] Brebbia C.A., Telles J.C.F., Wrobel L.C. *Boundary Element Techniques.* Berlin: Springer; 1984

[7] Carini A., Salvadori A. Analytical integrations in 3D BEM: preliminaries. *Computational Mechanics* 2002; **28**: 177–185

[8] Carley M., Analytical formulae for potential integrals on triangles. *Journal of Applied Mechanics* 2013; **80**: 041008

[9] Chen JT, Hong H-K. Review of dual boundary element methods with emphasis on hypersingular integrals and divergent series. *Applied Mechanics Reviews, ASME* 1999; **52** (1):17–33

[10] Crouch S.L. Solution of plane elasticity problems by displacement discontinuity method. *International Journal for Numerical Methods in Engineering* 1976; **10**: 301–343

[11] Crouch S.L., Starfield A.M. *Boundary element methods in solid mechanics.* London: Allen and Unwin; 1983

[12] Cruse T.A. *Boundary Element Analysis in Computational Fracture Mechanics.* Dordrecht, Boston, London: Kluwer academic publishers; 1998

[13] Detournay E., Jeffrey R.G. Stress conditions for initiation of secondary fractures from a fractured borehole. *Proceedings of the International Symposium on Rock Stress and Rock Stress Measurements.* Stockholm; 1986: 281–288

[14] Detournay E., Napier J.A.L. Propagation of non-planar pressurized cracks from a borehole. In: *Proceedings of the Fifth International Conference on Structural Engineering, Mechanics and Computation.* 2013: 597–602

[15] Fabrikant VI. Penny-shaped crack revisited: closed-form solutions. *Philosophical Magazine A.* 1987; **56** (2): 191-207

[16] Frangi A., Novati G., Springhetti R., Rovizzi M. 3D fracture analysis by the symmetric Galerkin BEM. *Computational Mechanics.* 2002; **28**: 220–232

[17] Frangi A. Fracture propagation in 3D by the symmetric Galerkin boundary element method. *International Journal of Fracture.* 2002; **116**: 313–330

[18] Gaul L., Kögl M., Wagner M., *Boundary Element Methods for Engineers and Scientists. An Introductory Course with Advanced Topics.* Berlin: Springer; 2003

[19] Gordeliy E., Peirce A. Coupling schemes for modeling hydraulic fracture propagation using the XFEM. *Computer Methods in Applied Mechanics and Engineering* 2013; **253**: 305–322. DOI: 10.1016/j.cma.2012.08.017

[20] Gordeliy E., Peirce A. Implicit level set schemes for modeling hydraulic fractures using the XFEM. *Computer Methods in Applied Mechanics and Engineering* 2013; **266**: 125–143. DOI: 10.1016/j.cma.2013.07.016

[21] Gradshteyn I.S., Ryzhik I.M. *Table of Integrals, Series, and Products, sixth edition.* San Diego, San Francisco, New York, Boston, London, Sydney, Tokyo: Academic press; 2000

[22] Green A.E. On Boussinesq's problem and penny-shaped cracks. *Mathematical Proceedings of the Cambridge Philosophical Society.* 1949; **45** (2): 251–257

[23] Green A.E., Zerna W. *Theoretical Elasticity.* London: Oxford University Press; 1968

[24] Gupta P., Duarte C.A. Simulation of non-planar three-dimensional hydraulic fracture propagation. *International Journal for Numerical and Analytical Methods in Geomechanics* 2014; **38**: 1397–1430

[25] Hadamard J. 1952. *Lectures on Cauchys Problem in Linear Partial Differential Equations.* New Haven: Yale University Press; 1923; New York: Dover Publications; 1952

[26] Hong H.-K., Chen J.T. Derivations of Integral Equations of Elasticity. *Journal of Engineering Mechanics, ASCE* 1988; **114** (6):1028–1044

[27] Ioakimidis N.I. Application of finite-part integrals to the singular integral equations of crack problems in plane and three-dimensional elasticity. *Acta Mechanica* 1982; **45**: 31–47

[28] Ioakimidis N.I. A natural approach to the introduction of finite-part integrals into crack problems of three-dimensional elasticity. *Engineering Fracture Mechanics* 1982; **16**: 669–673

[29] Ioakimidis N.I. Validity of the hypersingular integral equation of crack problems in three-dimensional elasticity along the crack boundaries. *Engineering Fracture Mechanics* 1987; **26**: 783–788

[30] Kachanov M. Elastic solids with many cracks and related problems. *Advances in Applied Mechanics* 1994; **30**: 259–445

[31] Kupradze V.D. *Potential Methods in the Theory of Elasticity.* Jerusalem: Israel Program for Scientific Translations; 1965. (Translation of Russian edition. 1963. Gos. Izdat. Fiz-Mat. Lit., Moscow)

[32] Kuriyama K., Mizuta Y. Three-dimensional elastic analysis by the Displacement Discontinuity Method with boundary division into triangular leaf elements. *International Journal of Rock Mechanics, Mining Science & Geomechanics Abstracts* 1993; **30** (2): 111–123

[33] Kuriyama K., Mizuta Y., Mozumi H., Watanabe T. Three-dimensional Elastic Analysis by the Boundary Element Method with Analytical Integrations over Triangular Leaf Elements. *International Journal of Rock Mechanics, Mining Science & Geomechanics Abstracts* 1995; **32**(1): 77–83

[34] Kushch V. Interacting cracks and inclusions in a solid by multipole expansion method. *International Journal of Solids & Structures* 1998; **35** (15): 1751–1762

[35] Kushch V, Sangani AS. Stress intensity factor and effective stiffness of a solid containing aligned penny-shaped cracks. *International Journal of Solids & Structures* 1999; **37**: 6555–6570

[36] Lachat J.C., Watson J.O. Effective numerical treatment of boundary integral equations: a formulation for three-dimensional elastostatics. *International Journal for Numerical Methods in Engineering* 1976; **10**: 991-1005

[37] Lazarus V. Perturbation approaches of a planar crack in linear elastic fracture mechanics: A review. *Journal of the Mechanics and Physics of Solids* 2011; **59**: 121–144

[38] Lazarus V., Leblond J.B., Mouchrif S-E. Crack front rotation and segmentation in mixed mode I+III or I+II+III. *Journal of the Mechanics and Physics of Solids* 2001; **49**: 1399–1443

[39] Lecampion B. An extended finite element method for hydraulic fracture problems. *Communications in Numerical Methods in Engineering* 2009; **25**(2): 121–133. DOI: 10.1002/cnm.1111

[40] Lecampion B., Desroches J. Simultaneous initiation and growth of multiple radial hydraulic fractures from a horizontal wellbore. *Journal of Mechanics and Physics of Solids* 2015; **82**: 235–258

[41] Li H., Liu C.L., Mizuta Y., Kayupov M.A. Crack edge element of three-dimensional displacement discontinuity method with boundary division into triangular leaf elements. *Communications in Numerical Methods in Engineering* 2001; **17**: 365–378

[42] Linkov A.M. Real and complex hypersingular integrals and integral equations in computational mechanics. *Demonstratio Mathematica* 1995; **28** (4): 759–769

[43] Linkov A.M. *Boundary Integral Equations in Elasticity Theory.* Dordrecht, Netherlands: Kluwer Academic Publishers; 2002

[44] Lin'kov A.M., Mogilevskaya S.G. Finite-part integrals in problems of three-dimensional cracks. *Journal of Applied Mathematics & Mechanics* 1986; **50** (5): 652–658

[45] Linkov A.M., Mogilevskaya S.G. Complex hypersingular BEM in plane elasticity problems. In: Sladek V., Sladek J. (eds) *Singular integrals in boundary element method*, Chapter 9. Southampton: Computational Mechanics Publication; 1998: 299–364

[46] Lin'kov A.M., Zubkov V.V., Heib M.A. A method for solving three-dimensional problems of seam workings and geological faults. *Journal of Mining Science* 1997; **33** (4): 295–315

[47] Y. Liu, *Fast Multipole Boundary Element Method: Theory and Applications in Engineering* Cambridge: Cambridge University Press; 2009

[48] Lo S.H., Dong C.Y., Cheung Y.K. Integral equation approach for 3D multiple-crack problems. *Engineering Fracture Mechanics* 2005; **72** (12): 1830–1840

[49] Meng C., Maerten F., Pollard D.D. Modeling mixed-mode fracture propagation in isotropic elastic three dimensional solid. *International Journal of Fracture* 2013; **179**: 45–57

[50] Mi Y., Aliabadi M.H. Dual boundary element method for three-dimensional fracture mechanics analysis. *Engineering Analysis with Boundary Elements* 1992; **10** (2): 161–171

[51] Mogilevskaya S.G. The universal algorithm based on complex hypersingular integral equation to solve plane elasticity problems. *Computational Mechanics* 1996; **18**: 127–138

[52] Mogilevskaya S.G., Rothenburg L., Dusseault M.B. Growth of pressure-induced fractures in the vicinity of a wellbore. *International Journal of Fracture* 2000; **104**: L25–L30

[53] Mogilevskaya S.G. Lost in translation: Crack problems in different languages. *International Journal of Solids and Structures* 2014; **51**: 4492–4503. DOI: 10.1016/j.ijsolstr.2014.08.025

[54] Mogilevskaya S.G., Nikolskiy D.V. The use of complex integral representations for analytical evaluation of three-dimensional BEM integrals. Potential and Elasticity problems. *The Quarterly Journal of Mechanics and Applied Mathematics* 2014; **67**: 505–523

[55] Muskhelishvili N.I. *Singular integral equations.* Groningen: P.Noordhoff; 1953; New York: Dover Publications; 1992

[56] Muskhelishvili N.I. *Some Basic Problems of the Mathematical Theory of Elasticity - fundamental equations, plane theory of elasticity, torsion, and bending.* Groningen: P.Noordhoff; 1963

[57] Newman J.N. Distributions of sources and normal dipoles over a quadrilateral panel, *Journal of Engineering Mathematics* 1986; **20**: 113–126

[58] Nikolskiy D.V., Mogilevskaya S.G., Labuz J.F. Complex variables boundary element analysis of three-dimensional crack problems. *Engineering Analysis with Boundary Elements* 2013; **37**: 1532–1544

[59] Nikolskiy D.V., Mogilevskaya S.G., Labuz J.F. Boundary element analysis of non-planar three-dimensional cracks using complex variables. *International Journal of Rock Mechanics and Mining Sciences* 2015; **76**: 44–54

[60] Nintcheu Fata. S. Explicit expressions for 3D boundary integrals in potential theory, *International Journal for Numerical Methods in Engineering* 2009; **78**: 32–47

[61] Nintcheu Fata S. Explicit expressions for three-dimensional boundary integrals in linear elasticity. *Journal of Computational and Applied Mathematics* 2011; **235**: 4480–4495

[62] Okon E.E., Harrington R.F. The potential due to a uniform source distribution over a triangular domain, *International Journals for Numerical Methods in Engineering* 1982; **18**: 1401–1419

[63] Okon E.E., Harrington R.F. The potential integral for a linear distribution over a triangular domain, *International Journals for Numerical Methods in Engineering* 1982; **18**: 1821–1828

[64] Okon E.E. Potential integrals associated with quadratic distributions in a triangular domain, *International Journals for Numerical Methods in Engineering* 1985; **21**: 197–209

[65] Parton V.Z., Perlin P.I. *Integral Equations in Elasticity.* Moscow: Mir Publishers; 1982

[66] Perlin P.I., Samarov V.N. Application of the theory of generalized potential to the solution of three-dimensional problems of elasticity for bodies with cuts and the estimation of brittle fracture of complex-shaped structures. *Izvestiya Akademii Nauk Kazakhskoi SSR. Ser. Fiz.-Matem.* 1974; **5**: 72–73 (in Russian)

[67] Perlin P.I., Samarov V.N. Application of potential theory to the solution of three-dimensional problems of elasticity for bodies with cuts. *Prikladnye Problemy Prochnosti i Plastichnosti* 1977; **6**: 42–46 (in Russian)

[68] Piltner R.The use of complex valued functions for the solution of three-dimensional elasticity problems. *Journal of Elasticity* 1987; **18**: 191–225

[69] Piltner R. On the representation of three-dimensional elasticity solutions with the aid of complex valued functions. *Journal of Elasticity* 1989; **22**: 45–55

[70] Pompeiu D. Sur une classe de functions d'une variable complexe et sur certaine equations integrales, *Rendiconti del Circolo Matematico di Palermo* 1913; **35**: 277–281

[71] Qin T.Y., Tang R.J. Finite-part integral and boundary element method to solve embedded planar crack problems. *International Journal of Fracture* 1993; **60**: 373–381

[72] Qin T.Y., Chen W.J., Tang R.J. Three-dimensional crack problem analysis using boundary element method with finite-part integrals. *International Journal of Fracture* 1997; **84**: 191–202

[73] Rjasanow S., Steinbach O. *The Fast Solution of Boundary Integral Equations* Berlin: Springer; 2007

[74] Sack R.A. Extension of Griffith's theory of rupture to three dimensions. *Proceedings of the Physical Society, London* 1946; **58**: 729

[75] Salvadori A. Analytical integrations of hypersingular kernel in 3D BEM problems. *Computer Methods in Applied Mechanics and Engineering* 2001; **190**: 3957–3975

[76] Salvadori A. Analytical integrations in 2D BEM elasticity, *International Journals for Numerical Methods in Engineering* 2002; **53**: 1695–1719

[77] Salvadori A. Analytical integrations in 3D BEM for elliptic problems: Evaluation and implementation, *International Journals for Numerical Methods in Engineering* 2010; **84**: 505–542

[78] Salvadori A., Temponi A. Analytical integrations for the approximation of 3D hyperbolic scalar boundary integral equations, *Engineering Analysis with Boundary Elements* 2010; **34**: 977–994

[79] Segedin C.M. Note on a penny-shaped crack under shear. Mathematical Proceedings of the Cambridge Philosophical Society 1951; 47 (2): 396-400

[80] Shabat B.V. *Introduction to Complex Analysis.* Translations of Mathematical Monographs, vol. **110** Providence: American Mathematical Society; 1992

[81] Sladek V., Sladek J. 1983. Three-dimensional curved crack in an elastic body. *International Journal of Solids and Structures.* **19**: 425–436

[82] Sneddon I.N. The distribution of stress in the neighbourhood of a crack in an elastic solid. *Proceedings of the Royal Society A* 1946: 187–229

[83] Stephan E.P. A boundary integral equation method for three-dimensional crack problems in elasticity. *Mathematical Methods in the Applied Sciences* 1986; **8**: 609–623

[84] Tanaka M., Sladek V., Sladek J. Regularization techniques applied to boundary element methods. *Applied Mechanics Reviews* 1994; **47** (10): 457–499

[85] I. N. Vekua, *Generalized Analytic Functions.* Oxford: Pergamon Press; 1962

[86] C.-Y. Wang and M. Denda, 3D BEM for general anisotropic elasticity, *International Journal of Solids and Structures* 2007; **44**: 7073–7091

[87] Weng X. Fracture Initiation from Deviated Wellbores. SPE 25967, presented at the 68th Annual Technical Conference and Exhibit held in Houston, TX, Oct 3–6, 1993

[88] L. C. Wrobel, *The Boundary Element Method: Applications in Thermo-Fluids and Acoustics*, vol. **1** Chichester: John Wiley & Sons, Ltd.; 2002

Appendix A

Treatment of Body Integrals

The volume integrals representing the constant body force **b** are treated by the standard technique based on the following Galerkin vector representation (see [2]):

$$U_{ik} = G_{ik,ll} - \frac{1}{2(1-\nu)} G_{il,lk} \tag{A.1}$$

Using the divergence theorem the volume integrals in Eqs.(2.37) and (2.38) are transformed to the following surface integrals:

$$\int_{\Omega} U_{ij}(x,\xi)\, b_j dV_\xi = \int_{\partial\Omega} P_i(\xi)\, dS_\xi \tag{A.2}$$

$$\int_{\Omega} T_{ij}(x,\xi)\, b_j dV_\xi = \int_{\partial\Omega} B_{ij}(\xi)\, n_j(x)\, dS_\xi \tag{A.3}$$

where

$$P_i(\xi) = \frac{1}{8\pi\mu}\left[b_i n_k(\xi)\, r_{,k} - \frac{1}{2(1-\nu)} b_k n_i(\xi)\, r_{,k} \right] \tag{A.4}$$

and

$$
\begin{aligned}
B_{ij}(\xi) = & \frac{1}{8\pi(1-\nu)r}\delta_{ij}\left[\left(b_k n_k(\xi) - b_k r_{,k} n_l(\xi) r_{,l}\right)\right] \\
& + \frac{1-2\nu}{16\pi(1-\nu)r}\left[\left(b_i n_j(\xi) + b_j n_i(\xi)\right)\right] \\
& - \frac{1}{8\pi r} n_k(\xi) r_{,k}\left[b_i r_{,j} + b_j r_{,i}\right] \\
& + \frac{1}{16\pi(1-\nu)r} b_k r_{,k}\left[n_i(\xi) r_{,j} + n_j(\xi) r_{,i}\right]
\end{aligned} \tag{A.5}
$$

Appendix B

Calculation of the Coefficients of Shape Functions

In Chapter 4 (see Subection 4.3.1), the shape function associated with the M-th node of the element of interest E_s (referred as $N^{(M)}$ in the "global" listing of the nodes) was expressed in terms of the used complex notations as follows:

$$L^{(M)}(\tau,\overline{\tau}) = \sum_{\substack{m,n=0 \\ m+n\leq 2}}^{2} \kappa_{mn}^{(M)} (\tau - z)^m (\overline{\tau} - \overline{z})^n \tag{B.1}$$

where τ, $\overline{\tau}$ (understood as independent variables) define the position of the point on the element and z corresponds to the projection of the point $\mathbf{x}$ to the plane of the element. The coefficients $\kappa_{mn}^{(M)} = \overline{\kappa_{nm}^{(M)}}$ are defined by the geometry of the element E_s and the arrangement of the nodes on it.

The matrix $\left[\widetilde{\mathbf{F}}^{(s)}\right]$ that contains coefficients $\kappa_{mn}^{(N)}$ of the shape functions (see Subsection 4.3.1) can be assembled as a product of three matrices: $\left[\widetilde{\mathbf{M}}\right]$ defined by the relative positions of the edge nodes , $\left[\widetilde{\mathbf{S}}\right]$ related to the geometry of the element in terms of the used complex notations, and $\left[\widetilde{\mathbf{Z}}\right]$ defined by the position of the point $\mathbf{x}$ with respect to

the element. Thus,

$$\left[\widetilde{\mathbf{F}}^{(s)}\right] = \begin{bmatrix} \kappa_{00}^{(1)} & \kappa_{00}^{(2)} & \dots & \kappa_{00}^{(6)} \\ \kappa_{10}^{(1)} & \kappa_{10}^{(2)} & \dots & \kappa_{10}^{(6)} \\ & \dots & & \\ \kappa_{02}^{(1)} & \kappa_{02}^{(2)} & \dots & \kappa_{02}^{(6)} \\ \kappa_{11}^{(1)} & \kappa_{11}^{(2)} & \dots & \kappa_{11}^{(6)} \end{bmatrix} = \left[\widetilde{\mathbf{Z}}\right]^T \cdot \left[\widetilde{\mathbf{S}}\right]^T \cdot \left[\widetilde{\mathbf{M}}\right]^T \tag{B.2}$$

where the superscript T denotes transposition.

In the algorithm, the relative positions of the edge nodes are defined via assigning "weights" to the vertices. The "weights" of the crack tip nodes may be chosen as either 1 or 3 (see Subsection 4.2.2 for the rationale of that choice); the "weights" of the other nodes are equal to 1. Let W_1, W_2, W_3 denote the "weights" of the vertices N_1, N_2, N_3, correspondingly; N_4, N_5, N_6 will denote the edge nodes each placed at the "center of gravity" of the corresponding edge.

As in Subsection 4.3.3, let $a_1 = \xi_1^{(1)} + i\xi_2^{(1)}$, $a_2 = \xi_1^{(2)} + i\xi_2^{(2)}$, and $a_3 = \xi_1^{(3)} + i\xi_2^{(3)}$ be the complex coordinates of the vertices of the element E_s in terms of the local coordinate system. Thus, the positions of the edge nodes are defined by $a_4 = (a_2W_2 + a_3W_3)/(W_2 + W_3)$, $a_5 = (a_1W_1 + a_3W_3)/(W_1 + W_3)$, and $a_6 = (a_1W_1 + a_2W_2)/(W_1 + W_2)$.

The matrix $\left[\widetilde{\mathbf{M}}^{(s)}\right]$ is defined as follows:

$$\left[\widetilde{\mathbf{M}}^{(s)}\right] = \begin{bmatrix} 1 & -\frac{W_1}{W_2} - 2 & -\frac{W_1}{W_3} - 2 & \frac{W_1+W_2}{W_2} & \frac{W_1+W_3}{W_3} & W_1(\frac{1}{W_3} + \frac{1}{W_2}) + 2 \\ 0 & -\frac{W_2}{W_1} & 0 & \frac{W_1+W_2}{W_1} & 0 & W_2(\frac{1}{W_1} - \frac{1}{W_3}) \\ 0 & 0 & -\frac{W_3}{W_1} & 0 & \frac{W_1+W_3}{W_1} & W_3(\frac{1}{W_1} - \frac{1}{W_2}) \\ 0 & 0 & 0 & 0 & 0 & \frac{(W_2+W_3)^2}{W_2*W_3} \\ 0 & 0 & \frac{(W_1+W_3)^2}{W_1*W_3} & 0 & -\frac{(W_1+W_3)^2}{W_1*W_3} & -\frac{(W_1+W_3)^2}{W_1*W_3} \\ 0 & \frac{(W_1+W_2)^2}{W_1*W_2} & 0 & -\frac{(W_1+W_2)^2}{W_1*W_2} & 0 & -\frac{(W_1+W_2)^2}{W_1*W_2} \end{bmatrix} \tag{B.3}$$

where each row represents the coefficients of the shape function related to the corresponding node expressed in terms of the following monomials:

$$1,\ \eta_1,\ \eta_2,\ \eta_1^2,\ \eta_2^2,\ \eta_1\eta_2 \tag{B.4}$$

where η_1 and η_2 are the so-called "master element" coordinates of the point $\boldsymbol{\xi} \in E_s$ (see Fig. B.1).

The matrix $\left[\widetilde{\mathbf{S}}^{(s)}\right]$ represents the coordinate transformation from η_1 and η_2 in terms of monomials defined by Eq.(B.4) to τ and $\overline{\tau}$ in terms of the following monomials:

$$1,\ \tau,\ \overline{\tau},\ \tau^2,\ \overline{\tau}^2,\ \tau\overline{\tau} \tag{B.5}$$

This matrix is expressed as follows:

$$\left[\widetilde{\mathbf{S}}^{(s)}\right] = \begin{bmatrix} 1 & 0 & 0 & 0 & 0 & 0 \\ 0 & P_{11} & P_{12} & 0 & 0 & 0 \\ 0 & P_{21} & P_{22} & 0 & 0 & 0 \\ 0 & 0 & 0 & P_{11}^2 & P_{12}^2 & 2P_{11}P_{12} \\ 0 & 0 & 0 & P_{21}^2 & P_{22}^2 & 2P_{21}P_{22} \\ 0 & 0 & 0 & P_{11}P_{21} & P_{12}P_{22} & P_{11}P_{22} + P_{21}P_{12} \end{bmatrix} \tag{B.6}$$

where P_{jk} are the coefficients of the following matrix:

$$\left[\widetilde{\mathbf{P}}^{(s)}\right] = \begin{bmatrix} \frac{\overline{b}_3 - \overline{b}_1}{D} & \frac{b_1 - b_3}{D} \\ \frac{\overline{b}_1 - \overline{b}_2}{D} & \frac{b_2 - b_1}{D} \end{bmatrix} \tag{B.7}$$

and

$$D = (b_3 - b_2)\overline{b}_1 + (b_1 - b_3)\overline{b}_2 + (b_2 - b_1)\overline{b}_3 \tag{B.8}$$

For the continuous approximation scheme (**a**), see Subsection 4.2.2, $b_k = a_k$, $k = 1 \ldots 3$. For the discontinuous approximation scheme (**b**), $b_k = (1 - \beta)a_k + \beta z_c$, where $z_c = (a_1 + a_2 + a_3)/3$ corresponds to the centroid of the element and the parameter β defines

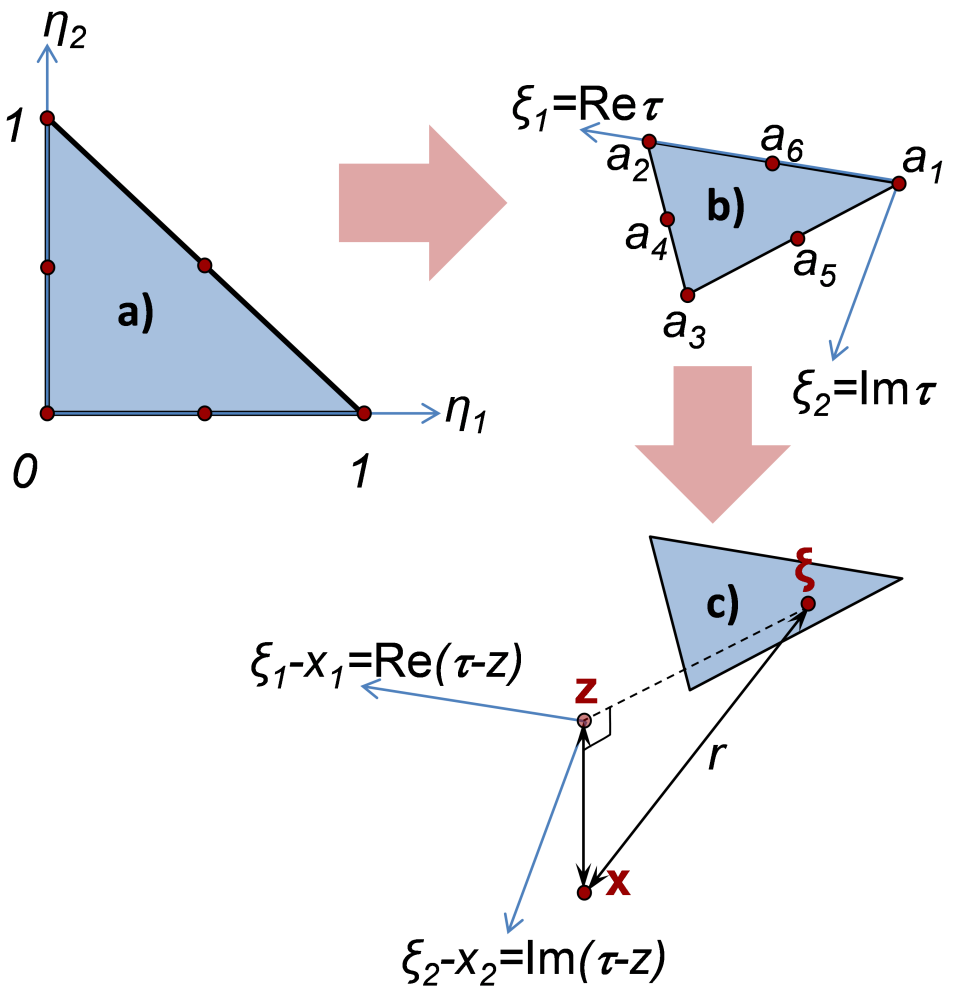

Figure B.1: An illustration to the used coordinate transformations. a) the master element; b) the element in the local Cartesian coordinate system; c) the coordinate system shifted to z.

the relative distance between the element contour and its centroid where the nodes are located.

The above matrices are defined only by the geometry of the element, therefore they (and their product) need to be calculated once for each element, while only the matrix $\left[\widetilde{\mathbf{Z}}^{(s)}\right]$ has to be recalculated for each collocation point. The matrix is defined as follows:

$$\left[\widetilde{\mathbf{Z}}^{(s)}\right] = \begin{bmatrix} 1 & 0 & 0 & 0 & 0 & 0 \\ b_1 - z & 1 & 0 & 0 & 0 & 0 \\ \overline{b}_1 - \overline{z} & 0 & 1 & 0 & 0 & 0 \\ (z - b_1)^2 & 2(b_1 - z) & 0 & 1 & 0 & 0 \\ (\overline{z} - \overline{b}_1)^2 & 0 & 2(\overline{b}_1 - \overline{z}) & 0 & 1 & 0 \\ (z - b_1)(\overline{z} - \overline{b}_1) & \overline{b}_1 - \overline{z} & b_1 - z & 0 & 0 & 1 \end{bmatrix} \tag{B.9}$$

Appendix C

Integration over a Boundary Element with Contour Containing Circular Arcs

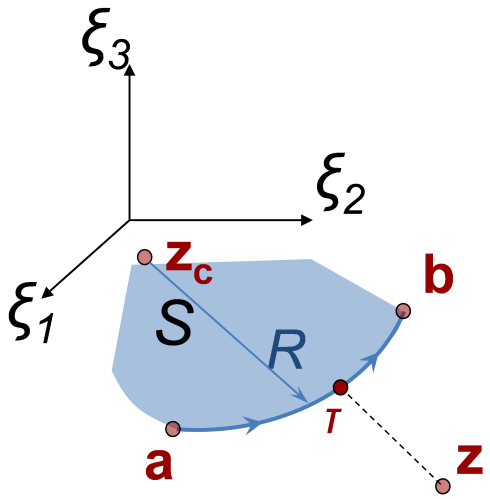

Figure C.1: Circular arc segment of a boundary element contour.

The complex equation for the circular arc $\widehat{\mathbf{a},\mathbf{b}}$ with its centre at the point $\mathbf{z}_c$ associated with the complex combination $z_c = z_{1c} + iz_{2c}$ and radius R (Fig. C.1) has the form

$$(\overline{\tau} - \overline{z}_c)(\tau - z_c) = R^2 \tag{C.1}$$

which gives $\overline{\tau} = \overline{z}_c + R^2/(\tau - z_c)$. Thus, the distance r can be expressed via the following function of τ:

$$r = \sqrt{(\tau - z)\left[\overline{z}_c - \overline{z} + \frac{R^2}{\tau - z_c}\right] + h^2} \tag{C.2}$$

- $\mathbf{z} \neq \mathbf{z}_c,\ \mathbf{z} \notin \widehat{\mathbf{a},\mathbf{b}}$

For the following considerations, it is useful to represent r as

$$r = |Z|\sqrt{\frac{g(\vartheta)}{\vartheta}} \quad \text{with} \quad \vartheta = \frac{\tau - z_c}{Z}, \quad Z = z_c - z, \tag{C.3}$$

and the function $g(\vartheta)$ given by

$$g(\vartheta) = \vartheta^2 + A\vartheta + B = (\vartheta + \chi_1)(\vartheta + \chi_2), \tag{C.4}$$

where

$$\chi_{1,2} = \frac{1}{2}\left(A \mp \sqrt{A^2 - 4B}\right), \quad A = \frac{h^2 + R^2 + |Z|^2}{|Z|^2}, \quad B = \frac{R^2}{|Z|^2}.$$

Substituting (C.2) into (4.34) and expressing $(\tau - z)^m$ through $\tau - z_c$ one can represent

the integrals in (4.32) via the following ones:

$$
n=0\text{: }\int_a^b \frac{f(\tau)d\tau}{\tau-z}=\begin{cases} 2I_{-1}(a,b) & m=-1 \\ 2\sum\limits_{k=0}^{m}\binom{m}{k}Z^{m-k}J_k(a,b) & m\geq 0 \end{cases}
$$

$$
n=1\text{: }\int_a^b \frac{f(\tau)d\tau}{\tau-z}=\begin{cases} \frac{2}{3}\Big[\,\overline{Z}J_0(a,b)-2h^2I_{-1}(a,b) \\ \quad -(R^2/Z)\left(I_{-1}(a,b)-J_{-1}(a,b)\right)\Big] & m=0 \\ \frac{2}{3}\Big[\sum\limits_{k=0}^{m}\binom{m}{k}Z^k\overline{Z}J_{m-k}(a,b) \\ \quad -\sum\limits_{k=0}^{m-1}\binom{m}{k}Z^k\left(2h^2J_{m-k-1}(a,b)\right. \\ \quad \left.-R^2J_{m-k-2}(a,b)\right)\Big] & m\geq 1 \end{cases} \tag{C.5}
$$

$$
n=2\text{: }\int_a^b \frac{f(\tau)d\tau}{\tau-z}=\begin{cases} \frac{16}{15}h^4I_{-1}(a,b)+\frac{6}{15}\sum\limits_{k=0}^{1}Z^k\Big[3\overline{Z}^2J_{2-k}(a,b) \\ \quad +2R^2\overline{Z}J_{1-k}(a,b)+R^4J_{-k}(a,b)\Big] \\ -\frac{8}{15}h^2\Big[\,\overline{Z}J_0(a,b)+R^2J_{-1}(a,b)\Big] & m=1 \\ \frac{16}{15}h^4J_0(a,b)+\frac{6}{15}\sum\limits_{k=0}^{2}\binom{2}{k}Z^k\Big[3\overline{Z}^2J_{3-k}(a,b) \\ \quad +2R^2\overline{Z}J_{2-k}(a,b)+R^4J_{1-k}(a,b)\Big] \\ -\frac{8}{15}h^2\sum\limits_{k=0}^{1}Z^k\Big[\,\overline{Z}J_{1-k}(a,b)+R^2J_{-k}(a,b)\Big] & m=2 \end{cases}
$$

where

$$
J_k(a,b)=\int_a^b r(\tau)\left(\tau-z_c\right)^k d\tau=Z^{k+1}|Z|\int_{\vartheta_a}^{\vartheta_b}\sqrt{g(\vartheta)}\,\vartheta^{k-\frac{1}{2}}\,d\vartheta, \tag{C.6}
$$

$\vartheta_a=(a-z_c)/Z$, $\vartheta_b=(b-z_c)/Z$, and $a=a_1+ia_2$ and $b=b_1+ib_2$ represent the beginning point **a** and the end point **b** of the arc. Using (C.3) and (C.4), one obtains

the following analytical expressions for the integrals involved in (C.5):

$$I_{-1}(a,b) = \int_a^b \frac{r(\tau)}{\tau - z} d\tau$$
$$= 2\left\{ r + \frac{i\,|Z|}{\sqrt{\chi_1}} \left[\frac{h^2}{|Z|^2} P(\vartheta) + \chi_1 (E(\vartheta) + (\chi_2 - 1) F(\vartheta)) \right] \right\} \Bigg|_{\vartheta_a}^{\vartheta_b}, \qquad \text{(C.7)}$$

$$J_k(a,b) = \begin{cases} 2\left\{ r + i(|Z|/\sqrt{\chi_1}) \left[2\chi_1 E(\vartheta) + (\chi_2 - \chi_1) F(\vartheta) \right] \right\} \Big|_{\vartheta_a}^{\vartheta_b} & k = -1 \\ \\ \frac{2}{3} Z \Big\{ r(\chi_2 + \chi_1 + \vartheta) \\ \quad + i|Z| \sqrt{\chi_1} \left[(\chi_2 + \chi_1) E(\vartheta) + (\chi_2 - \chi_1) F(\vartheta) \right] \Big\} \Big|_{\vartheta_a}^{\vartheta_b} & k = 0 \\ \\ \Big\{ \; 2r^3 (\tau - z_c)^k / \, \overline{Z} \Big|_{\tau=a}^{\tau=b} - 2kAZ J_{k-1}(a,b) \\ \quad - (2k-3) B Z^2 J_{k-2}(a,b) \Big\} / (2k+3) & k \geq 1 \end{cases} \qquad \text{(C.8)}$$

where

$$E(\vartheta) = \mathrm{E}\left(\sin^{-1}\left(i \sqrt{\frac{\chi_1}{\vartheta}} \right) \middle| \, \frac{\chi_2}{\chi_1} \right), \quad F(\vartheta) = \mathrm{F}\left(\sin^{-1}\left(i \sqrt{\frac{\chi_1}{\vartheta}} \right) \middle| \, \frac{\chi_2}{\chi_1} \right),$$
$$P(\vartheta) = \Pi\left(\frac{1}{\chi_1}; \sin^{-1}\left(i \sqrt{\frac{\chi_1}{\vartheta}} \right) \middle| \, \frac{\chi_2}{\chi_1} \right)$$

and $\mathrm{F}(\phi|k)$, $\mathrm{E}(\phi|k)$ and $\Pi(l;\phi|k)$ are elliptic integrals of the first, second and third kind, respectively, defined as follows:

$$\mathrm{F}(\phi|k) = \int_0^\phi \left(1 - k \sin^2\theta\right)^{-\frac{1}{2}} d\theta, \quad \mathrm{E}(\phi|k) = \int_0^\phi \left(1 - k \sin^2\theta\right)^{\frac{1}{2}} d\theta,$$
$$\Pi(l;\phi|k) = \int_0^\phi \left(1 - l \sin^2\theta\right) \left(1 - k \sin^2\theta\right)^{-\frac{1}{2}} d\theta.$$

We should emphasize that in case when $\arg a < \arg(z - z_c) < \arg b$, the argument of the elliptic functions may undergo a jump; the simplest remedy is to treat $J_k(a,b)$ as

$$J_k(a,b) = \int_a^{\tau_z} r(\tau) \, (\tau - z_c)^k d\tau + \int_{\tau_z}^b r(\tau) \, (\tau - z_c)^k d\tau,$$

where $\tau_z = z_c + R \arg(z - z_c)$.

- $\mathbf{z} \in \widehat{\mathbf{a}, \mathbf{b}}$

In this case, $(\overline{z}_c - \overline{z})(z_c - z) = R^2$, the integral (C.7) is understood as Cauchy principal value integral, and (C.5)–(C.8) remain the same with

$$A = \frac{h^2 + 2R^2}{R^2}, \quad B = 1, \quad \chi_{1,2} = \frac{1}{2R^2}\left[h^2 + 2R^2 \mp |h|\sqrt{h^2 + 4R^2}\right].$$

- $\mathbf{z} = \mathbf{z}_c$

In this case, $r = \sqrt{R^2 + h^2}$ and

$$\int_a^b r(\tau - z_c)^k d\tau = \frac{\sqrt{R^2 + h^2}}{k+1}(\tau - z_c)^{k+1}\Big|_{\tau=a}^{\tau=b}.$$

Thus, the expressions for the parts of the integrals in (4.32) corresponding to $\widehat{\mathbf{a}, \mathbf{b}}$ become

$$\int_a^b \frac{f(\tau)\, d\tau}{\tau - z} = \begin{cases} \frac{2}{m}\sqrt{R^2 + h^2}\,(\tau - z_c)^m|_{\tau=a}^{\tau=b} & n = 0 \\ \frac{2}{3(m-1)}\sqrt{R^2 + h^2}\,(R^2 - 2h^2)\,(\tau - z_c)^{m-1}\Big|_{\tau=a}^{\tau=b} & n = 1 \\ \frac{2}{15(m-2)}\sqrt{R^2 + h^2}\,(3R^4 - 4h^2R^2 + 8h^4)\,(\tau - z_c)^{m-2}\Big|_{\tau=a}^{\tau=b} & n = 2 \end{cases} \tag{C.9}$$

Appendix D

Stresses around a Penny-Shaped Crack

The problem of a penny-shaped crack under specified load at infinity can be solved by using superposition of two solutions: one for an infinite domain without a crack under the prescribed load at infinity, and a complementary one for the same domain with a crack loaded by the tractions on its surface (opposite to those induced by the stress field from the first problem) and vanishing stresses at infinity.

The complementary problem for a penny-shaped crack located in the plane $z = 0$ under $\sigma_{zz}^{\infty} = S$ is characterized by the following boundary conditions for the stress equilibrium equation (2.26):

$$\sigma_{zz} = -S;\ \sigma_{xz} = \sigma_{yz} = 0 \ \text{ for } z = 0; r < a \tag{D.1}$$

$$u_x, u_y, u_z \text{ are continuous for } z = 0; r > a$$

For the shear loading case ($\sigma_{xz}^{\infty} = S$), the boundary conditions are

$$\begin{aligned} &\sigma_{xz} = -S;\ \sigma_{yz} = \sigma_{zz} = 0 \ \text{ for } z = 0; r < a \\ &u_x, u_y, u_z \text{ are continuous for } z = 0; r > a \end{aligned} \tag{D.2}$$

One possible way of solving those problems is to reduce them to equivalent ones for axisymmetric harmonic potential ψ with certain boundary conditions for it. In fact, as shown by Segedin [79], both problems can be reduced to the same boundary conditions for ψ:

$$\begin{aligned} \frac{\partial^2 \psi}{\partial z^2} &= -K \ \text{ for } z = 0; r < a \\ \frac{\partial \psi}{\partial z} &= 0 \ \text{ for } z = 0; r > a \end{aligned} \tag{D.3}$$

but with different scaling coefficients for K: $K = \frac{S}{2\mu}$ for tension and $K = \frac{S}{\mu(2-\nu)}$ for shear.load. The convenient representation of the solution of this problem was given by Fabrikant [15]:

$$\begin{aligned} \psi(r,z) &= \frac{K}{2\pi}\left[\left(r^2 - 2z^2 - 2a^2\right)\arcsin\frac{L_1}{r} + \frac{2a^2 - 3L_1^2}{a}\left(L_2^2 - a^2\right)^{1/2}\right], \\ L_{1,2} &= \frac{1}{2}\left[\left((a+r)^2 + z^2\right)^{1/2} \mp \left((a-r)^2 + z^2\right)^{1/2}\right] \end{aligned} \tag{D.4}$$

Note that the above expressions are given for $z \geq 0$; the potential ψ is supposed to be even with respect to z. In case of tensile loading, the expressions for the stress

components are (see [22] and Chapter 21 in [4])

$$\begin{aligned}
\frac{\sigma_{xx}}{2\mu} &= \frac{\partial^2\psi}{\partial x^2} + 2\nu\frac{\partial^2\psi}{\partial y^2} + z\frac{\partial^3\psi}{\partial x^2\partial z} \\
\frac{\sigma_{yy}}{2\mu} &= \frac{\partial^2\psi}{\partial y^2} + 2\nu\frac{\partial^2\psi}{\partial x^2} + z\frac{\partial^3\psi}{\partial y^2\partial z} \\
\frac{\sigma_{xy}}{2\mu} &= (1-2\nu)\,\frac{\partial^2\psi}{\partial x\partial y} + z\frac{\partial^3\psi}{\partial x\partial y\partial z} \\
\frac{\sigma_{xz}}{2\mu} &= z\frac{\partial^3\psi}{\partial x\partial z^2} \\
\frac{\sigma_{yz}}{2\mu} &= z\frac{\partial^3\psi}{\partial y\partial z^2} \\
\frac{\sigma_{zz}}{2\mu} &= -\frac{\partial^2\psi}{\partial z^2} + z\frac{\partial^3\psi}{\partial z^3}
\end{aligned} \tag{D.5}$$

In case of shear loading, the stresses can be easily derived from the displacements whose expressions via ψ are reported by Segedin [79]:

$$\begin{aligned}
\frac{\sigma_{xx}}{2\mu} &= 2\frac{\partial^2\psi}{\partial x\partial z} - z\frac{\partial^3\psi}{\partial x^3} \\
\frac{\sigma_{yy}}{2\mu} &= 2\nu\frac{\partial^2\psi}{\partial x\partial z} - z\frac{\partial^3\psi}{\partial x\partial y^2} \\
\frac{\sigma_{xy}}{2\mu} &= (1-\nu)\,\frac{\partial^2\psi}{\partial y\partial z} - z\frac{\partial^3\psi}{\partial x^2\partial y} \\
\frac{\sigma_{xz}}{2\mu} &= (1-\nu)\,\frac{\partial^2\psi}{\partial z^2} - \nu\frac{\partial^2\psi}{\partial x^2} - z\frac{\partial^3\psi}{\partial x^2\partial z} \\
\frac{\sigma_{yz}}{2\mu} &= -\nu\frac{\partial^2\psi}{\partial x\partial y} - z\frac{\partial^3\psi}{\partial x\partial y\partial z} \\
\frac{\sigma_{zz}}{2\mu} &= -z\frac{\partial^3\psi}{\partial x\partial z^2}
\end{aligned} \tag{D.6}$$

Finally, the far-field stress S must be added to σ_{zz} or σ_{xz}, respectively, to solve the initially stated problem.

The following expressions are sufficient to evaluate the derivatives of ψ needed to

find the stress field:

$$\begin{aligned}
\frac{\partial^2\psi}{\partial x^2} &= \frac{x^2}{r^2}\frac{\partial^2\psi}{\partial r^2} + \frac{y^2}{r^3}\frac{\partial\psi}{\partial r} \\
\frac{\partial^2\psi}{\partial y^2} &= \frac{y^2}{r^2}\frac{\partial^2\psi}{\partial r^2} + \frac{y^2}{r^3}\frac{\partial\psi}{\partial r} \\
\frac{\partial^2\psi}{\partial x\partial y} &= \frac{xy}{r^2}\frac{\partial^2\psi}{\partial r^2} - \frac{xy}{r^3}\frac{\partial\psi}{\partial r} \\
\frac{\partial^2\psi}{\partial x\partial z} &= \frac{x}{r}\frac{\partial^2\psi}{\partial r\partial z} \\
\frac{\partial^2\psi}{\partial y\partial z} &= \frac{y}{r}\frac{\partial^2\psi}{\partial r\partial z}
\end{aligned} \tag{D.7}$$

$$\begin{aligned}
\frac{\partial^3\psi}{\partial x^2\partial z} &= \frac{x^2}{r^2}\frac{\partial^3\psi}{\partial r^2\partial z} + \frac{y^2}{r^3}\frac{\partial^2\psi}{\partial r\partial z} \\
\frac{\partial^3\psi}{\partial y^2\partial z} &= \frac{y^2}{r^2}\frac{\partial^3\psi}{\partial r^2\partial z} + \frac{x^2}{r^3}\frac{\partial^2\psi}{\partial r\partial z} \\
\frac{\partial^3\psi}{\partial x\partial y\partial z} &= \frac{xy}{r^2}\frac{\partial^3\psi}{\partial r^2\partial z} - \frac{xy}{r^3}\frac{\partial^2\psi}{\partial r\partial z} \\
\frac{\partial^3\psi}{\partial x\partial z^2} &= \frac{x}{r}\frac{\partial^3\psi}{\partial r\partial z^2} \\
\frac{\partial^3\psi}{\partial y\partial z^2} &= \frac{y}{r}\frac{\partial^3\psi}{\partial r\partial z^2} \\
\frac{\partial^3\psi}{\partial x^3} &= \frac{x^3}{r^3}\frac{\partial^3\psi}{\partial r^3} + \frac{3xy^2}{r^4}\frac{\partial^2\psi}{\partial r^2} - \frac{3xy^2}{r^5}\frac{\partial\psi}{\partial r} \\
\frac{\partial^3\psi}{\partial x^2\partial y} &= \frac{x^2y}{r^3}\frac{\partial^3\psi}{\partial r^3} + \left(y^2 - 2x^2\right)\left(\frac{y}{r^4}\frac{\partial^2\psi}{\partial r^2} - \frac{y}{r^5}\frac{\partial\psi}{\partial r}\right) \\
\frac{\partial^3\psi}{\partial x\partial y^2} &= \frac{xy^2}{r^3}\frac{\partial^3\psi}{\partial r^3} + \left(x^2 - 2y^2\right)\left(\frac{x}{r^4}\frac{\partial^2\psi}{\partial r^2} - \frac{x}{r^5}\frac{\partial\psi}{\partial r}\right)
\end{aligned}$$

Omitted the common factor of $\frac{2K}{\pi}$, the cylindrical coordinate derivatives of ψ are as follows:

$$\frac{\partial\psi}{\partial r} = \frac{r}{2}\arcsin\frac{L_1}{r} - \frac{L_1}{2L_2}\left(L_2^2 - a^2\right)^{1/2}$$

$$\begin{aligned}
\frac{\partial^2\psi}{\partial r^2} &= \frac{1}{2}\arcsin\frac{L_1}{r} - \frac{a}{2}\left(1+\left(\frac{L_1}{L_2}\right)^2\right)\frac{\left(L_2^2-a^2\right)^{1/2}}{\left(L_2^2-L_1^2\right)} \\
\frac{\partial^2\psi}{\partial r\partial z} &= -a\frac{L_1}{L_2}\frac{\left(a^2-L_1^2\right)^{1/2}}{\left(L_2^2-L_1^2\right)} \\
\frac{\partial^2\psi}{\partial z^2} &= -\arcsin\frac{L_1}{r} + a\frac{\left(L_2^2-a^2\right)^{1/2}}{\left(L_2^2-L_1^2\right)}
\end{aligned} \tag{D.8}$$

$$\begin{aligned}
\frac{\partial^3\psi}{\partial r^2\partial z} &= \frac{a^2 z}{L_2^2\left(L_2^2-a^2\right)^{1/2}}\left(4r^2\frac{L_2^2-a^2}{\left(L_2^2-L_1^2\right)^3} - \frac{a^2-z^2}{\left(L_2^2-L_1^2\right)^2}\right) \\
\frac{\partial^3\psi}{\partial r\partial z^2} &= \frac{a}{L_2}\frac{\left(r^2-L_1^2\right)^{1/2}}{\left(L_2^2-L_1^2\right)^3}\left(a^2\left(4L_2^2-5r^2\right)+L_1^4\right) \\
\frac{\partial^3\psi}{\partial z^3} &= \frac{\left(a^2-L_1^2\right)^{1/2}}{\left(L_2^2-L_1^2\right)^3}\left(L_1^4+a^2\left(2a^2+2z^2-3r^2\right)\right) \\
\frac{\partial^3\psi}{\partial r^3} &= -\frac{1}{2}\frac{\left(L_2^2-a^2\right)^{1/2}}{\left(L_2^2-L_1^2\right)}\left\{\frac{L_1}{L_2}+2\frac{a^2L_1}{L_2^3}\frac{\left(z^2-r^2+a^2\right)}{L_2^2-L_1^2}\right. \\
&\quad \left.+\frac{ar}{L_2^2-L_1^2}\left(1+\frac{L_1^2}{L_2^2}\right)\left(1-2\frac{\left(z^2+r^2-a^2\right)}{L_2^2-L_1^2}\right)\right\}
\end{aligned}$$

Using (D.5) for tensile loading and (D.6) for shear loading, one can evaluate all stress components at any point in the domain.